ROMA
TRE
UNIVERSITÀ DEGLI STUDI

Ph.D. IN CIVIL ENGINEERING

XXX CYCLE

Internal solitary waves interacting with the bottom

Ph.D. Student:
Ing. Giovanni la Forgia

Tutor:
Prof. Claudia Adduce
Claudia Adduce

Co-Tutor:
Dr. Federico Falcini

Coordinator Ph.D. Course:
Prof. Gianmarco De Felice

Collana delle tesi di Dottorato di Ricerca
In Scienze dell'Ingegneria Civile
Università degli Studi Roma Tre
Tesi n° 69

Ai miei genitori

Abstract

Nonlinear internal waves are observed in many parts of the world ocean. They are mostly generated by the interaction between tidal flow and the bottom topography. Internal waves are important physical phenomena on the continental shelf/slope. They are often very energetic, and their breaking provides an important dissipation and mixing mechanism, with implications for biological productivity and sediment transport. Breaking mechanisms associated with internal solitary waves include bottom boundary layer instabilities, shear instabilities in the interior of the water column, and wave overturning as they shoal.

In the present work, internal solitary waves (ISWs) propagating in a two layer stratified fluid system are primarily studied by laboratory experiments. The generation, propagation, and breaking phases of large amplitude internal solitary waves of depression, propagating horizontally in a wave tank, are investigated. ISWs main features result to be dependent on the geometrical parameters that define the initial experimental setting: empirical relations between ISWs geometric and kinematic features and the initial setting parameters are obtained. The approach of the ISWs towards a uniform sloping boundary is investigated. Depending on both waves properties and slopes values, different physical processes characterize the shoaling phase, causing the development of different breaker types. Following a qualitatively analysis of the different breaking mechanisms, collapsing-plunging breakers show the larger contribution in terms of mixing.

Internal wave packets propagating towards the North of the Messina Strait (Mediterranean Sea) are investigated. In this region, the analysis of both the observed internal waves, and the bathymetry suggests that plunging breakers are expected to occur. Additional laboratory experiments are carried out in order to investigate how the pycnocline thickness is affected by the breaking of plunging ISWs. The increase of the pycnocline thickness results to be non-linearly related with the Iribarren number.

High-resolution 3-D large Eddy Simulations (LES) are also used to investigate the effects of internal solitary waves breaking over a sloping boundary. Here again, the lock release method is applied in a two-layer stratified fluid system to generate the three main breaking mechanisms. The different breaking dynamics are investigated in terms of their effects on the dynamics of the ISW and the interaction of the ISW with the sloping boundary. The bulk entrainment parameter and the mixing efficiency are used to characterize the effects of the different breaking mechanisms on the initially stably-stratified fluid. The larger entrainment is observed for the surging case as a consequence of the large gravity current flowing upslope, while the plunging breaker shows the relatively largest amount of mixing, which is mostly induced by rear-edge overturning in the onshore direction. The bed shear stress and the local flux of sediments entrained from the bed are estimated to investigate the effects of the ISW breaking on the inclined surface. The collapsing breaker mechanism generates boundary layer separation, which in turn induces whirling instabilities. Results also show that the ISW interaction with the inclined surface occurs in its close proximity for collapsing breaker mechanism, which explains why the largest bed shear stresses and sediment resuspension are predicted in the simulation where a collapsing breaker mechanism is observed.

Further laboratory experiments are performed in order to investigated the role of the unsteady behavior of solitary waves interacting with a mobile bottom. The sandy bedforms triggering process induced by surface solitary waves in shallow water conditions is analyzed. The standard lock-release method is applied in a flume, producing an initial displacement between the free surfaces that are divided by the gate. The quick removal of the gate induces the generation of a single surface solitary wave which interacts with the sandy particles composing the original flat bottom. For 15 different cases, the effect on the mobile bed of 400 consecutive waves with the same features is investigated. From the boundary layer theory, it is possible to relate the wave stroke action to the bedforms triggering process. Nearby the bottom, the adverse horizontal pressure gradient results to be strongly affected by the horizontal velocity induced by the wave. It induces a reverse flow and a boundary layer separation. Depending on the wave and sand features and on the water depth, the boundary shear stress induced by the reverse flow can exceed the critical value, inducing the back motion of the sand particles. Under these circumstances, the first erosion zones form, and they gradually evolve in asymmetric dunes because of the action induced by the following waves. The breaking generation mechanism results linked to the wave features and their effect at the bottom.

Contents

List of Figures

List of Tables

Chapter 1

Introduction

The change of density and pressure with depth in a stratified fluid involves energy costs for the fluid to move against or with the direction of gravity: buoyancy forces act restoring the vertically displaced fluid. Two layers generally approximate the vertical density profile of the ocean: the well-mixed surface region and the underlying weakly stratified deep water [*Garrett*, 2003; *Pedlowsky and Miles*, 2004]. A thin, strongly stratified layer called *pycnocline* separates them. It is characterized by a sharp change in density with depth, due to differences in temperature or salinity. It represents an extremely stable zone, acting as a barrier for surfaces processes. Below the pycnocline, changes in salinity or temperature are very small. Seasonal climatic excursions, wind stress, surface wave breaking and convection lead the ocean surface layer to be homogenously or weakly stratified [*Garrett*, 2003; *Pedlowsky and Miles*, 2004; *Sutherland and Ivey*, 2013]. Both in freshwater lakes and in oceans, temperature, salinity and pressure change with depth. However, it is mostly the temperature variations, which affect the density change: a strongly stratified layer, in which the temperature decreases rapidly with depth, represents the *thermocline.* Depending upon latitude and season, the thermocline region extends downward as far as about 100 m, approximately from 50 to 150 m depth. In the Mediterranean Sea, for instance, the thickness of the surface mixed layer is typically around 100 m, with some peaks and lows that reach $\sim$ 200 m and $\sim$ 30 m, respectively, depending on the season [*D'Ortenzio et al.*, 2005]. During summer, the large density contrast between the warm surface and the cooler deep waters inhibits the vertical mixing: the thermocline results to be shallowest and strongly stratified. In winter, instead, the surface cooling leads the thermocline to have weaker stratification and greater thickness. In estuaries, the less dense fluid release, into the ocean, induces the formation of the *halocline*, a stratified layer resulting strictly from increasing saltiness with depth.

For surface gravity waves, the fluid oscillates around its equilibrium position because of buoyancy and gravity acting on a vertically displaced fluid. Likewise, the oscillation of the interface between more dense and less dense fluids, within the water body, gives rise to internal gravity waves (IGWs). Internal gravity waves, thus, need a stably stratified fluid to exist. Any disturbance that results in an alteration of the stable stratification of the ocean could cause large amplitude undulations of the pycnocline, giving rise to internal waves that propagate due to the consequent action of the gravitational restoring forces on the vertically displaced fluid.

It is quite difficult to directly investigate the features of internal waves by field observations [*Alpers and Salusti*, 1983; *Artale et al.*, 1990]. Internal solitary wave packets become visible when their propagation induces sea surface manifestations. Although they propagate along a pycnocline in the interior of the ocean, nonlinear internal waves alter the sea surface roughness, making them readily detectable in satellite imagery. Currents within the nonlinear internal wave produce convergent and divergent zones on the surface that move in phase with the internal wave's subsurface crests and troughs. These zones cause variations in sea surface roughness that appear as distinctive features in both synthetic aperture radar (SAR) and optical sunglint imagery. *Alpers et al.* [1996] show, by SAR images, the presence of a group of surface waves caused by internal wave train propagating out of the Strait of Gibraltar towards the Atlantic Ocean.

Internal gravity and solitary waves generation mechanisms

The understanding of nonlinear internal wave generation begun with the study of *Maxworthy* [1979] focused on the analysis of the lee wave generation at an underwater sill or a bank. In this work, the characterization of the hydraulic state of a stratified shear flow is based on the internal Froude number (F), a dimensionless quantity defined as the ratio of the velocity of a fluid to the relative velocity of a small-amplitude internal wave on the interface. When a stratified flow propagate over a sill or bank, the sloping seabed imparts a vertical component, displacing the pycnocline. When the flow is subcritical ($F< 1$), the wave velocity is greater than the flow velocity, thus, the information can move upstream (opposite the direction of flow); when the flow is subcritical ($F> 1$), the fluid velocity is greater than the wave velocity and the information can only move downstream (in the direction of the flow). When the Froude number is critical ($F = 1$), a disturbance on the interface will remain stationary accumulating energy through resonance. When a moving fluid encounters a change in depth, the seabed feature provides the variation in depth necessary to set up the transition zone between subcritical and supercritical flow. A stationary lee wave of depression forms in the pycnocline downstream of the sill, characterized by a large phase speed relative to the moving water, such that it remains stationary relative to the bank. Sills and banks are among the principal generation regions of nonlinear internal waves in the ocean, for example the Camarinal and Spartel sills induce the generation of the nonlinear internal waves at the Strait of Gibraltar [*Armi and Farmer*, 1988].

IGWs, however, are primarily generated by the interaction between tidal flow and the bottom topography[e.g., *Niwa and Hibiya*, 2001]. For this reason, IGWs could be mainly found within estuaries, straits, continental margins and the coastal oceans [*Brandt et al.*, 1999; *Marullo and Santoleri*, 1986; *Stashchuk and Vlasenko*, 2009]. Baroclinic tidal generation occurs in a similar manner to the lee wave mechanism, where seabed features induce vertical components into a tidal flow causing pycnocline vertical displacements. The internal tide may propagates away from the generation zone with an initially sinusoidal shape, but, if it is sufficiently energetic, it will steepen, break, and evolve into nonlinear internal waves. The gravitational instability can be caused, also by the action of strong winds [e.g., *Simmons and Alford*, 2012] and by river plumes [*Nash and Moum*, 2005]. IGWs occur in different forms: vertically propagating narrow internal wave beams and horizontally propagating modal waves. The latter may develop in isolated waves of fixed form. During the propagation of the internal tides, IGWs could steepen due to nonlinearity, giving rise to a train of much shorter strongly nonlinear internal solitary waves (ISWs), or solitons. The main characteristic of the ISWs is the balance between nonlinear effects, which tend to steepen the leading edge of the wave profile, and nonhydrostatic dispersive effects, which cause its flattening [*Korteweg and De Vries*, 1985]. These forces act simultaneously and allow the single wave to preserve its shape during motion [*Artale et al.*, 1990; *Grue et al.*, 2000]. The velocity field of an ISW induces water parcels motion (in the same direction of the wave in the upper layer, and in the opposite direction in the lower one), because their path is composed by open orbits [*Bakhoday-Paskyabi*, 2015]. For this reason, ISWs are able to transport energy, in terms of mass and heat during their propagation. The hydrodynamic soliton was first observed and described by Russell: in 1834, he reported the formation of a singular, unchanging hump on the surface of a Scottish canal, generated when a towed barge was brought to a sharp halt. Following the wave for several miles on horseback, he was surprised on how it retained a constant shape for a long distance. He performed laboratory experiments in order to produce the first quantitative description of the solitary wave [*Russell*, 1844]. In 1895, Diederik Korteweg and Gustav de Vries produced a generic equation accounting (to lowest order) for the wave properties of dispersion and nonlinearity and its soliton solution. *Osborne and Burch* [1980] analyzed the internal waves in the Andaman Sea during the 1970s, linking the properties of solitary waves to the phenomena of oceanic nonlinear internal waves.

Breaking internal solitary waves

In recent years, scientific research has focused on the interaction between ISWs and the continental shelf/slope, studying the particular conditions that cause the breaking of shoaling internal waves and their consequent effects. The continental shelf is a shallow gently sloping region lying between the coast and the shelf break (typically at depths $100 - 200$ m), beyond which the water deepens rapidly down the steep continental slope, with an average angle of 2° to 4°, to the deep ocean [*Cacchione et al.*, 2002]. In these regions, two homogeneous layers of different density usually approximate vertical density profile. This density structure is commonly described by the Boussinesq parameter, defined as the ratio of the density difference between the two layers and a reference density. In the coastal oceans, the typical value of the Boussinesq parameter is 0.03 [*Chen et al.*, 2007]. The continental shelf/slope region is characterized by the presence of strong barotropic tides, currents, eddies, and complicated bathymetry. For these reason, waves of many frequencies and geometric features, form [*Nash et al.*, 2004]. This environment is an important source of food, is a location for industrial activity and is subject to nutrient, sediment and pollution loads from the adjacent land. The breaking and dissipation of internal waves have implication for all.

Breaking mechanisms beneath the shoaling waves induce both mixing and near-bottom turbulence that could cause the suspension and redistribution of the bed material [*Arthur and Fringer*, 2014; *Droghei et al.*, 2016]. Internal waves can compromising sub-sea oil and gas drilling operations [*Osborne et al.*, 1978], and they can have important consequences for underwater sound propagation [e.g., *Zhou et al.*, 1991]. Shear stress induced by solitons may even destabilize drill pipes during offshore operations. ISWs may also affect nutrients transport towards the surface, in particular when mixing occurs [*Lai et al.*, 2010], and also may cause lateral transport of nutrients [*Lamb*, 1997]. Consequently, internal solitary waves represent a crucial phenomenon on the continental shelf/slope providing an important link between the large and the small scale at which their energy could be partially dissipated. The recent reports from the Intergovernmental Panel on Climate Change (IPCC), regarding the climate change that is occurring, is directly acting on the factors that affect the development and the characteristics of ISWs [*Stocker et al.*, 2013; *Core Writing Team and Meyer*, 2014a, b]. All international organizations responsible for climate system control draw attention to the most obvious effects that are occurring. The rise in global temperature [*Kraucunas*, 2006; *Peterson and Baringer*, 2009], the shrinking ice sheets, the glacial retreat [*Church and White*, 2006] and the warming oceans [*Levitus et al.*, 2009] are just some of the main consequences of this change. In this context, the action of ISWs can have a significant importance. *DeCarlo et al.* [2015] document what happens to ISWs in the breaking phase and stress their relevant action in global climate. They analyzed how these waves help move a huge amount of energy from Luzon Strait across the South China Sea. Warming in the upper layer of the ocean enhances wave activity: for large density difference between the surface and the deep layers, an increase of the wave energy is expected, inducing more energetic effects in the breaking phase. For these reasons, wave action is expected to increase in those regions, through the 21st century, with consequent mitigation of the climate change impacts on coastal ecosystems.

Many experimental and numerical studies have focused on the breaking of shoaling internal waves in continuous two-layer stratifications. By defining an external forcing, such as a tide, it is possible to analyze the evolution of long internal waves in a two-layer fluid system. This topic has attracted much interest in the past: *Osborne and Burch* [1980] and *Artale et al.* [1990] used the well-known Korteweg and de Vries (KdV) equation which describes the waveform for weakly nonlinear internal waves propagating in straits of uniform and shallow depth in two-layer stratified fluid system. According with the KdV equation, the undulation of the pycnocline induced by an ISW takes the form of a squared hyperbolic secant. The experimental study conducted by *Grue et al.* [1999] shows that the KdV theory is valid for amplitudes up to 0.4 times the shallow water depth. The observed oceanic ISWs show higher vertical displacement. *Alpers et al.* [2008] show the density distribution of the water column of the Strait of Messina measured by shipborne sensors during the passage of a highly nonlinear internal wave packet: the vertical displacement is approximately 3 times the shallow water depth.

For highly nonlinear waves the wave structure is significantly different from that predicted by KdV theory. Moreover, it is quite difficult to analyse the ISWs features, and their shoaling and breaking processes, by field observations, because special/time resolution of field data limit the obtained results [*Alpers and Salusti*, 1983; *Alpers et al.*, 1996; *Artale et al.*, 1990; *Brandt et al.*, 1999; *Klymak and Moum*, 2003; *Scotti and Pineda*, 2004; *Davis and Monismith*, 2011; *Walter et al.*, 2012; *Droghei et al.*, 2016]. For this reason, experimental and numerical studies on shoaling/breaking ISWs, have been widely carried out by using small-scale idealized domains. Shoaling and breaking internal waves on slopes have been extensively investigated also by numerical models, both at the field scales [*Lamb*, 2002; *Bourgault et al.*, 2007; *Vlasenko and Stashchuk*, 2007; *Walter et al.*, 2012] and at laboratory scales [*Aghsaee et al.*, 2010; *Vlasenko and Hutter*, 2002; *Venayagamoorthy and Fringer*, 2007]. Moreover, several high-resolution 3-D modelling studies have examined turbulence and mixing during internal wave breaking on slopes: the numerical simulations (DNS) of *Gayen and Sarkar* [2010] and *Arthur and Fringer* [2014] and the large-eddy simulations (LES) of *Gayen and Sarkar* [2011].

The experiments conducted by *Kao et al.* [1985] concerned with the transition of ISWs from deep to shallow ambient fluid, passing over a slope. They evaluated the loss of energy due to breaking under these circumstances. In their experiments, the pycnocline never intersects the sloping boundary. *Helfrich and Melville* [1986] studied experimentally the transition of ISWs from waves of depression in deep water to waves of elevation over the slope. Their experiments showed mixing during the waves transition. *Helfrich* [1992] experimentally investigated the approach of a solitary wave toward a uniform slope, focusing on the study of boluses caused by the shoaling of ISWs. The ratio between the ISWs amplitude and the shallow water depth assumed values not so larger than 0.4. *Michallet and Ivey* [1999] analyzed the energy loss due to mixing induced by shoaling large amplitude ISWs over a sloping boundary, examining slopes between 0.069 and 0.214. *Boegman et al.* [2005] performed laboratory experiments in order to analyze the shoaling process of an internal wave-train over a uniform slope (0.097 and 0.145). They introduced the wave slope as the parameter able to describe the ISWs geometric features. It represents the ratio between the wave amplitude and the wavelength. The wavelength is defined as the ratio between the wave surface and the wave amplitude, in accordance with the KdV theory. They classified different breaking types depending on the Iribarren number (Ir), defined as the ratio between the topographic slope and the square root of the wave slope. However, this way to estimate the characteristic wavelength is quite misleading since they assume that the generated waves agrees with the theoretical KdV structure. This brings to the following breaking domains: plunging breakers ($Ir = 0.45 \div 0.75$) and collapsing breakers ($Ir > 0.75$). *Aghsaee et al.* [2010] used 2-D numerical simulations in order to explore the dynamics of large amplitude ISWs shoaling on a uniform slope. They investigated the slope range $0.01 \div 0.3$, generating internal waves with an amplitude from 0.2 to 2 times the shallow layer depth. They characterized the breaking regimes introducing time scales for each main process involved in the breaking event. Even if they evaluated Ir for each case, they did not use that parameter to classify the different breaking mechanisms. They observed that, for a defined wave, the increase of the topographic slope changes the breaking type. *Sutherland and Ivey* [2013] performed laboratory experiments on large amplitude ISWs shoaling on a constant slope. Their analyses focused on the prediction of the maximum breaking depth and the consequent propagation upslope of the dense layer as a bolus. They defined the wavelength as the half-width at the half maximum. They used Ir in order to identify the different breaking regimes: plunging breakers occurred if $Ir < 0.3$, collapsing breakers for $0.3 < Ir < 0.7$ and surging breakers for $0.7 < Ir < 1.5$. The marked difference of the values that identify breaking domains between *Boegman et al.* [2005] and *Sutherland and Ivey* [2013] is due to the different definition of the wavelength. In this work, large amplitude internal waves are experimentally investigated, broadening the parameters range explored in the past both numerically and experimentally. One aim of this study is to distinguish the breaking mechanisms by evaluating the parameter λ, extensively used in literature to define the ISW wavelength, defined as the ratio between the wave surface and the wave amplitude, as in *Aghsaee et al.* [2010]. This allows to define an experimental set of Ir that will be used to describe breaking mechanisms, merging the numerical/theoretical approaches with the classic experiments on ISW breaking [*Sutherland and Ivey*, 2013; *Boegman et al.*, 2005]. The generated ISWs are characterized by wave amplitudes up to 4 times the shallow layers depth, well beyond the KdV regime. For this reason, results may be efficiently applied to interpret the physical processes involved in real field observations. The investigated slope values ranged between 0.15 and 0.95. However, it must be stressed that some relevant parameters are not scaled (e.g., Reynolds numbers, surface tension, vapor pressure). This might introduces additional scale effects during the breaking processes that can not be accounted in laboratory experiments. This study aims to understand how to configure the initial experimental conditions in order to obtain a wave of desired geometrical characteristic, and for each generated ISW, how to configure the sloping bottom in order to induce a particular type of breaking mechanism (i.e., plunging, collapsing and surging). Moreover, real breaking of the ISWs propagating towards the North of the Strait of Messina (Italy) are analyzed. In this region, the characteristics of both sea bottom and wave parameters suggest that the plunging breakers are expected to occur. For this reason the analysis focused more in detail on plunging breakers, by investigating the effect of internal wave breaking in terms of increase of the pycnocline thickness. The idealized experimental procedure allows to recognize and characterize the physical processes involved in the real field, rather than simulating real field geometries and conditions. By using Large Eddy Simulation (LES) numerical model ISWs shoaling and breaking effects are examined, in terms of mixing and entrainment induced over the sloping bottom. Being each breaking mechanism characterized by different dynamics, the motivation of the work is to distinguish different ISWs braking types depending on the effects they induce.

The role of solitary waves in bedforms generation

Large amplitude internal waves in naturally occurring stratified fluids induce currents throughout the water column and hence have the potential to drive instability. They can induce turbulent transition within the bottom boundary layer (BBL), and hence material exchange across it. There is evidence of bed sediment resuspension in the wake of ISWs traveling over ocean shelves [*Klymak and Moum*, 2003; *Bogucki et al.*, 2005; *Bourgault et al.*, 2014; *Quaresma et al.*, 2007]. Understanding this process is of great interest due to the importance of sediments on aquatic biogeochemistry and acoustics [*Carr et al.*, 2008], and for bedforms generation [*Droghei et al.*, 2016]. Field observations [e.g., *Bogucki et al.*, 2005], laboratory experiments [*Boegman and Ivey*, 2009] and numerical simulations [e.g., *Stastna and Lamb*, 2002; *Diamessis and Redekopp*, 2006; *Stastna and Lamb*, 2008; *Aghsaee et al.*, 2012; *Olsthoorn and Stastna*, 2014] suggest that global instability of the wave-induced boundary layer [*Batchelor et al.*, 2000], where coherent vortices are shed from the separation bubble in the adverse pressure gradient region, is the main resuspension mechanism beneath ISWs. *Bogucki et al.* [1997] were the first authors to prove the occurrence of boundary layer separation, having observed enhanced rates of resuspension of sedimentary material associated with waves of elevation on the Californian Shelf near Los Angeles. The observations of *Bogucki et al.* [2005] prompted new investigations: they invoked global instability as the causal mechanism of their observed benthic stimulation. Two-dimensional direct numerical simulations have shown that the shed vortices will increase the instantaneous bed stress and enhance turbulent vertical velocities [e.g., *Stastna and Lamb*, 2002; *Diamessis and Redekopp*, 2006; *Aghsaee et al.*, 2012]; thus, providing a potential mechanism for resuspension. In particular *Diamessis and Redekopp* [2006] performed numerical simulations of both ISWs of elevation and depression propagating over a flat boundary. They showed that the global instability can occur within the wave-induced boundary layer aft of the wave, in the adverse pressure gradient region, for wave amplitudes exceeding a critical value. In such cases, coherent vortices appear in the boundary layer and are shed upward into the main water column. They found that for waves of a high enough amplitude (i.e., high enough Reynolds number), the bursting of the separation bubble in the BBL led to vortices being shed from the bottom boundary that reached as high as 30%-35% of the water depth, thus providing a means for sediment resuspension in shallow waters. However, there is some uncertainty regarding the use of weakly nonlinear theory for initializing the simulations. Laboratory experiments have shown elevated Reynolds stresses above the viscous sublayer in the adverse pressure gradient region [*Skåre and Krogstad*, 1994; *Boegman et al.*, 2005]. In 2-D particle image velocimetry (PIV) experiments of shoaling ISWs, *Boegman et al.* [2005] observed a correlation between the elevated Reynolds stress and particle resuspension. This was in agreement with previous studies implying that the Reynolds stress correlates with the vertical diffusivity, leading to upward flux of sediments [*Soulsby et al.*, 1994; *Bogucki et al.*, 1997]. Recently, *Aghsaee and Boegman* [2015] performed laboratory experiments on ISWs of depression moving over a flat bottom. They showed that not only does the viscous bed shear stress need to exceed the critical value (the Shields criterion) in order to resuspend sediment, but the vertical velocities need to be an order of magnitude larger than the settling velocity of the sediments. In the present work, the effect of surface solitary waves on an initially flat mobile bottom is experimentally studied. By considering shallow water conditions, I investigate how the unsteady behavior of solitary waves affects the bottom boundary layer. We also analyzed the relation between the solitary wave geometric features and the velocity and pressure field induced at the bottom.

Several studies focused on transport due to ISWs breaking on slopes [*Helfrich*, 1992; *Nakayama and Imberger*, 2010; *Nakayama et al.*, 2012; *Bourgault et al.*, 2014; *Arthur and Fringer*, 2016]. *Helfrich* [1992] investigated the onshore transport associated with the dense fluid flowing upslope as a gravity current after the breaking event takes place [*Lombardi et al.*, 2015]. *Nakayama and Imberger* [2010] and *Nakayama et al.* [2012] quantified trans-

port by means of a time-averaged residual circulation: their laboratory experiments and numerical simulations showed that transport occurs onshore in the upper layer and offshore in the lower layer. *Arthur and Fringer* [2016] distinguished an onshore transport due to the upslope flow of the denser fluid and an offshore transport induced by an intrusion of mixed fluid propagating upstream. As generally observed in the coastal regions of oceans, these intrusions resemble intermediate nepheloid layers (INLs), inducing offshore transport of benthic material into the interior of the water column [*McPhee-Shaw*, 2006].
Formation and propagation of internal bores in two-layer stratified environments were studied based on eddy resolving simulations by *Borden et al.* [2012b, a]. Shoaling and breaking internal waves on slopes have been extensively investigated numerically, both at field scales [*Lamb*, 2002; *Bourgault et al.*, 2007; *Vlasenko and Stashchuk*, 2007; *Walter et al.*, 2012] and at laboratory scales [*Vlasenko and Hutter*, 2002; *Venayagamoorthy and Fringer*, 2006, 2007; *Aghsaee et al.*, 2010]. Moreover, several high-resolution, 3-D numerical studies have examined turbulence and mixing during internal wave breaking on slopes. One can mention the direct numerical simulations (DNS) of *Gayen and Sarkar* [2010] and *Arthur and Fringer* [2014, 2016] and the large-eddy simulations (LES) of *Gayen and Sarkar* [2011] among others.

The present thesis is organized as follows: 2 presents the laboratory experiments on ISWs interacting with a uniform sloping boundary. We investigate the generation, propagation, shoaling and breaking processes. We focus on plunging breakers, investigating the breaking effects in terms of increase of the pycnocline thickness; in 3, we numerically study the different dynamics characterizing each breaking mechanism. By using LES numerical model, we preliminary evaluate the instantaneous mixing efficiency and the mixed layer entrainment parameter. The spatial and temporal distribution of the bed shear stress over the incline is also investigated, in order to provide an estimate of the potential of the ISW to induce sediment entrainment. 4 shows the experimental study on sandy dunes generated by surface solitary waves, and the bedforms generation conditions. 5 presents a discussion of the obtained results and the conclusions.

Chapter 2

Breaking internal solitary waves

This Chapter presents the analysis of large amplitude internal waves in shallow water condition generated by laboratory experiments by applying the standard lock release method on a 3 m long, 0.3 m high and 0.2 m wide Perspex tank.
Empirical relations are obtained between the initial setting parameters and the generated ISWs main feature (i.e. amplitude, wavelength, surface and celerity). The small-scale experimental apparatus is thus properly set up in order to generate ISWs with well-defined geometric and kinematic features Once an ISW of depression interacts with a sloping boundary, different breaking mechanism could occur. Depending on how the wave shoals, different dynamics develop affecting the consequent breaking event. As widely used in literature [e.g., *Sutherland and Ivey*, 2013], the breaking domains are defined by using the Iribarren number. Plunging, collapsing or surging breakers occur depending on geometric wave and inclines features.
Finally, I discuss real breaking of the ISWs propagating towards the North of the Strait of Messina (Italy), where the characteristics of both sea bottom and wave parameters suggest that the plunging breakers occur in this region. An image analysis technique applied on *ad hoc* experiments allow us to evaluate the instantaneous density field during the plunging breaking of several ISWs. Results show that the effects of the breaking, in terms of increase of the pycnocline thickness, are non-linearly related to the Iribarren number. The present Chapter is organized as follows: in Section 2.1 the laboratory facilities used to generate a single solitary wave of depression propagating in the wave flume are introduced. In Section 2.2 the laboratory model is described. Section 2.3 shows the wave field during the propagation

phase and during the shoaling process, and the description of the different breaking mechanisms that could happen are described. Finally, Section 2.4 introduces the experiments performed in order to analyze the case of the wave packets propagating toward the North of the Messina Strait, also discussing mixing process.

2.1 Experimental setting

A series of laboratory experiments are performed in a Perspex tank following the standard lock-release method [*Kao et al.*, 1985]. The 0.2 m wide flume has a length $L_t = 3.0$ m and a height $H_t = 0.3$ m (Fig. 2.1a).
A thin, vertical, removable Perspex gate divides the flume into two regions: the lock on the left-hand side, and the channel, which represents the ambient fluid region in which the waves propagate (Fig. 2.1a). The flume is filled in order to obtain a stratified two-layer fluid system of fresh water in the upper layer and brine water in the lower layer. The tank is first filled with a solution of sodium chloride (NaCl), creating the lower layer of uniform density ρ_2. Later, fresh water is poured slowly into a funnel inlaid in a sponge float, generating the upper layer of uniform density ρ_1. This process has to be done very slowly to minimize the thickness of the pycnocline. The fresh water was dyed by Methylthioninium chloride ($C_{16}H_{18}Cl\ N_3S$) in order to visually distinguish the two layers. A pycnometer is used to measure the density of the saline mixture and the dyed fresh water, with an error of 0.2%.

The vertical gate is placed up to a given distance from the bottom, such that the hydraulic continuity between the lock and channel regions is always insured. A displacement η_0 between the pycnoclines of the two regions is produced by adding fresh water to the lock water surface. During the tank-filling phase, part of the brine water flows below the gate spilling in the ambient fluid region, as long as the two sides reach a stable hydrostatic condition. The final setting presents two different stratifications on the left- and the right-hand side of the gate (Fig. 2.1a); depending on the displacement η_0 and on the ratio ρ_2/ρ_1, a displacement δ forms between the two free surfaces. For all the performed experiments $\delta = 2 \div 4$ mm.
By removing the gate, a gravity collapse happens and an ISW of depression forms and propagates towards the right hand side of the tank [*Chen et al.*, 2007], as schematized in Fig. 2.1b.
The geometrical parameters that define the initial setting of each experiment are (Fig. 2.1a): the lock length x_0, the displacement between the pycnoclines η_0, the fresh and brine water layer thicknesses h_1 and h_2, and the total water depth $H = h_1 + h_2$. A ruler is used to measure the lower layer thickness (h_2), and the total water depths. Once h_1 and h_2 are evaluated, the midpoint of the pycnocline in the ambient fluid region is known, and it is used to identify the pycnocline position. All the experiments are recorded with a CCD (Charged Coupled Device) camera with a frequency of 25 Hz and a spatial resolution of 1024 × 668 pixels, located at a fixed distance from

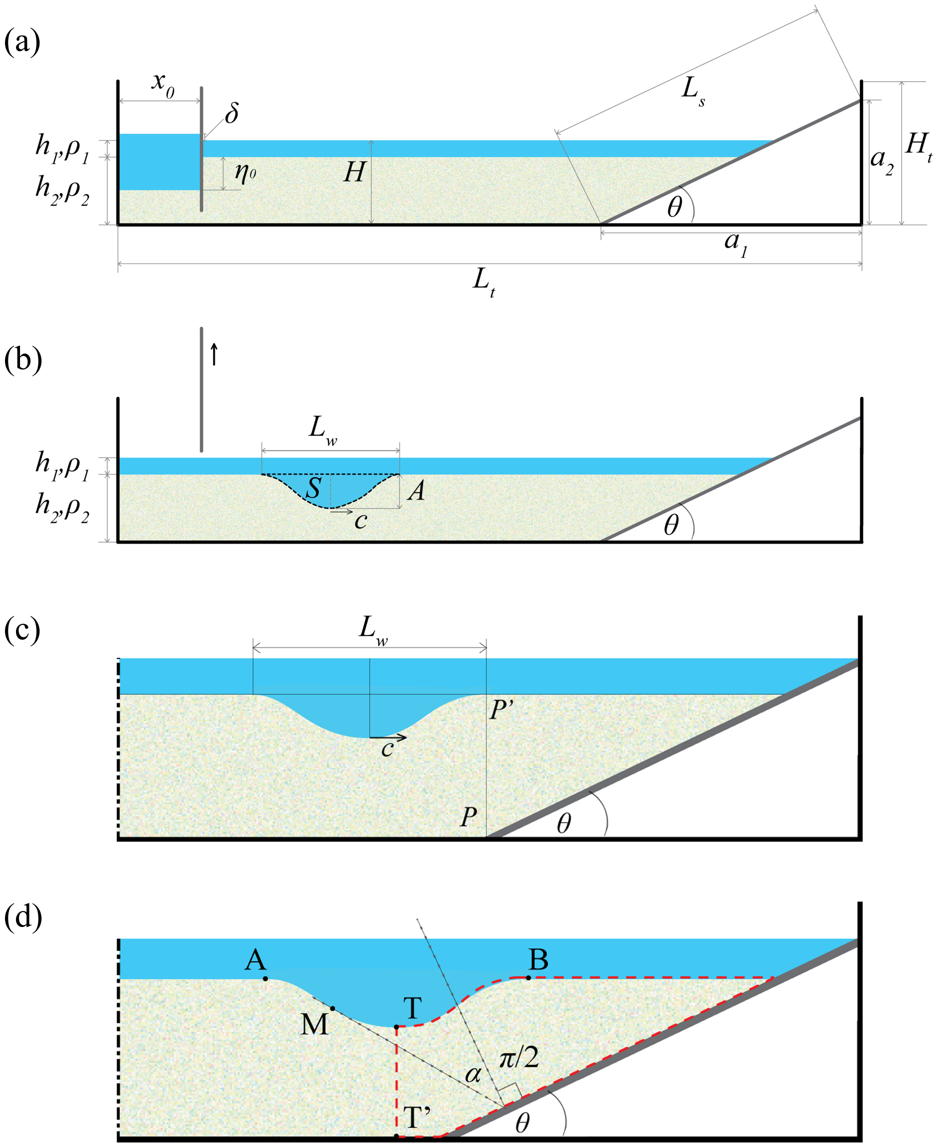

Figure 2.1: Schematic view of the experimental apparatus: the initial setting (a) and the wave generated after the removal of the gate (b). The wave surface S is bounded by dashed lines. Sketch of the incident wave (c). Point P defines the position of the toe of the slope, and point P' is its vertical projection on the pycnocline. Sketch of the shoaling phase (d). Point T is the wave trough, point T' is its vertical projection at the bottom; points A and B define the wavelength; point M is the midpoint of the rear edge of the wave; α identifies the angle between the trailing edge slope and the line perpendicular to the sloping boundary. The dense fluid confined on the right hand-side of the segment TT' (dashed boundary) represents the confined fluid between the wave and the slope.

the lateral wall of the tank, so that each pixel has a resolution of about 3 mm. From image analysis, the pycnocline thickness and the midpoint of the pycnocline in the lock region are obtained. Depending on the filling process accuracy, the initial pycnocline thickness ranged between 1% and 9% of the total water depth H.

A slope, defined by the angle θ, is located at one end of the tank (Fig. 2.1a) in order to analyze the different breaking mechanisms of the ISWs. The slope length is $L_s = 0.845$ m, and the angle θ is obtained by measuring the legs a_1 and a_2 (Fig. 2.1a; Tab. 2.1).

All the experiments are carried out with two homogeneous fluids in order to obtain a density profile as similar as possible to the conditions occurring in ocean, where solitary waves are observed. The brine water in the lower layer presents a homogeneous density ρ_2 that ranges between 1029÷1032 kg/m^3. The density of the upper layer, for all the performed experiments, is 1000÷1001 kg/m^3. The density difference between the salt and the fresh water therefore ranged between 29 and 32 kg/m^3, obtaining a Boussinesq parameter typical of the coastal oceans (0.029÷0.032).

In order to visualize the direction of the horizontal velocity during the shoaling process, some particles of potassium permanganate are disposed as a tracer along particular locations over the slope. Some particles decant and collect over the slope, and they are used to qualitatively understand the bed material redistribution process caused by the wave breaking. An image analysis technique is used to measure the instantaneous pycnocline position [as in *Robinson et al.*, 2013; *Lombardi et al.*, 2015; *Ottolenghi et al.*, 2016a, b; *Ozeren and Altinakar*, 2016; *Musumeci et al.*, 2017]. It was possible to obtain both geometric and kinematic features of the ISW, such as the wave amplitude A, the wave surface S, the wavelength L_w, and the celerity c (Fig. 2.1b). The wave celerity is evaluated as the first derivative of the trough's position, deduced by image analysis. The error committed for lengths measurements is about 1 pixel, thus the celerity values are affected by an error of 0.1 cm/s. The characteristic wavelength λ is defined as in *Michallet and Ivey* [1999]:

$$\lambda = \frac{1}{A} \int_{-\infty}^{+\infty} \eta(x)\,\mathrm{d}x = \frac{S}{A} \tag{2.1}$$

where $\eta(x)$ is the pycnocline position (m), S the wave surface (m^2) and A the wave amplitude (m).

All the generated ISWs follow the shallow water approximation [*Osborne* *and Burch*, 1980]:

$$\frac{H}{\lambda} \ll 1 \tag{2.2}$$

The large amplitude condition, compared to the surface layer thickness [*Bourgault et al.*, 2014], can be defined as:

$$\frac{A}{h_1} > 0.4 \tag{2.3}$$

For all the performed experiments, the ratio in Eq. 2.3 ranges between 0.6 and 4.
For additional laboratory experiments, the density fields are evaluated using dye as tracer. For each pixel of the image, a relation between the amount of the uniformly distributed dye in the tank, and the grey scale values, is obtained by acquiring, at the end of each experiment, several images characterized by a known concentration of dye [as in *Nogueira et al.*, 2013a, b, 2014; *Theiler and Franca*, 2016]. The error in the evaluation of the instantaneous density fields is estimated in 0.1 kg/m^3, by considering the ratio between the maximum range of density and the gray scale levels.

2.1.1 Waves generation and propagation over the horizontal bottom

Starting from the gate lifting, several phases can be identified in order to describe the different processes involved during each experiment (Fig. 2.2). The first phase characterizes the wave generation: the gate removal induces a gravity collapse, and the light-fluid trapped in the lock region begins to move forward into the ambient fluid (Fig. 2.2a-c).

After a certain time, the initial disturbance (Fig. 2.2d) develops into an internal solitary wave of depression [*Artale et al.*, 1990], characterized by symmetric geometric features (Fig. 2.2e). The generation phase ends when the ISW is completely formed and starts to maintain approximately constant its shape and its main features (i.e. amplitude, wavelength and celerity), propagating over the horizontal bottom. During the propagation phase, the wave celerity is constant, while the other wave properties could slightly change. For the performed experiments, starting from the time at which the wave assumes a constant, homogeneous shape, a mean decrease in amplitude of about 8% and a mean increase in wavelength of 7% occurred. Being ISWs characterized by a balance between nonlinear and dispersive effects, this broadening process is likely due to the friction effects. The evolution of λ and A during the motion of an internal wave over the horizontal bottom shows that the wavelength increases of about 6% of the initial value,

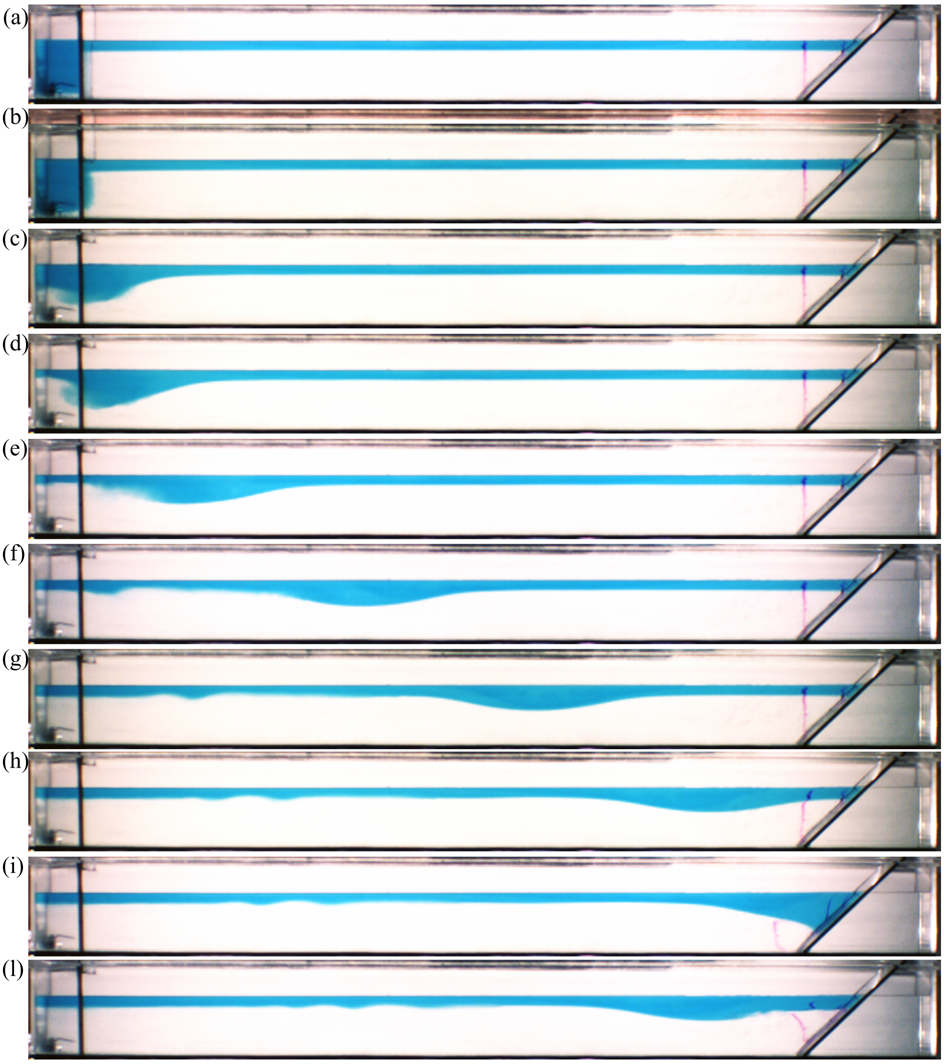

Figure 2.2: Consecutive snapshots captured during the experiment Run 38 ($h_1 = 3.3$ cm, $h_2 = 16.7$ cm, $A = 4.8$ cm, $\lambda = 43.8$ cm, $c = 11.0$ cm/s, $s = 0.952$). a) $t = 0$ s; b) $t = 0.5$ s; c) $t = 2.3$ s; d) $t = 3.4$ s; e) $t = 7.2$ s; f) $t = 11.0$ s; g) $t = 16.0$ s; h) $t = 21.0$ s; i) $t = 23.4$ s; l) $t = 28.2$ s.

while the amplitude decreases of about 9.5% of the initial value, reaching approximately constant values starting from 13 seconds after the gate removal (Fig. 2.3).

During the propagation of the leading wave, secondary ISWs can form (Fig. 2.2f-h). However, among all the performed experiments, only few runs showed this occurrence. In Fig. 2.2g the leading wave has an amplitude $A = 4.8$ cm and a celerity $c = 11$ cm/s, while the secondary wave features are: $A_s = 1.8$ cm and $c_s = 5.4$ cm/s. Secondary waves are characterized by a very small amplitude, up to one fifth of the amplitude of the leading waves. The celerity of secondary waves eventually generated after the gate removal, is very small, compared to the celerity of the leading wave. This is in accordance with the KdV theory: the wave celerity depends on the wave amplitude [*Sutherland and Ivey*, 2013], thus ISWs with larger amplitude propagate faster. Since the amplitude of secondary waves is very small, these quickly separate from the leading wave, reaching the sloping boundary always after its breaking (Fig. 2.2i). Because of the initial turbulence generated during the gate removal, and the eventual presence of secondary waves, the volume of the generated leading waves is lower than the initial volume $x_0\ \eta_0$ (meanly 82%).
Once the wave reaches the sloping boundary, the breaking event occurs. During this phase, part of the wave is reflected (Fig. 2.2i). Depending on the breaking mechanism, the reflected wave assumes different geometric and kinematic features. In presence of a vertical front wall, the wave would be completely reflected, and no breaking would occur. Once a sloping wall is introduced, the interaction between the wave and the incline causes breaking. Most of the incident wave energy is lost due to turbulent mixing, and only a part of the wave is reflected.

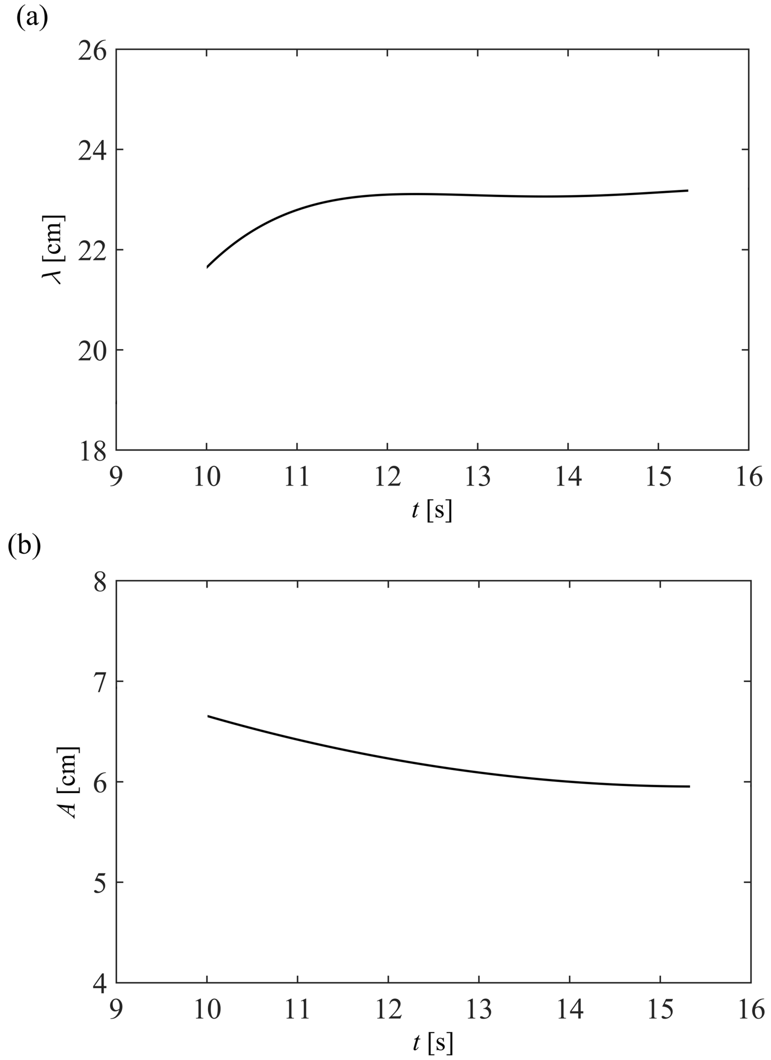

Figure 2.3: The broadening process during the propagation phase. Time series of characteristic wavelength λ (a), and wave amplitude A (b), for a generated internal solitary wave. The evaluation of the wave features starts as the wave starts to maintain the same shape during the propagation (i.e. after 13 s from the gate removal).

INITIAL EXPERIMENTAL SET UP PARAMETERS	Values			
Total water depth	H [cm]	28	20	
Layers thickness ratio in the channel	r_0	5	7	
Pycnocline displacement	η_0 [cm]	10	15	
Lock length	x_0 [cm]	10	15	20
Slope angle	θ [°]	$9 \div 60$		
Slope angle	a_1 [cm]	$42.3 \div 83.4$		

ISW'S CHARACTERISTICS	Ranges	
Wave Amplitude	A [cm]	$2.9 \div 5.7$
Characteristic wavelength	λ [cm]	$25.6 \div 55.6$
Wave celerity	c [cm/s]	$8.0 \div 13.7$

Table 2.1: Initial experimental setting and generated ISWs parameters.

2.2 The laboratory model

To develop empirical relations with the initial setting parameters, the incident wave amplitude, wavelength and celerity are considered as characteristic values of each run. From image analysis, the vertical projection of the toe of the slope on the pycnocline is evaluated (i.e. point P' in Fig. 2.1c). The instant at which the approaching wave starts to induce a pycnocline displacement in P' defines the incident wave, whose features are amplitude, wavelength, and celerity. The main features of the incident wave are not affected yet by the presence of the sloping boundary. As soon as the solitary wave approaches the slope, the shoaling process starts, and the main wave features quickly change: the wave celerity decreases, and the wave modifies its original shape.

Empirical relations are developed in order to predict the ISWs main features depending on the geometrical parameters that define the initial experimental set up. The initial experimental setting is uniquely determined once the values of the following four parameters are fixed: the ambient fluid total depth H, the layers depth ratio in the ambient fluid region $r_0 = h_2/h_1$, the lock length x_0, and the displacement between the pycnoclines η_0. By using all the possible combinations of these four parameters, it was possible to design 24 experiments (Tab. 2.1) in order to obtain ISWs characterized by different amplitude A, characteristic wavelength λ and the wave celerity c.

The dimensionless wave amplitude A/h_2 and the dimensionless term $\eta_0 x_0/H\ h_2$ result related by empirical exponential functions (Fig. 2.4a), where the latter is the product between the dimensionless pycnocline displacement η_0/h_2, and the lock region aspect ratio x_0/H. The empirical exponential function reveals that the increase of the wave amplitude is correlated with the pycnocline displacement. Regardless from the lock aspect ratio (i.e. x_0/H), the wave amplitude is always lower than the pycnocline displacement η_0. Moreover, $\eta_0 x_0$ can be considered the generating volume enclosed in the lock before the gate removal. As the generating volume increases, the wave amplitude tends to reach asymptotically a limit value. For larger generating volumes, the resulting waves present an increase of the wavelength rather than of the amplitude. The wave amplitude also depends on the aspect ratio $\eta_0 x_0$ of the trapped light volume confined in the lock region (Fig. 2.4b). For a given pycnocline displacement η_0, the wave amplitude decreases when the lock length increases. The wavelength depends mainly on the generating volume. Fig. 2.4c shows the empirical relation between the two dimensionless volumes (i.e., the generating volume $\eta_0 x_0$) and the generated volume λA, which is equal to the volume of the generated wave. It results that the

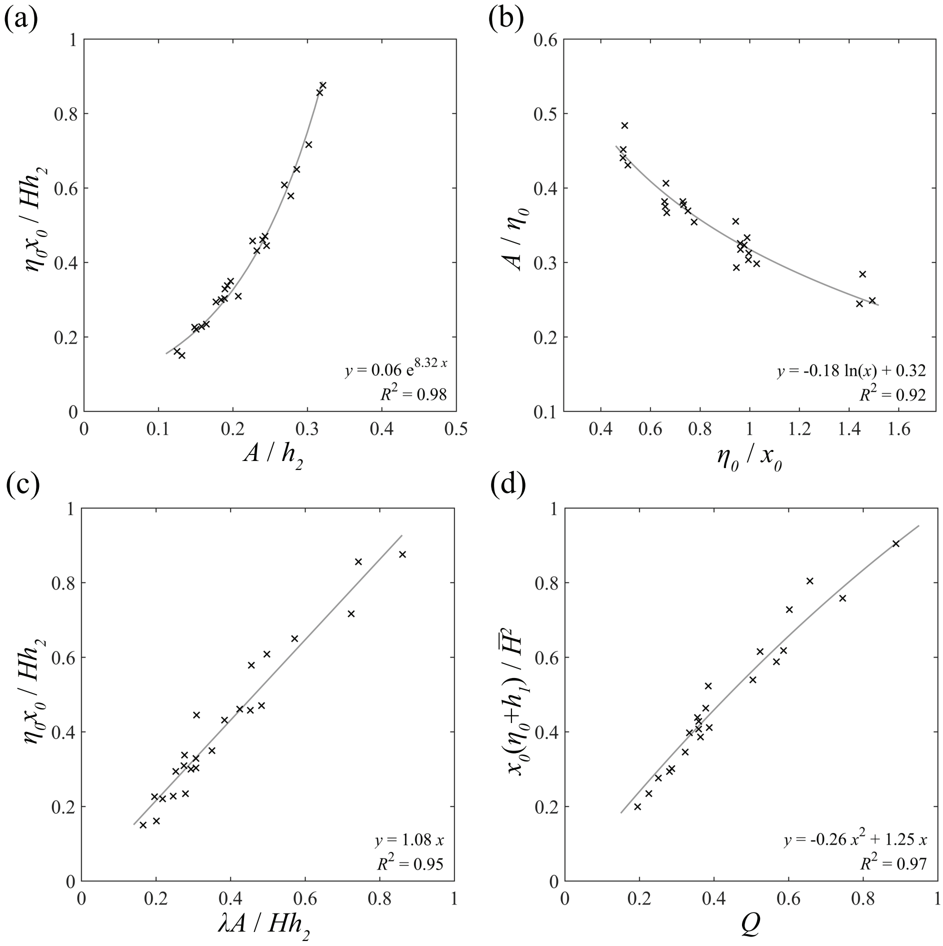

Figure 2.4: Empirical relations between input/output wave amplitude. a) dimensionless relation between the wave amplitude A and the generating volume $\eta_0 x_0$; b) relation between the aspect ratio η_0/x_0 and the dimensionless amplitude A/η_0. c) Relation between the dimensionless generated surface λA and the dimensionless generated surface $\eta_0 x_0$; d) Relation between the dimensionless specific flow rate and the parameters that define the initial setting of the experiments.

linear fit passes through the origin of the axes, then the generated volume of the wave is only a part of the initial volume confined in the lock, and the lost volume depends only on the generating volume. The gate removal causes an initial phase of rather violent fluid motion: a collapse mechanism occurs, characterized by an initial turbulent disturbance.

To obtain a further empirical relation, associated with the wave motion, the dimensionless specific flow rate Q is introduced, defined as:

$$Q = \left(\frac{A\lambda}{\overline{H}^2}\right)\left(\frac{c}{v_s}\right) \tag{2.4}$$

where:

$$\overline{H} = \frac{h_1 h_2}{h_1 + h_2} \tag{2.5}$$

$$v_s = \sqrt{g'\ \overline{H}} \tag{2.6}$$

The term g' is the reduced gravity defined as:

$$g' = g\ \frac{\rho_2 - \rho_1}{\rho_1} \tag{2.7}$$

The specific flow rate is normalized by using the harmonic mean of the upper and lower layer depths of the two-layer fluid (2.5), and the shallow water linear wave speed (2.6). In particular, the harmonic mean represents the characteristic depth of the ambient and it is introduced in order to evaluate the shallow water linear wave speed (c_s). In accordance with the KdV theory, the more the wave amplitude increases the more the ISWs celerity is larger than c_s [*Sutherland and Ivey*, 2013]. For this reason, the wave celerity is normalized by c_s, and both the wave amplitude and the wavelength are made dimensionless by using the harmonic mean of the upper and lower layer depths (2.5). Thus, the two factors in (2.7) represent the dimensionless wave surface and celerity. Fig. 2.4d shows the empirical relation between the parameters that define the initial experimental set up $x_0(\eta_0 + h_1)$, made dimensionless by using the depths harmonic mean, and the dimensionless specific flow rate Q.

For a given stratified ambient fluid, the specific flow rate increases as the volume of fresh water confined in the lock region increases: larger volume waves propagate faster, in accordance with the KdV theory. The analyzed relations explain more in detail the wave generation process, as obtained with the standard lock-release method. These equations will be used to set initial experimental parameters in order to generate desired waves in terms of amplitude and wavelength.

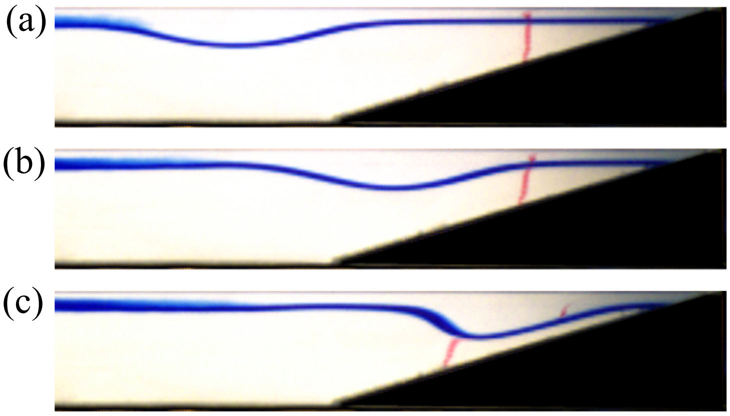

Figure 2.5: Consecutive snapshots during the shoaling process of a ISW over a sloping boundary. The fresh layer is partially dyed with methylene blue. Potassium permanganate vertical lines show the effect of the wave shoaling.

2.3 The breaking mechanisms

To identify the different breaking types, it is useful to directly observe in which process each generated wave gets involved during the shoaling. During this phase, for all the generated waves, two particular events occur:

- the steepening of the trailing edge of the wave;
- the downward motion of the volume confined between the leading edge of the wave and the sloping boundary.

The leading edge of the wave tends to become parallel to the slope and the fluid, confined in this region, flows down-channel with a strong acceleration. Potassium permanganate shows that the steepening of the trailing edge of the wave happens because the upper layer instantaneous horizontal velocities are lower along the verticals closer to the slope [*Aghsaee et al.*, 2010]. This process is similar to the steepening of the leading edge of the wave profile for SSWs shoaling [*Li and Raichlen*, 2002]. Fig. 2.5 shows three consecutive snapshots of a single solitary wave during the shoaling process. The fresh layer is partially dyed with methylene blue to better identify the pycnocline region and to observe directly the instabilities induced by the wave breaking, in the top layer.

Additional experiments were performed in order to qualitatively show the main processes induced by each breaker type, and the consequent development of different instabilities (Tab. 2.2). Figs. 2.6-2.9 show consecutive

Breaker type	Run	h_1 [cm]	h_2 [cm]	A [cm]	λ [cm]	c [cm/s]	s -
Plunging	44	1.2	10.0	4.3	25.5	10.9	0.298
Collapsing	37	3.3	15.0	4.3	40.1	10.8	0.363
Collapsing	42	4.8	19.2	2.3	42	10.2	0.292
Collapsing/Plunging	43	3.0	21.0	3.8	36.6	10.5	0.309
Surging	38	3.3	16.7	4.8	43.8	11.0	0.952

Table 2.2: Wave generated in order to analyze the different breaking mechanisms.

snapshots captured from a prospective point of view.

2.3.1 Qualitative description of the observed breaking mechanisms

In accordance with *Sutherland and Ivey* [2013], it was possible to recognized four breaking mechanisms: plunging breakers, collapsing breakers, plunging/collapsing breakers, and surging breakers. The development of a specific breaker type depends on the two processes described above. During the shoaling of the wave along the slope, the predominance of one of the two processes, or their simultaneous development, or their simultaneous absence affects the breaking mode.

For collapsing breakers, the downward motion of the confined fluid is dominant compared to the trailing edge steepening. During the shoaling, the dense water trapped between the wave and the slope quickly leaves its original position (Figs. 2.6a-d). At the same time, the trailing edge steepening slowly occurs without inducing any observable instability; the trapped dense fluid flows downward, in the adverse pressure gradient region; consequently, the down-slope flow quickly decreases its velocity after passing the wave trough, inducing the boundary-layer separation beneath the shoaling wave; a separation bubble forms close to the bottom (Fig. 2.6d). The turbulent structure quickly gives rise to an anticlockwise motion that causes a large amount of mixing in the breaking location (Figs. 2.6e-f).

Plunging breaking mechanism takes place when the overturning develops due to a dominant steepening of the trailing edge of the wave (Fig. 2.7). During the shoaling, a plunging breaker steepens the trailing edge that quickly overturns (Fig. 2.7a-c). At the same time, the dense fluid trapped between the wave and the sloping bottom leaves its position slowly and not completely. When the rear edge overturning occurs, a large amount of dense fluid sep-

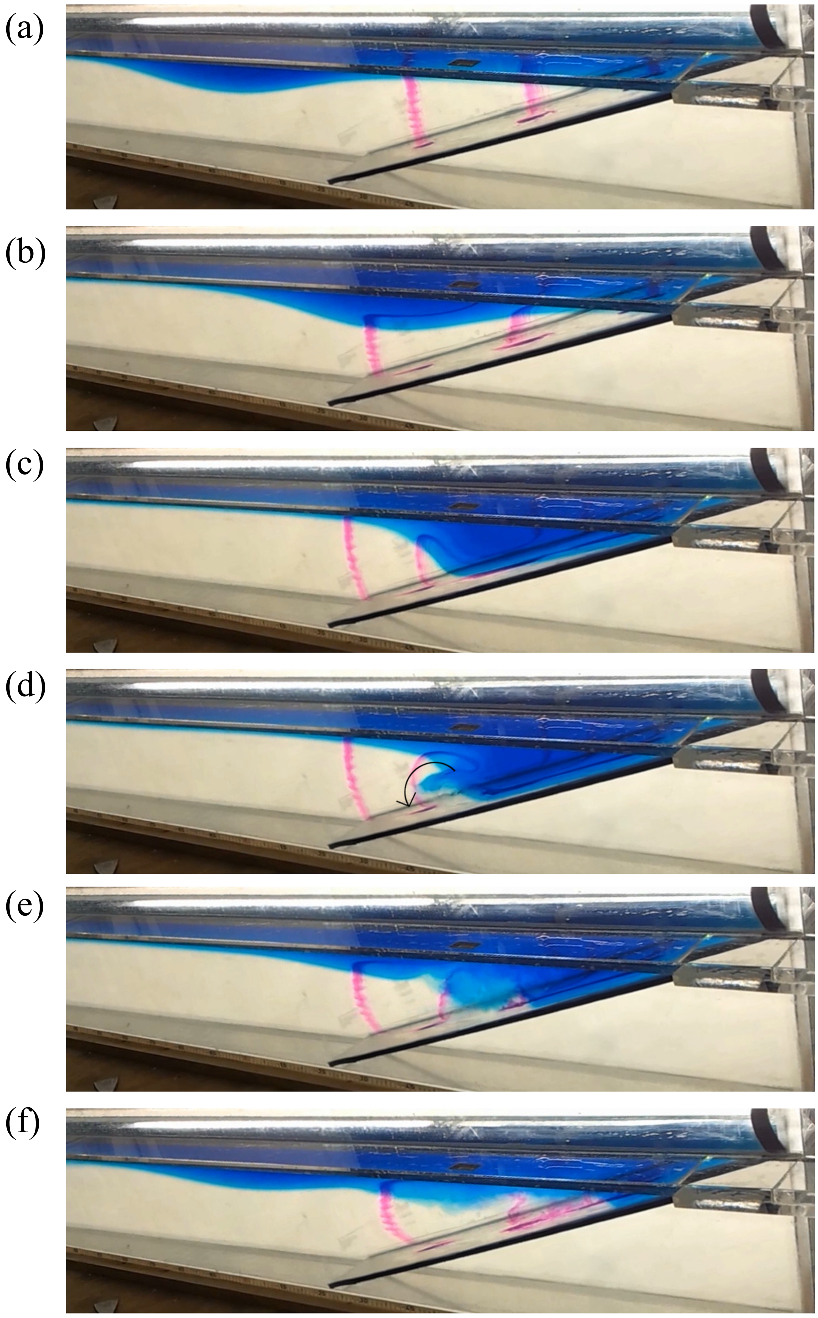

Figure 2.6: Collapsing breaker, Run 37. Consecutive snapshots during the shoaling and breaking processes. The wave reaches the slope (a); the confined volume beneath the leading edge flows out from this position (b,c); an anti-clockwise vortex forms near the bottom (d); the vortex losing its energy moves onshore (e); the wave is partially reflected (f).

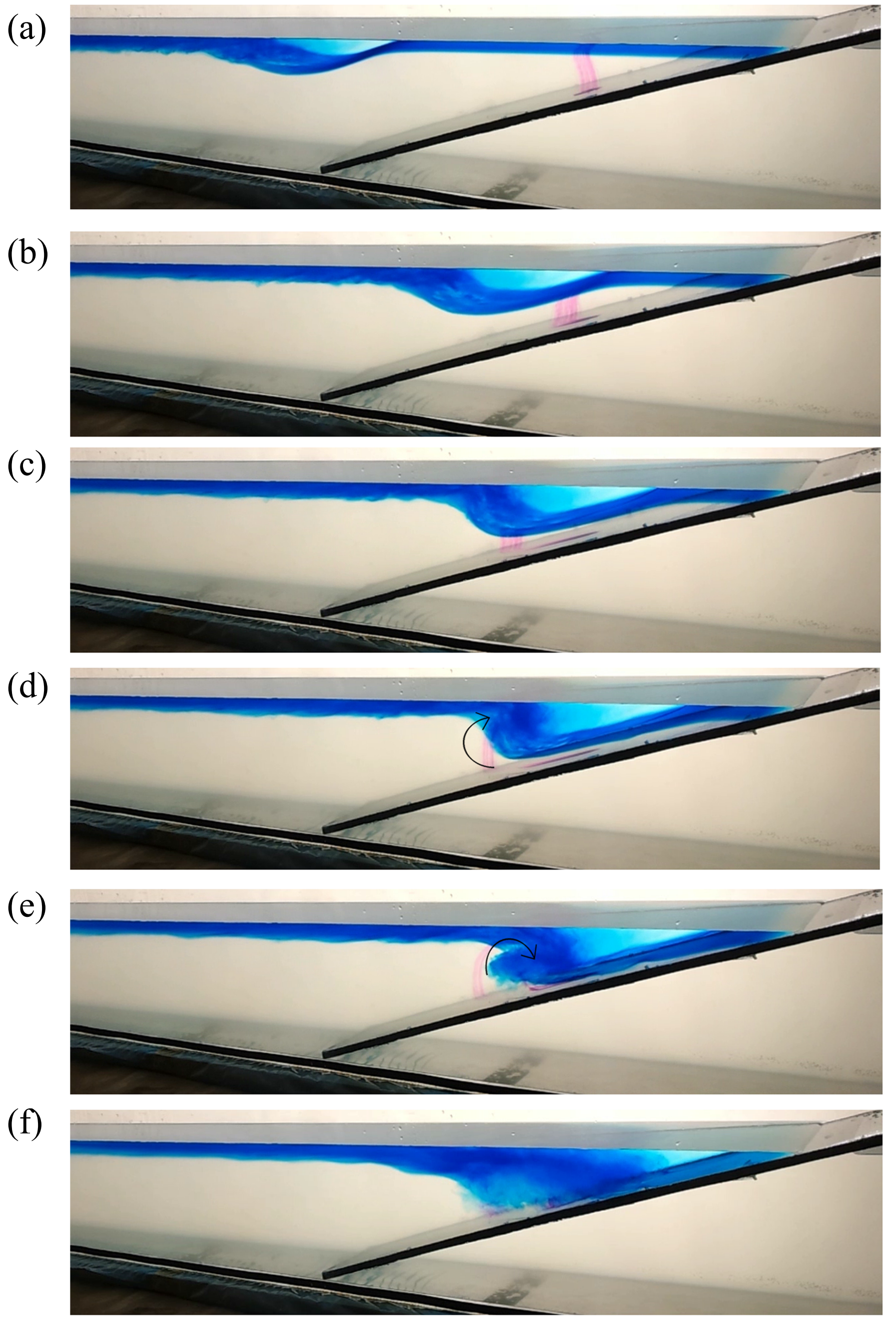

Figure 2.7: Plunging breaker, Run 44. Consecutive snapshots during the shoaling and breaking processes. The wave reaches the slope (a); the steepening of the trailing edge occurs (b,c); a clockwise vortex forms (d) and reaches the sloping bottom onshore, generating mixing (e,f).

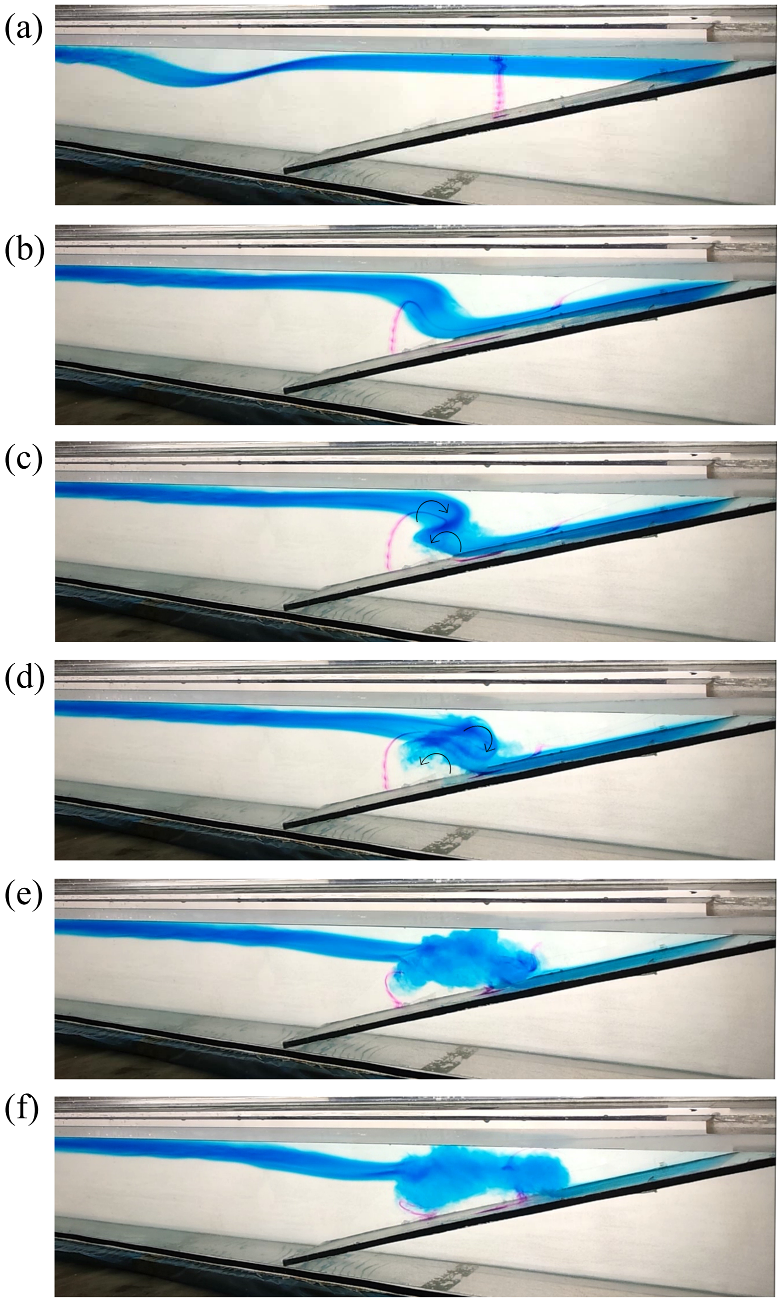

Figure 2.8: Collapsing-Plunging breaker, Run 43. Consecutive snapshots during the shoaling and breaking processes. The wave reaches the slope (a); the steepening of the trailing edge and the downward motion of the confined volume occur (b); a clockwise vortex near the surface and a separation bubble close to the bottom form (c,d); a large amount of mixing occur (e,f).

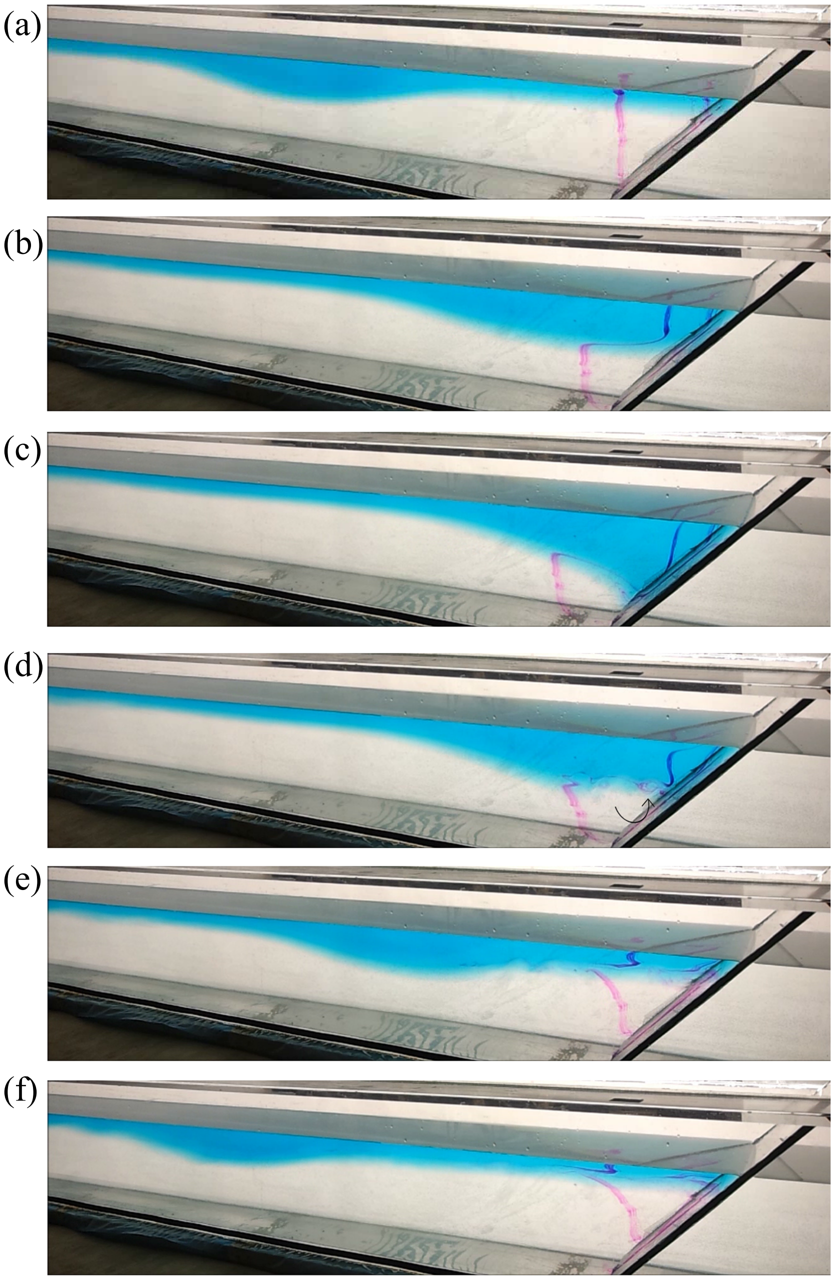

Figure 2.9: Surging breaker, Run 38. Consecutive snapshots during the shoaling and breaking processes. The wave reaches the slope (a); the steepening of the trailing edge and the downward motion of the confined volume occur without generating instabilities (b,c); a gravity current forms above the slope (d); most part of the wave is reflected (e,f).

arates the wave from the sloping boundary yet (Fig. 2.7d). During the plunging process, mixing is confined within the body of the water column at the breaking location. The clockwise vortex (Fig. 2.7e) is initially detached from the sloping boundary, then it propagates onshore, toward the sloping bottom, gradually losing its energy (Fig. 2.7f).

An intermediate breaking mechanism, i.e., collapsing/plunging breakers (Figs. 2.8a-b), is observed in the breaking location, where the contemporary formation of a clockwise vortex within the body of the fluid and a separation bubble close to the bottom (Figs. 2.8c-d). This causes a large amount of mixing, because of the double motion at the breaking location. (Figs. 2.8e-f).

Finally, another kind of breaking can be observed. In this case, neither the steepening of the trailing edge, nor the downward motion of the water volume confined below the right tail, cause the development of any kind of instability (Figs. 2.9a-c). Figs. 2.9d-f show that when the trough of the wave reaches the sloping boundary a second kind of instabilities occur, composed by a gravity current flowing up the slope [*Lombardi et al.*, 2015; *Ottolenghi et al.*, 2014]. This kind of breaking refers to the surging breakers.

A quantitative analysis of the shoaling phase behind the breaking processes follows in the next section. This allows defining the parameters that properly link breaker types with their shoaling conditions.

2.3.2 Characterization of the shoaling processes

The occurrence of different breaking mechanisms depends directly on the wave evolution over the slope region. I therefore parametrized the two main processes that characterize the shoaling phase: the steepening of the trailing edge of the wave (i.e., rear front of the ISW) and the downward (i.e., upstream) motion of the volume confined between the leading edge of the wave and the sloping boundary (Fig. 2.1d). I evaluated the instantaneous trailing edge steepening by the decrease of the angle α, defined between the line perpendicular to the sloping boundary and the rear edge slope (Fig. 2.1d). The latter is calculated as the derivative of the ISW profile at the midpoint (M) between the wave through and the final point of the trailing edge (Fig. 2.1d). To characterize the downward motion of the dense fluid confined between the wave and the sloping boundary, I investigated the evolution of the volume V_t, identified by the trapped dense fluid between the wave and the slope. This volume is instantaneously evaluated starting from the segment between the wave trough (T) and its vertical projection on the bottom (T').

For four runs, characterized by different breaking mechanisms, I analyzed the evolution of the two dimensionless parameters α/α_0 and V_t/V_{t0}. For those runs, I estimated the total time of the shoaling process (t_i), which starts when the wave begins to modify its main features because of the presence of the slope. The values of α_0 and V_{t0} refer to the initial shoaling time. Wave shoaling lasts until any discontinuity of the pycnocline (i.e., the ISW profile) do not show up. I obtained the trend of α/α_0 (Fig. 2.10a) and V_t/V_{t0} (Fig. 2.10b) for the four breaker types. Fig. 2.11 shows consecutive snapshots of the shoaling and breaking phases for the four cases. After the shoaling phase (i.e., for $t/t_i > 1$) wave breaking occurs.

The plunging breaker presents a large initial decrease of α/α_0, compared to the other cases. This is in accordance with the consequent breaker type, characterized by the overturning of the rear edge of the wave. This event begins before the leading edge is completely reclined on the sloping boundary. During the overturning ($t/t_i = 1 \div 1.2$ in Fig.2.11a), the upstream displacement of the vertical tracer shows that the downward motion of the denser, bottom fluid below the leading edge, is still occurring.

For the collapsing breaker, the ratio α/α_0 remains initially unvaried because wave geometry does not change (Fig. 2.10a). The wavelength of the collapsing wave is indeed larger and the resulting horizontal velocity gradient assumes lower values when compared to the plunging case [*Aghsaee et al.*, 2010]. During the shoaling of a collapsing case, the decrease of the upper layer horizontal velocities and, consequently, the trailing edge steepening are smaller than those of the plunging case. Moreover, about at the half of the shoaling phase, the decrease of the trapped volume is larger for the plunging breaker than for the collapsing one. During the final stages of the shoaling, these occurrences undergo a change: the trailing edge of the plunging breaker quickly steepens, and, at the same time, the trapped volume continues to decrease more slowly. The edge overturning takes place before the confined volume completely leaves its original position (Fig. 2.11a). For the collapsing breaker, the rear edge steepening occurs during the final phase of the shoaling process (Fig.2.10a). The downward motion beneath the shoaling wave is the dominant process, which develops with a constant speed, until all the trapped dense fluid is completely expelled (Fig.2.10b). While the trapped volume is almost linearly decreasing, the surface from which it flows, decreases (Fig. 2.11b). For this reason, during the final phase of the shoaling process, large values of the downward velocities are expected. This flow evolves in the direction of the adverse pressure gradient. Thus, the boundary layer separation is expected to occur, and to be the cause of

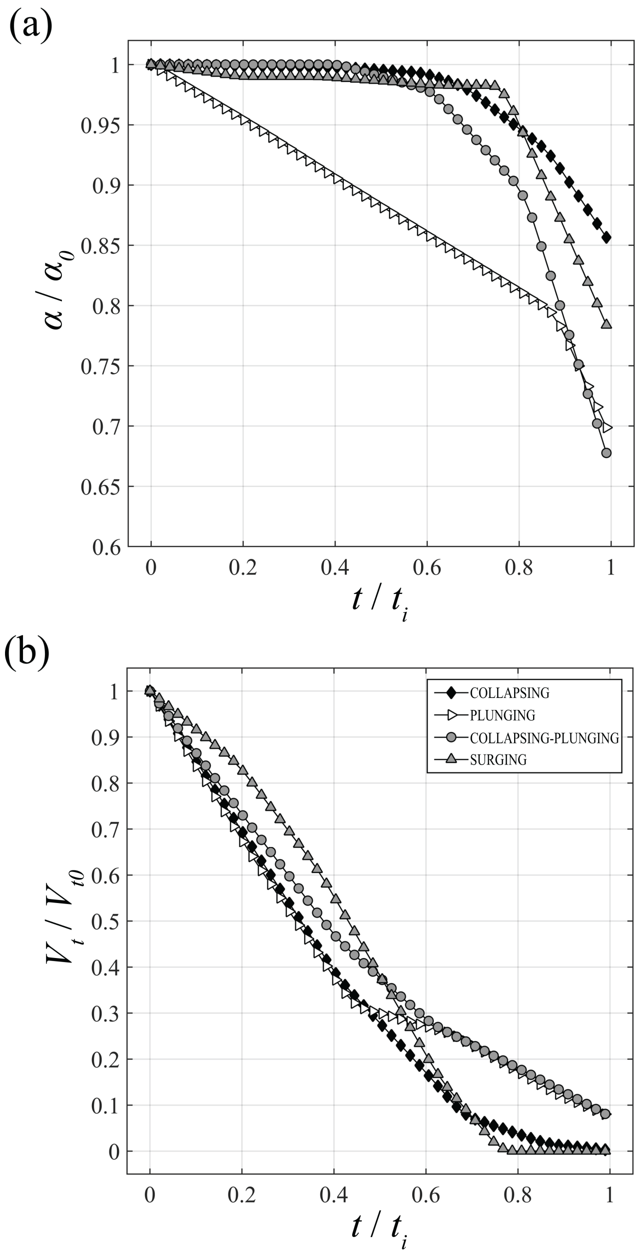

Figure 2.10: Parametrization of the shoaling phase for four breaking mechanisms: plunging breaker (Run 44), collapsing breaker (Run 42), collapsing-plunging breaker (Run 43), surging breaker (Run 38). Decrease of the dimensionless trailing edge slopes α/α_0 (a) and trapped dense volume V_t/V_{t0} (b) during the shoaling. For each experiment, time is normalized by the shoaling time t_i.

the instability generated close to the bottom (for $t/t_i > 1$).

Collapsing-plunging breaking is in the middle between the two previous cases (Fig. 2.10). The dimensionless ratio α/α_0 remains initially roughly unvaried, as for the collapsing breaker. At $t/t_i \simeq 0.4$ it begins to decrease very quickly reaching the same trend of the plunging breaker at the end of the shoaling. At the same time, the decrease of the trapped volume presents a slightly marked deviation point at $t/t_i \simeq 0.4$, after which it becomes slower, as for the plunging breaker. Finally, for surging breaker the main mechanism seems to be the decrease of V_t/V_{t0}: a boundary layer separation induced by the downward motion would be expected. This event does not take place, probably because the larger amount of the confined volume leaves its original position during the initial shoaling phase, when the surface defined by TT' (Fig. 2.1d) is not small enough to induce strong downward velocities at the bottom.

2.3.3 The breaking domains

The wave shoaling analysis shows how the occurrence of a particular kind of breaking mechanisms depends on the different geometric characteristics of the incident waves compared to the sloping boundary.

For this reason, in agreement with the works of *Aghsaee et al.* [2010] and *Sutherland and Ivey* [2013], two parameters are introduced: the topographic slope s and the wave slope S_w, defined as:

$$s = \tan(\theta) \tag{2.8}$$

$$S_w = \frac{A}{\lambda} \tag{2.9}$$

where θ is the angle between the slope and the horizontal. For all experiments, the relation between these two parameters is plotted (Fig. 2.13). Results show that the different breaker mechanisms are located in three different regions of the domain S_w, s, which are distinguished by means of the (internal) Iribarren number [*Bridges*, 2008]:

$$Ir = \frac{s}{{S_w}^{0.5}} \tag{2.10}$$

The Iribarren number is a dimensionless parameter universally applied to model surface gravity waves breaker types on beaches [*Dean and Dalrymple*, 1991]. By using the same geometric parameters, many authors defined ISWs breaking mechanisms [*Boegman et al.*, 2005; *Aghsaee et al.*, 2010; *Sutherland*

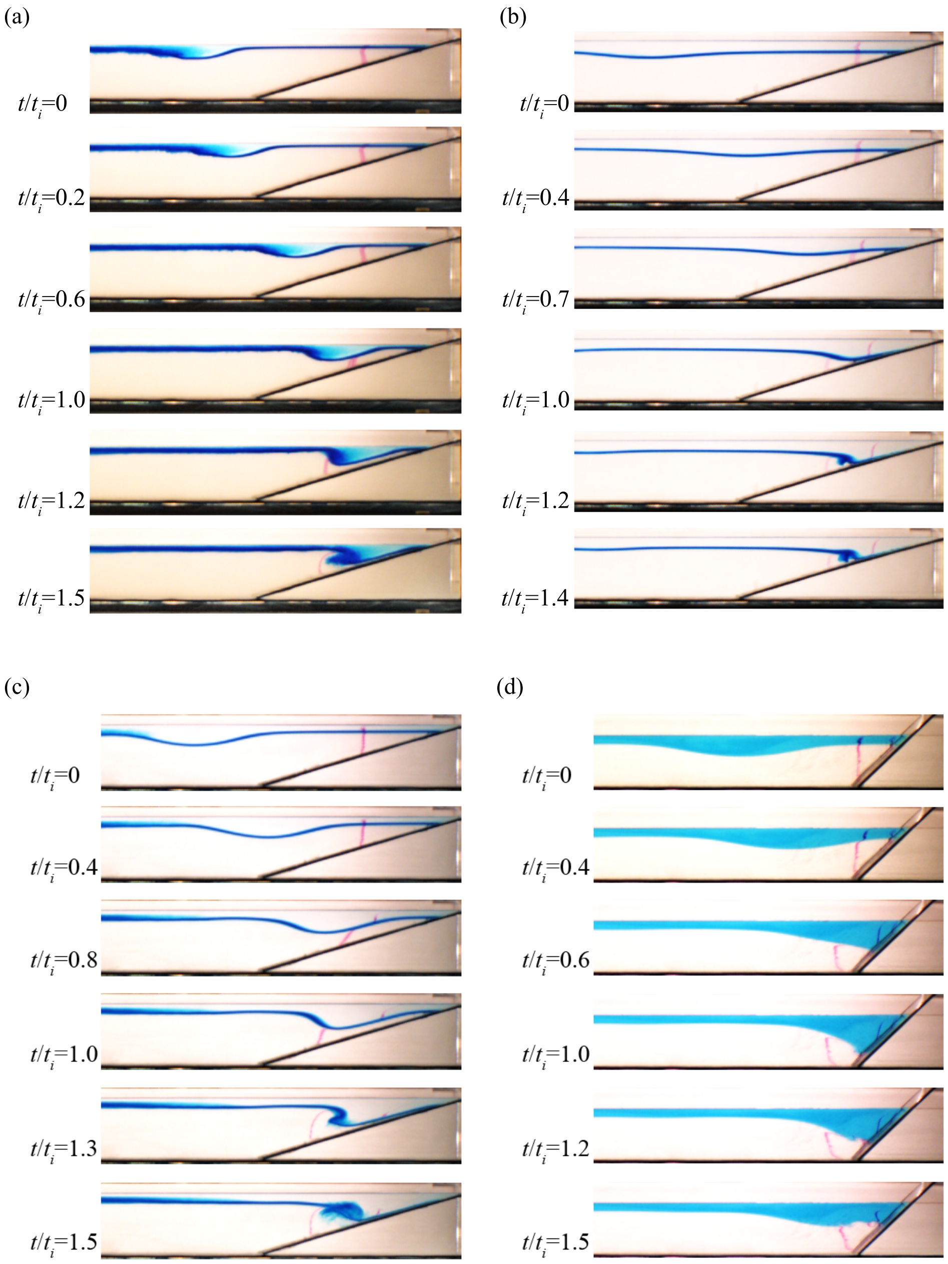

Figure 2.11: Consecutive snapshots captured during the shoaling and the breaking of Run 44: plunging breaker (a), Run 42: collapsing breaker (b), Run 43: plunging/collapsing breaker (c) and Run 38: surging breaker (d). For Run 38 the methylene is used to dye all the lighter volume. The timescale is made dimensionless by the time of the shoaling phase t_i. The mixed region inside the plunging wave body is caused by the generation mechanism.

and Ivey, 2013]. Nevertheless, a part from some similarities, the breaking evolution of surface waves and internal waves appear rather different. Fig. 2.12 shows a schematic comparison between the surface waves breaker types and the ISWs breaking mechanisms observed in our experiments. The steepening of the wave crest characterizes spilling and plunging surface waves, which usually occur for waves interacting with relative gentle slopes.

By increasing the slope, wave steepens and a turbulent whitewater spills down the face of the wave while, for steeper slopes, the crest curls over and drops onto the trough of the wave. For the observed ISW plunging breakers present the steepening of the trailing edge, such that the breaking evolves with its consequent overturning.

For even steeper slopes, both for internal and for surface waves, the collapsing mechanism occur. This results in an instability, evolving close to the bottom.

For very steep sloping boundaries, surging breakers are observed. For surface waves, a rapid motion of the base of the wave and the disappearance of the wave crest occur. The wave almost does not break and a little whitewater forms. For ISWs surging breakers the instabilities result in a gravity current flowing upward the incline, after the wave trough touches the sloping boundary. It is possible to conclude that the main similarities between surface and internal breaking waves are the edge steepening for plunging breakers and the location of the breaking for collapsing and surging breakers.

In our experiments, collapsing breakers are observed for values of ${S_w}^{0.5} < 1.5s$ and in particular for $Ir = 1 \div 1.5$. For gentler slopes, and/or for larger wave slope, plunging breakers develop (Fig. 2.12). They are observed for ${S_w}^{0.5} > s$, i.e. $Ir < 1$. The collapsing-plunging case occurs for ${S_w}^{0.5} \simeq s$ since, under these conditions, the two main breaking processes simultaneously are observed.

Runs 49-54 (Fig. 2.13) are performed in order to investigate the breaking effect of plunging breakers. For these runs, the density field is obtained by image analysis. I obtained the domain of the different breaking regimes by using a definition of characteristic wavelength based on a theoretical approach. By using the empirical relation developed in Section 2.2 it is possible to set the proper experimental setting that generates the desired wave and, in particular, to choose the appropriate values of the sloping boundary in order to induce, for each designed wave, a particular breaking mechanism.

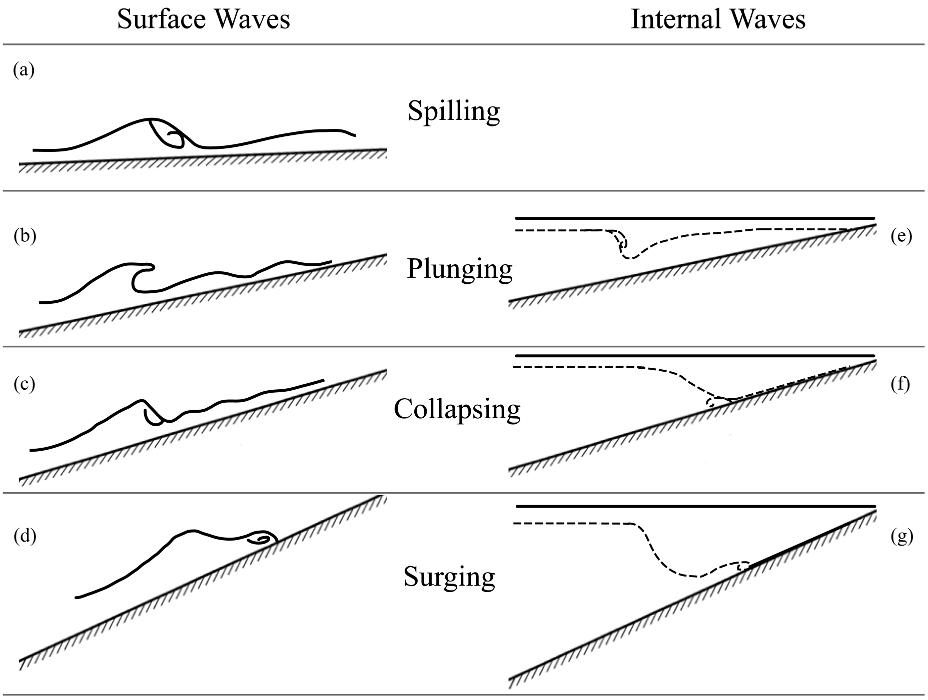

Figure 2.12: Schematization of the different surface (a-d) and internal (e-g) waves breaker types. The scheme considers a single wave interacting with an increasingly inclined sloping boundary. The dashed lines define the pycnocline position. The solid lines over the sloping boundaries indicate the free surfaces.

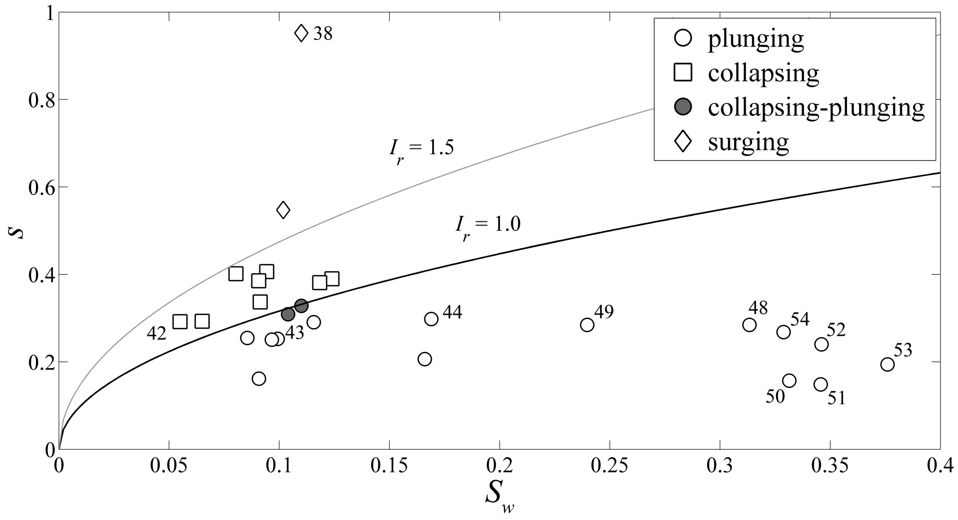

Figure 2.13: Domains of the different breaking regimes identified by the Iribarren number. Runs 38, 42- 44 were performed to analyze the shoaling process. Runs 49-54 were performed to evaluate the effect of the breaking (Sec. 2.4.

2.4 Plunging breakers: the case of the Messina Strait

The Messina Strait separates the Sicily island from the Italian Peninsula and represents the connection between the Tyrrhenian Sea in the north and the Ionian Sea in the south. The center of the Strait presents a shallow sill: here the maximum water depth is about 80 m. For this reason the center of the Strait represents a barrier to the water exchange between the two Seas. The phase opposition of the semidiurnal tides, in the Thyrrenian and Ionian Seas, generates large gradients of tidal displacements [*Brandt et al.*, 1999]. The interaction between these gradients and the topography features of the strait gives rise to strong tidal currents [*Alpers et al.*, 1996]. During northward (southward) tidal flow the Ionian (Tyrrhenian) waters, overflowing the sill, spills into the Tyrrhenian (Ionian) Sea. Because of the different stratification that characterizes the two Seas [*Vercelli*, 1925], nonlinear internal solitary waves of depression form and propagate from the Strait towards the north (south), in the Tyrrhenian (Ionian) Sea [*Nicolò and Salusti*, 1991; *Sapia and Salusti*, 1987]. Fig. 2.14 shows the topography of the north part of the Strait where the presence of a second sill forms a bottom with a slope $s_M = 0.075$ [*Marullo and Santoleri*, 1986]. *Alpers et al.* [2008] show the density and velocity fields induced by a nonlinear internal wave packet composed by three solitary waves of depression propagating towards the north of the Strait. The main wave has an amplitude $A_M = 100$ m and a characteristic wavelength $\lambda_M = 800$ m, approximately. The evaluation of the wave surface allows defining the wave slope value: $S_w = 0,1$. The corresponding Iribarren number is 0.24, a typical value of the plunging breakers.

To focus on the characteristic of the plunging breakers, and thus to investigate the potential effects of this kind of breaking in the north of Messina Strait, seven ad hoc experiments are performed (Tab. 2.3).

Although our experiments aim at the sole understanding of the breaking mechanisms involved in the real field, rather than scaling the real field conditions, our set-up is based on the internal solitary waves observed in the Strait of Messina and the topography that constraints their evolution northward (Fig. 2.14). A real-field reduced gravity g' and the Iribarren number Ir, as obtained from *Brandt et al.* [1999], are considered.

For each run, a constant value of 30 kg/m^3 is used as density difference between the two layers in the ambient fluid region. Then the reduced gravity is similar to the values measured in the real field [*Marullo and Santoleri*, 1986]. The Iribarren number is always less than one, thus the breaker type falls within the plunging breakers domain.

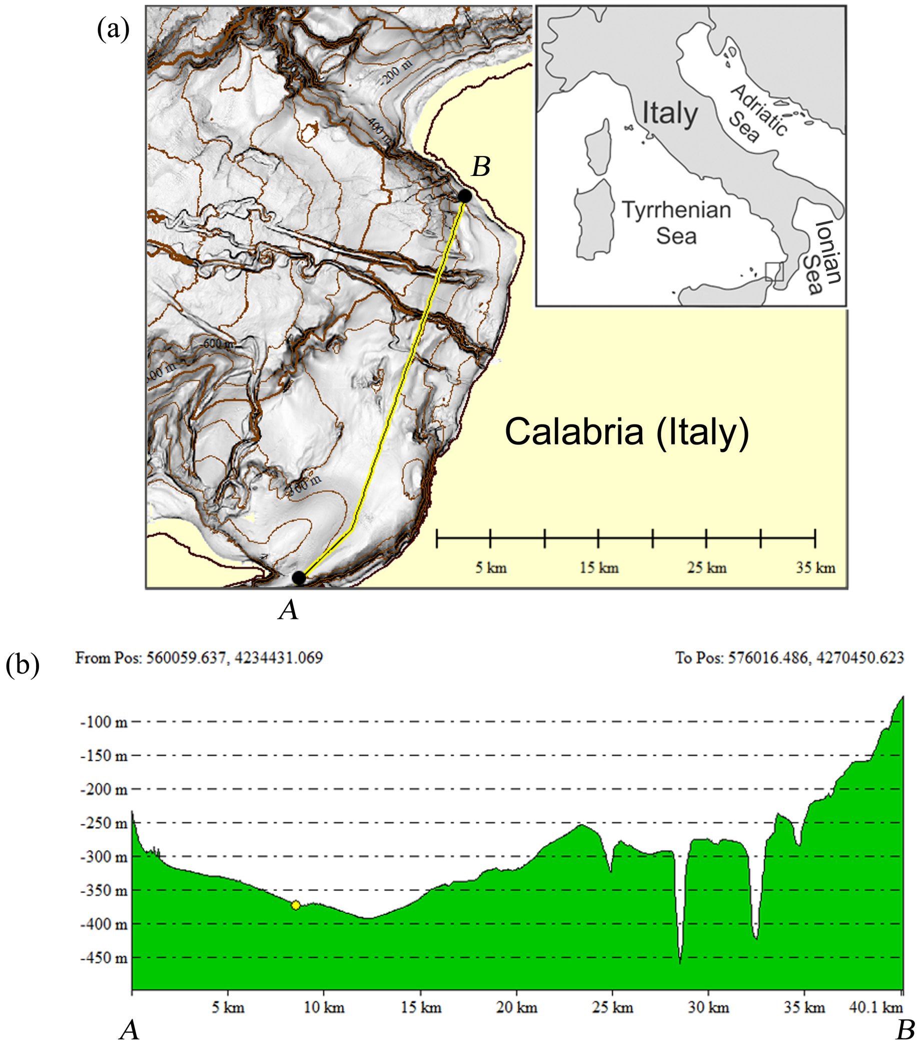

Figure 2.14: Bathymetry of the Strait of Messina along the cross northward section between the points A and B where ISWs are observed (a). Profile of the bathymetry along the considered cross section (b).

Run	A [cm]	λ [cm]	c [cm/s]	S_w	s	Ir
48	3.9	12.4	11.6	0.31	0.284	0.506
49	1.8	7.3	8.6	0.25	0.284	0.572
50	2.7	8.8	8.1	0.31	0.156	0.282
51	2.6	7.6	8.7	0.34	0.147	0.251
52	2.5	7.3	9.9	0.35	0.238	0.405
53	2.6	6.9	9.6	0.38	0.194	0.316
54	2.6	7.9	9.6	0.33	0.268	0.467

Table 2.3: Wave characteristics and slope values for the experiments performed to evaluate the effect of plunging breakers.

The analysis of the density profiles allows evaluating the effect of the breaking. As direct consequence of the breaking event, the pycnocline increases its thickness. To specifically evaluate this phenomenon, and to have a bulk evaluation of the breaking effects, the region overlying the slope has been chosen as the domain of interest. The domain is bounded by the free surface and the sloping boundary, while its left hand-side is limited by the vertical passing through the slope's toe. The space-averaged dimensionless density profiles along the domain is considered in order to analyze their change during each time interval, before and after the breaking process. For each time step, the evaluation of the density field by image analysis, allowed to obtain all the density profiles along the water depth; their horizontal average is computed, in order to estimate the instantaneous space-averaged density profile.

$$\rho_d = \frac{\rho(x,y) - \rho_1}{\rho_2 - \rho_1} \tag{2.11}$$

$$h_d = \frac{y}{H} \tag{2.12}$$

The dimensionless densities (ranging between 0 and 1) are defined in Eq. 2.11, where $\rho(x, y)$ is the density at each point of the domain, defined by the coordinates x and y, and $\rho_{1,2}$ are the densities values of the two layers in the ambient fluid region, before the gate removal. Moreover, Eq. 2.12 defines the dimensionless water depths h_d.

The comparison between the initial and final space-averaged dimensionless density profile for each run, allowed to quantify the effect of the breaking in terms of increase of the pycnocline thickness. The initial condition refers to the initial time interval immediately before the gate removal. The final

Run	IP_t [cm]	FP_t [cm]	H [cm]	ΔP [cm]	ΔP_t	$\Delta P_t/S_w$	S_r [cm^2]
48	1.11	3.32	21.0	2.21	0.105	0.335	15.1
49	1.17	1.46	21.0	0.29	0.014	0.056	6.5
50	1.08	1.90	13.0	0.81	0.063	0.206	4.5
51	1.18	1.77	13.0	0.59	0.045	0.133	4.9
52	0.56	1.70	13.0	1.13	0.088	0.253	5.4
53	0.58	1.73	13.0	1.16	0.088	0.235	5.4
54	0.29	1.44	13.0	1.16	0.089	0.271	6.1

Table 2.4: Values of the initial (IP_t) and the final (FP_t) pycnocline thickness, the total water depth (H), the increase of the pycnocline thickness (ΔP_t) and the ratio $\Delta P_t/S_w$. S_r identify the surface of the reflected wave.

density profile is defined when the fluid is at rest in stable equilibrium after the breaking event. Therefore, for each run, constant values of the pycnocline thickness characterize the final condition. During these experiments, no secondary waves formed, and the fluid reaches a stable at rest condition before the reflected wave comes back in the domain of interest. Fig. 2.15 shows the change in the pycnocline thickness at two different times: before the gate removal (Fig. 2.15a) and after the breaking event (Fig. 2.15c).

The pycnocline thickness is obtained by estimating the local maximum and local minimum of the derivative of each density profile. The breaking event induces mixing that causes the increase of the pycnocline thickness. By comparing the initial and final conditions for each run, the increase of the pycnocline thickness ΔP is obtained. For all the performed experiments an increase of the pycnoclines thickness occurs.

Tab. 2.4 shows the parameters used to analyze the mixing effects. In particular, the ratio between the increase of the dimensionless pycnocline thickness $\Delta P_t = \Delta P/H$ and the wave slope S_w is evaluated. The relation between the change in the pycnocline thickness and the Iribarren number is investigated (Fig. 2.16a). This relation shows that the overturning of the trailing edge for two different plunging breakers, with equal ratio of amplitude and wavelength, cannot generate the same breaking effects. The change in topographic slope affects the breaking, inducing different increases of the pycnocline thickness.

The ratio between the dimensionless increase of the pycnocline thickness and wave slope increases with the Iribarren number. However, this increasing trend seems to collapse for $Ir > 0.55$, suggesting a non-efficient overturning, in terms of mixing, for values of Ir that tend to the collapsing phase (i.e.,

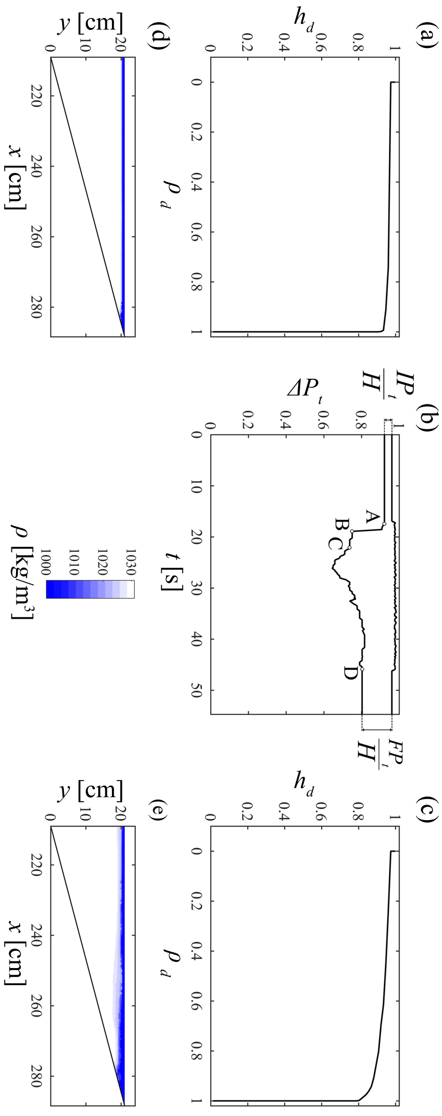

Figure 2.15: Averaged dimensionless density profiles and density fields for Run 48. Averaged dimensionless density profiles associated to: a) the initial condition ($t = 0$ s), and c) after the breaking event ($t = 54.7$ s). For each density profile, the density field is shown: d) the initial condition ($t = 0$ s), and e) after the breaking event ($t = 54.7$ s). Trend of the dimensionless pycnocline thickness during the experiment (b). Time intervals between points A and B define the entrance of the ISW into the domain. Time intervals between points B and C identify the shoaling phase. Time intervals before point A and after point D define the initial and final equilibrium states respectively.

$Ir = 1$). Low values of Ir well describe the Messina Strait case. The linear behavior that occurs in this region allows us to estimate the breaking effects on the pycnocline thickness in the real-field, where ΔP_t is expected to range in between 0.05 and 0.1 [*Marullo and Santoleri*, 1986].

ISWs propagating towards the north of the Messina Strait, are expected to break coherently with this nonlinear behavior. Then for plunging breakers, once the total water depth and the topographic slope are defined, a particular value of wave slope S_w that maximizes the increase of the pycnocline thickness exists. On the other hand, for a given value of total water depth, and for a well-defined wave in terms of amplitude and wavelength, a particular value of the topographic slope maximizes the breaking effects. By increasing this value, the breaking event induces a wave reflection process and the mixing effects in the pycnocline region tend to fade.

To investigate the horizontal distribution of the pycnocline thickness, the domain of interest is divided in four regions of equal length above the sloping boundary (Fig. 2.17). For each zone the space-averaged dimensionless density profiles are evaluated.

For all the performed experiments, and for each zone, the increases of the pycnocline ΔP thickness are plotted (Fig. 2.16b). The zone 0 refers to the ambient fluid region preceding the sloping boundary in which the increase of the pycnocline is nil or negligible. By approaching the right end of the tank, the effect of the breaking is noticeable.

All this suggests that the horizontal distribution of mixing also depends on the breaking location. For the performed experiments, indeed, the breaking location is always one zone upstream the one where the maximum increase of pycnocline thickness occurs (Fig. 2.17).

Since a small amount of the incident wave is reflected, the horizontal trend of the increase of the pycnocline thickness can be also affected by the action of the reflected wave that moves the mixed region offshore. Run 48, indeed, shows the largest reflected wave in terms of wave surface (Tab. 2.4). Thus, it is possible to conclude that both breaking location and reflected wave features may affect the horizontal distribution of the breaking effects.

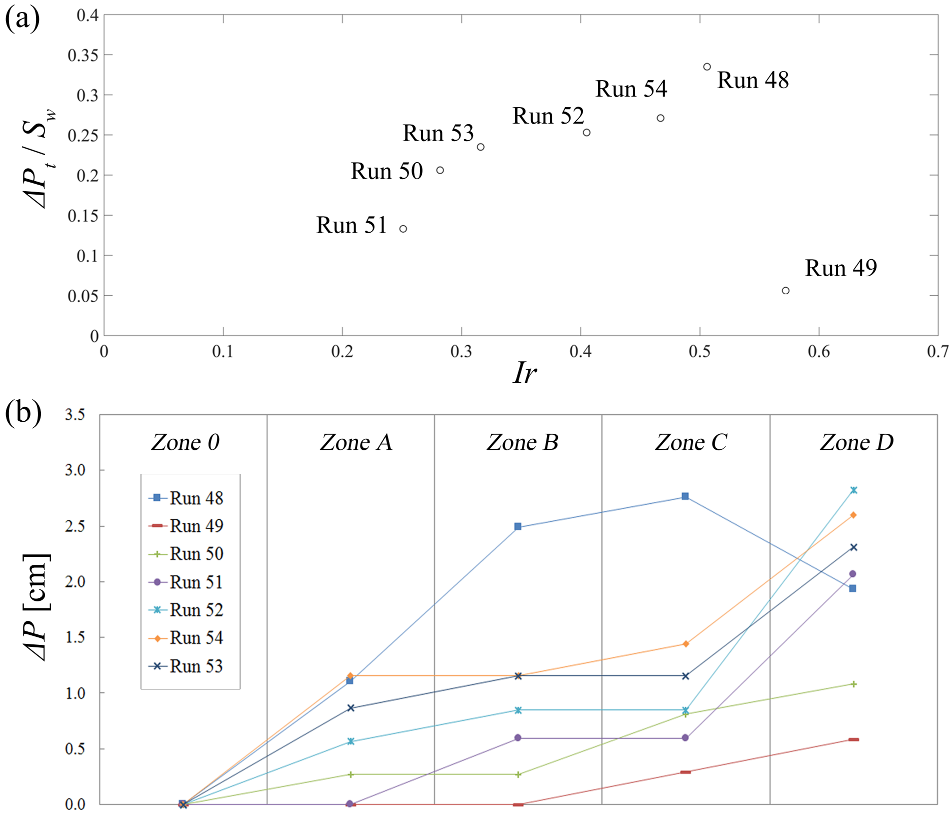

Figure 2.16: Relation between the ratio $\Delta P_t/S_w$ and Ir (a); horizontal trend of the increase of the pycnocline thickness ΔP (b). ISWs broke always one zone upstream with respect to the one where the maximum of pycnocline thickness increase occurs.

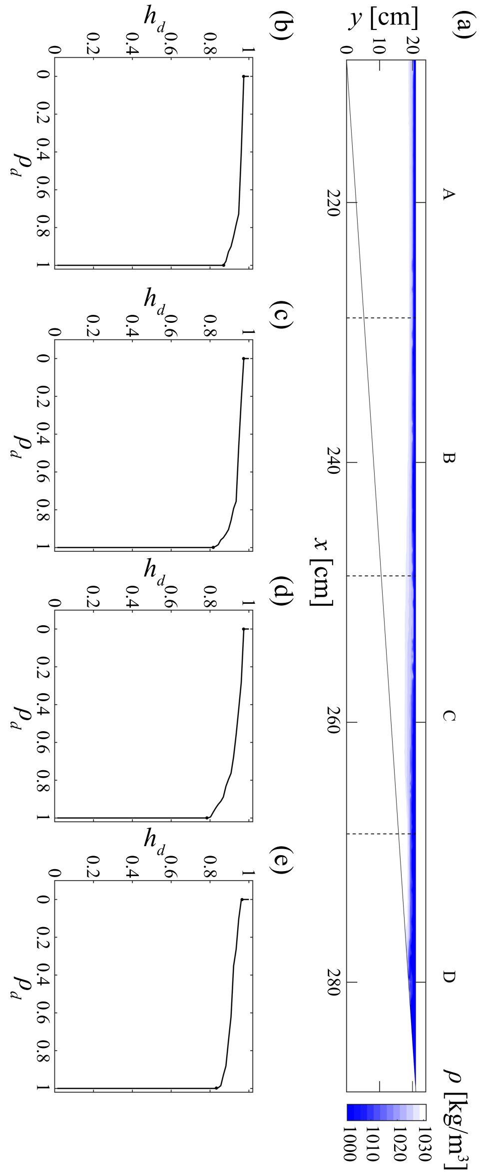

Figure 2.17: Run 48: density field (a) and averaged dimensionless density profiles of the four zones above the slope. Dashed lines separate the different zones, indicated by A-D. Space-averaged dimensionless density profiles of the zone A (b); B (c); C (d); D (e). Dots define the pycnocline limits for each zone.

Chapter 3

Numerical simulations of breaking ISWs

Each ISW breaking mechanism is characterized by peculiar dynamics and, consequently, different effects in terms of mixing, entrainment and shear stress at the bottom. During the wave shoaling, both the steepening of the rear edge of the wave, and the downward motion of the denser fluid confined between the leading edge and the incline occur.

Depending on ISWs geometric features and slope values, the ISWs shoaling over a sloping boundary differently develop [*La Forgia et al.*, 2017]. For plunging breakers, the steepening of the trailing edge evolves in a quick overturning in the onshore direction, entraining denser water and causing mixing [*Sutherland and Ivey*, 2013]. For the breaker type know as collapsing, the rear edge steepening slowly occurs and it does not involve any observable instability. At the same time, the dense water confined between the wave and the slope leaves its original position with a fast downward motion in the adverse pressure gradient region. The consequent decrease of down-slope velocities induces the boundary layer separation: a turbulent structure composed by a separated bolus forms and quickly dissipate with an anticlockwise motion. [*Aghsaee et al.*, 2010]. The collapsing process then goes on: part the incident wave is reflected and a gravity current composed by the denser fluid flows up the slope, until the hydrostatic conditions are re-established.

The surging breaker type characterizes those ISWs that during the shoaling do not present any observable turbulent instability until the wave trough reaches the sloping bottom. The wave is not completely reflected because a gravity current composed by the denser fluid flows up the slope inducing mixing [*Sutherland and Ivey*, 2013; *Ottolenghi et al.*, 2016a, 2017a].

As one would expect, depending on the different dynamics characterizing plunging, collapsing and surging breakers, distinct effects occur in terms of entrainment, mixing and shear stress at the bottom. This Chapter deals with the effects of the three different breaking mechanism. A Large Eddy Simulation (LES) numerical model is used in order to examine ISWs shoaling and breaking effects, in terms of mixing and entrainment. Being each breaking mechanism characterized by different dynamics, our goal is to distinguish different ISWs braking types depending on the effects they induce.

The following Chapter is organized as follows: Section 3.1 introduces the experimental procedure adopted to generate ISWs and to produce a well-defined breaking mechanism. Section 3.2 describes the numerical model adopted to simulate the ISWs generated in the small-scale apparatus, and its validation. Section 3.5 illustrates the entrainment process. In Section 3.4 ISWs energetics are evaluated in order to estimate the irreversible mixing. Section 3.5 analyze the spatial and temporal distributions of the bed shear stress on the incline after the ISW starts interacting with it. It also provides an estimate of the potential of the ISW to induce sediment entrainment in the case of a loose-bed sloped surface. Section 3.6 discusses the significance of the main results and provides some conclusions.

3.1 Internal solitary wave generation and related experiments

Laboratory experiments are performed at the Hydraulics Laboratory of the University '*Roma Tre*', in a 3.0 m long, 0.2 m wide and 0.3 m deep Perspex tank (Fig. 3.1). Following the standard lock-release method [*Kao et al.*, 1985], ISWs of depression are generated. The experimental procedure is described in Section 2.1. The density difference for the performed experiments ranges between 29.5 and 30.6 kg/m^3, obtaining a Boussinesq parameter values (0.0295 $\div$ 0.0306) typical of those ($\sim$ 0.3) observed in coastal ocean regions where solitary waves are forming [*Chen et al.*, 2007].
To produce this initial density stratification, the entire domain is filled with a solution of sodium chloride (NaCl) generating the lower layer of uniform density ρ_2. A density meter (Anton Paar DMA 4100M) is used to measure the density of the saline mixture, with an accuracy of 0.1 kg/m^3. The dashed lines in Fig. 3.1 visualize the interface between the heavier and the light fluid in the initial condition: the gate removal results in a gravity collapse that induces the generation of an ISW of depression, propagating toward the sloping boundary, defined by the angle θ. Each geometric distance (e.g. layers depth, slope legs, lock length) is measured by a ruler, with an error of 1 mm.
At a fixed distance from the front wall of the tank, a CCD (Charged Coupled Device) camera with a frequency of 25 Hz and a spatial resolution of 1024 × 668 pixels, records each experiment. Each pixel has a resolution of about 3 mm × 3 mm. Using image analysis, the pycnocline thickness and the pycnocline position, located at the midpoint of the pycnocline, are inferred. For each generated ISW, I measured the wave amplitude A_w, the wavelength L_w, and the wave surface S_w (Fig. 3.1). The celerity c_w is computed as the first derivative of the trough's position, and the characteristic wavelength λ_w [*Michallet and Ivey*, 1999]is evaluated as:

$$\lambda_w = \frac{1}{A_w} \int\limits_{-\infty}^{+\infty} \eta(x)\,\mathrm{d}x = \frac{S_w}{A_w} \tag{3.1}$$

where $\eta(x)$ is the local pycnocline vertical displacement compared to its original position.

Our goal was to generate well-defined ISWs, in terms of their geometric features, in order to induce, for defined values of the sloping boundary's angle, three different breaking mechanisms. ISWs different breaking mechanisms depend on both incoming ISWs geometric features and slope condi-

Case	Type	ρ_1 [kg/m^3]	ρ_2 [kg/m^3]	x_0 [cm]	η_0 [cm]	h_1 [cm]	h_2 [cm]
1	P	1001.7	1031.7	10.0	18.0	1.2	19.8
2	C	1001.0	1031.6	15.0	9.2	5.0	23.0
3	S	1001.0	1030.5	15.0	13.5	3.3	16.7

Table 3.1: Initial settings for the solitary wave cases considered in this study in terms of breaker type: plunging (P), collapsing (C), surging (S), densities of the upper and lower layer ($\rho_{1,2}$, lock length (x_0), pycnocline displacement (η_0), layers depth in the ambient fluid region ($h_{1,2}$).

Case	Type	A_w [cm]	λ_w [cm]	c_w [cm/s]	s_b	Ir
1	P	3.9	24.8	11.6	0.284	0.7
2	C	3.3	42.4	12.8	0.366	1.3
3	S	5.3	41.1	15.7	0.953	2.6

Table 3.1: Wave characteristics for the solitary wave cases considered in this study in terms of breaker type: plunging (P), collapsing (C), surging (S), wave amplitude (A_w), characteristic wavelength (λ_w), wave celerity (c_w), wave surface (S_w), topographic slope (s_b), and internal Iribarren number (Ir).

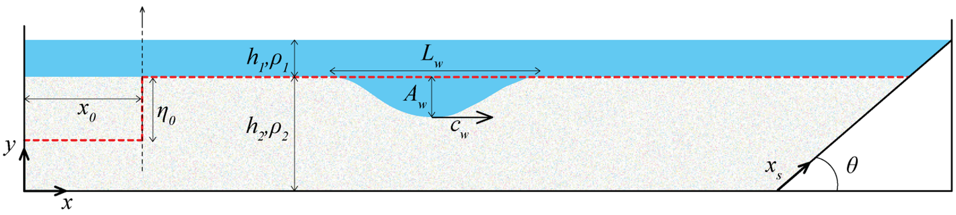

Figure 3.1: Sketch of the domain used to study breaking internal solitary waves (ISWs) on slopes. The dashed line represents the initial pycnocline position in the two layer-stratified fluid. The black dashed vertical line shows the initial position of the lock gate.

tions. Of particular interest has been the breaking mechanisms classification based on the internal Iribarren number, a dimensionless parameter defined as [*Boegman et al.*, 2005; *Aghsaee et al.*, 2010; *Sutherland and Ivey*, 2013]:

$$Ir = \frac{s_b}{\sqrt{\frac{A_w}{\lambda_w}}} \tag{3.2}$$

where $s_b = \tan\theta$ represents the topographic slope.
Chapter 2 shows the empirical relations between the initial experimental setting parameters (x_0, η_0, h_1, h_2) and the wave geometric features (A_w, λ_w). The plunging breakers domain is the region characterized by $Ir < 1$, while collapsing breakers are observed for $Ir = 1 \div 1.5$ and surging breakers for $Ir > 1.5$. The initial experimental parameters and slope values are chosen in order to obtain ISWs that break following three different breaking mechanism. Tabs. 3.1 and 3.1 show the solitary wave cases considered in this study.

3.2 Numerical model, simulations set up and validation

The numerical model was previously applied to study bottom propagating and intrusion lock-exchange gravity currents [*Ooi et al.*, 2007; *Tokyay et al.*, 2011, 2012, 2014] and internal bores [*Borden et al.*, 2012b]. The Boussinesq approximation is employed to account for stratification effects. Here we only briefly describe the main features of the numerical algorithm. The governing Navier-Stokes and density transport equations are solved in non-dimensional form with the channel height, $H = h_1 + h_2$, as the spatial scale and the buoyancy velocity, , as the velocity scale. The reduced gravity is $g' = g\ \frac{\rho_2 - \rho_1}{\rho_2}$, where g is the gravitational acceleration. The dimensionless density field is defined as:

$$\rho^*(x, y, z, t) = \frac{\rho(x, y, z, t) - \rho_1}{\rho_2 - \rho_1} \tag{3.3}$$

The finite-volume viscous solver [*Pierce and Moin*, 2001] advances the Navier-Stokes equations in time using a semi-implicit iterative method. The pressure-Poisson equation is solved using multigrid. The conservative form of the non-dimensional Navier-Stokes equations is integrated on non-uniform Cartesian meshes. All operators in the momentum and pressure equations are discretized using second-order central schemes. The algorithm is second order in time. Discrete energy conservation ensures robustness at relatively high Reynolds numbers despite using strictly non-dissipative (central) schemes to discretise the Navier-Stokes equations. A standard advection-diffusion equation is solved for the non-dimensional density. The Quadratic Upstream Interpolation for Convective Kinematics (QUICK) scheme is used to discretise the advective term in the equation for C. The Fortran 90 parallel code uses Message Passing Interface (MPI). The two parameters in the non-dimensional governing equations are the channel Reynolds number, $Re = ubH/\nu$ and the molecular Schmidt number, $Sc = \nu/\kappa$, in which ν is the molecular viscusity and κ is the molecular diffusivity. The subgrid-scale viscosity and the subgrid-scale diffusivity in the filtered non-dimensional momentum and temperature equations are calculated using the dynamic Smagorinsky model [*Pierce and Moin*, 2001] based on the resolved velocity and density fields at each time instant.

The geometrical set up in a horizontal-vertical plane $x - y$ is shown in Fig. 3.1. A zero flow velocity field is imposed in the domain at the time when the lock gate is released ($t = 0$). All the solid channel boundaries, including the inclined surface, were treated as no-slip surfaces. The flow was assumed to be periodic in the spanwise direction.

The top boundary (free surface of the tank) was treated as a shear-free, slip surface with zero normal velocity. Before the lock gate was released at $t = 0$, the nondimensional density was set up as $\rho^* = 1$ in the region containing the saltier fluid and $\rho^* = 0$ in the remaining part of the tank containing ambient lighter fluid (see red dashed line in Fig. 3.1). A small 3-D disturbance was imposed on the initial concentration field in the regions delimitating the saltier and ambient fluid. The surface-normal concentration gradient was set to zero at all no-slip and free-slip boundaries. The molecular Schmidt number was equal to 100. In all the simulations the grid contained over 70 million nodes with 64 grid points in the spanwise direction. The grid spacing in all three directions was around $0.008H$. Simulations were run with a time step of $0.002H/u_b$. A grid dependency study was conducted for Case 1. It confirmed that the mesh density used in the present simulations was sufficient for the solutions to be considered grid-independent.

In the simulations, the flow is homogeneous in the spanwise direction. This allows defining the mean (spanwise-averaged) variables at any moment in time. The spanwise-averaged values are denoted as $<>$. To interpret more easily the differences among the three cases, the result section analyses the relevant variables in nondimensional form. The nondimensional time scale is $T = H/u_b$. The time scale T is $0.85s$, $0.97s$ and $0.96s$ and the Reynolds number is $Re = 51,160$, $81,136$ and $81,260$ in Cases 1, 2 and 3, respectively. Given that the focus of the present study is on the interaction of the ISW with the sloped surface and that the length of the tank has a small effect on the ISW characteristics before it approaches the sloped surface, the time in each simulation (t') is specified with respect to the time (t_0) at which the horizontal velocity in the upper layer starts to decrease because of the presence of the sloping boundary. In nondimensional form, $t'/T = (t-t_0)/T$ where t is measured with respect to the time at which the lock gate is removed ($t/T = 0$).

Figs. 3.2 and 3.3 use the nondimensional density fields predicted by the numerical simulations to visualize the ISW generated by the lock release as it approaches the inclined surface and starts interacting with it. The steepening of the trailing edge of the wave for Case 1 (Figs. 3.3a-3.3e), the formation of a bolus over the sloping boundary for Case 2 (Figs. 3.2a-3.2e) and the formation of a gravity current flowing up the incline for Case 3 (Figs. 3.3f-3.3l) represent the main events that characterize the breaking mechanism in the plunging, collapsing and surging cases, respectively. The LES/DNS code was validated for several relevant types of flows relevant for the present investigation. *Ooi et al.* [2007] discusses validation results for in-

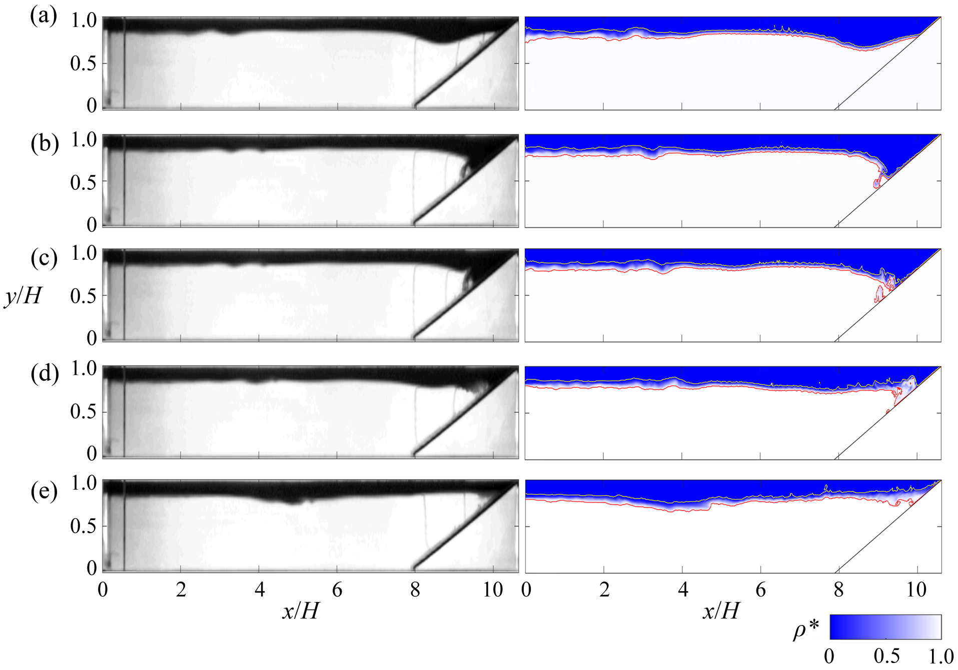

Figure 3.2: Snapshots in time visualizing the heavier fluid in the experiments (on the left) and the nondimensional density fields obtained by numerical simulation (on the right) for the collapsing case (Case 2). Yellow and red lines characterized the 2% and 98% isopycnal surfaces respectively. (a) Initial condition defined as the time at which the horizontal velocity in the upper layer starts to decrease because of the presence of the sloping boundary ($t'/T = 2.4$); (b) bolus generation - point A in the following figures - ($t'/T = 5.8$); (c) mixing induced by the bolus - point B in the following figures - ($t'/T = 7$); (d) the gravity current running up the slope forms - point C in the following figures - ($t'/T = 10.1$); (e) the gravity current reaches the end of the slope - point D in the following figures - ($t'/T = 19.1$).

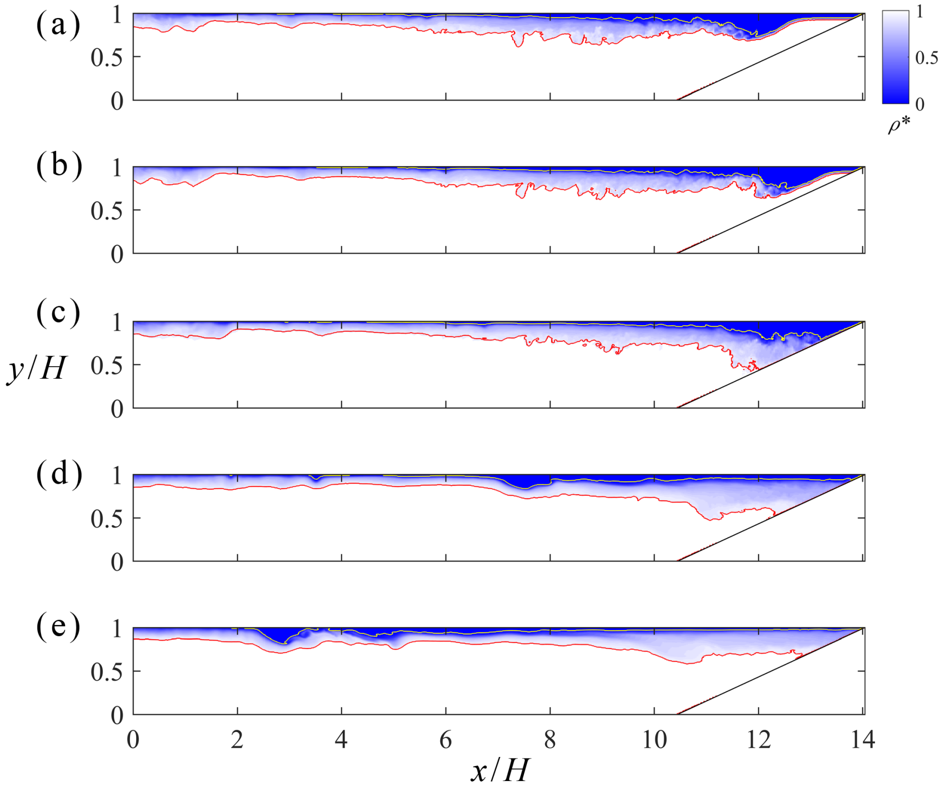

Figure 3.3: Nondimensional density fields predicted by numerical simulation for the plunging case (Case 1) and for the surging case (Case 3, see facing page): (a) the wave approaches the slope ($t'/T = 0$); (b) steepening of the trailing edge ($t'/T = 2.2$); (c) mixing induced by the trailing edge overturning - point E in the following figures - ($t'/T = 6.2$); (d) gravity current flowing up slope - point F in the following figures - ($t'/T = 18.7$); (e) the gravity current stops ($t'/T = 30$).

trusion currents propagating in a two-layer stratified environment. *Tokyay and Constantinescu* [2015] and *Steenhauer et al.* [2017] discuss validation for a gravity current interacting with a large triangular obstacle and lock-exchange currents propagating over a sloped surface, a set up that is directly relevant for the present study once the ISW starts interacting with the sloped surface. *Borden et al.* [2012b] investigated the propagation of internal bores generated in lock-exchange configurations. All these studies contain detailed comparison with experimental data and shallow water theory.

Additionally, we assessed the reliability of the numerical model by comparing the results of the numerical simulations with those obtained from laboratory experiments. For all three cases, the numerical simulations pre-

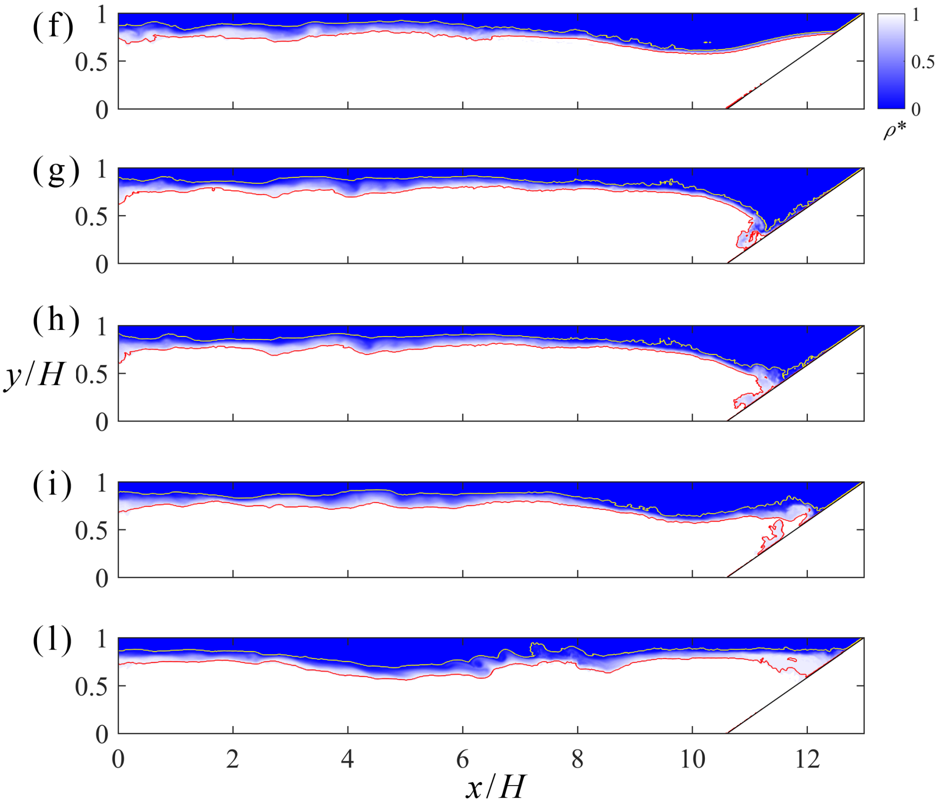

Figure 3.3: Nondimensional density fields predicted by numerical simulation for the plunging case (Case 1, see previous page) and for the surging case (Case 3):(f) the wave approaches the slope ($t'/T = 0$); (g) small instability for boundary layer separation - point G in the following figures - ($t'/T = 3.6$); (h) formation of the gravity current ($t'/T = 4.8$); (i) the gravity current flows up slope - point H in the following figures - ($t'/T = 7.1$); (h) the gravity current stops ($t'/T = 14.9$).

dicted the formation of an ISW with geometric and kinematic features (i.e. amplitude, wavelength and celerity) very close to those observed in the corresponding experiments. For brevity, only numerical results for Case 2, in which a collapsing breaking mechanism is observed, are compared in Fig. 3.2 with experimental visualizations. For the corresponding time steps, the right hand-side of the panel presents the (nondimensional) density field, $< \rho^* >$, predicted by the numerical simulation. In the experiment, the dye used for upper lighter layer allows to directly observe the spatial and temporal evolution of the pycnocline. The numerical model captures very well the main geometric features of the ISW approaching the inclined surface (Fig. 3.2a). The collapsing breaking mechanism involves the formation of a bolus characterized by an anticlockwise vortex, which is clearly visible over the inclined surface [*La Forgia et al.*, 2017]. Both the location of this instability and its geometric features are well captured by the numerical simulation (Figs. 3.2b, 3.2c). The wave breaking induces the generation of a gravity current composed by the lower denser fluid running up the inclined surface (Fig. 3.2d), while the approaching ISW is partially reflected (Fig. 3.2e).

3.3 Entrainment in internal solitary waves

During the ISWs generation phase, the pycnocline region entrains both fresh and salty water, increasing its volume. Once the lock gate is released, the initial potential energy is converted into kinetic energy, and mixing occurs between the upper layer containing lighter fluid and the lower layer containing heavier fluid. The fresh water entrainment velocity can be estimated as the fresh water discharge per unit area crossing the interface between the two fluids defined by an iso-density level ($< \rho^* >= 0.02$) in the vertical $x-y$ plane.

This procedure is similar to the one used by *Adduce et al.* [2012]; *Cenedese and Adduce* [2008]; *Nogueira et al.* [2014]; *Ottolenghi et al.* [2016b, 2017b, c]. The salty water entrainment velocity is estimated in a similar way using the water discharge per unit area crossing the interface defined by the iso-density level $< \rho^* >= 0.98$ in the vertical $x-y$ plane. Fig. 3.3a shows the $< \rho^* >= 0.02$ and $< \rho^* >= 0.98$ iso-density levels as the ISW is approaching the inclined surface in Case 2. The arrows perpendicular to the iso-density surfaces identify the direction of the entrainment discharge. We define the mixed layer as the region enclosed by these two iso-density levels. The water discharge per unit area crossing these interfaces represents entrainment into the mixed layer. It can be described by the time-variation of the mixed layer region volume enclosed between the two iso-density levels in the vertical $x-y$ plane.

If at $t = t_0$ ($t'/T = 0$) the initial volume of the mixed layer is Vm_0, at a successive time $t_i = t_0 + \Delta t_i$ the mixed layer has a larger volume $Vm_t = Vm_0 + \Delta V_i$. The change in volume ΔV_i can be estimated as $\Delta V_i = (A_t - A_0)d$, where d is the spanwise dimension of the domain, A_t is the area enclosed between the iso-density levels in the vertical $x-y$ plane at time t_i, and A_0 is the initial area of the mixed layer at $t = t_0$. A bulk entrainment discharge can be calculated at each time:

$$Q_{ei} = \Delta V_i / \Delta t_i \tag{3.4}$$

Then, one can define a bulk entrainment velocity:

$$W_{ei} = Q_{ei} / S_i \tag{3.5}$$

where the interface S_i is obtained as the sum of the iso-density surfaces defining the boundaries of the mixed layer region. The bulk entrainment parameter EP is a dimensionless number obtained by dividing the bulk entrainment velocity to the ISW celerity:

$$EP_i = W_{ei} / c_w \tag{3.6}$$

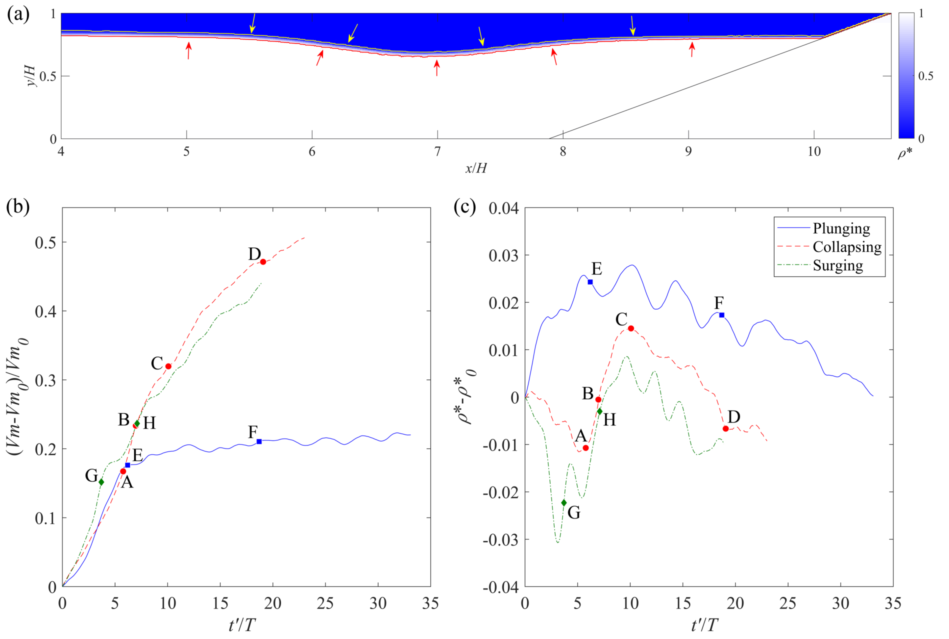

Figure 3.4: Analysis of entrainment process (a): Case 2, nondimensional density. The arrows identify the direction of the entrainment which occurs perpendicularly to the 2% and 98% isopycnal surfaces (yellow and red lines, respectively). Frames (b) and (c) show the temporal evolution of the dimensionless volume and averaged density of the mixed layer, respectively. Results are shown for Case 1, plunging breaker (solid lines), for Case 2, collapsing breaker (dashed lines) and for Case 3, surging breaker (dash-dot lines).

For each case, the temporal variations of the nondimensional mixed layer volume, Vm/Vm_0, and averaged density, $\rho^* - {\rho^*}_0$, are plotted in Figs. 3.4b and 3.4c, respectively. The index 0 is used to denote the values of these variables at $t = t_0$.

Before the ISW reaches the inclined surface (initial phase, $t'/T < 6$), the mixed layer volume increases with time at an approximately constant rate in all three cases (Fig. 3.4b). By contrast, the averaged density does not show a similar variation in the three cases for $t'/T < 6$ (Fig. 3.4c). After this initial phase, the temporal variations of the mixed layer volume is a function of the breaking dynamics of the ISW. For the collapsing and the surging cases, the mixed layer volume continues to increase with about the same initial rate (Fig. 3.4a). Meanwhile, a much smaller rate of increase of the mixed layer volume with time is observed in the plunging case for $t'/T > 6$ (Fig. 3.4a). This is due to the slow decrease of the mean density of the mixing layer (Fig. 3.4b). The temporal variation of the averaged density is non-monotonic for $t'/T > 6$ for all three cases. For the collapsing and the surging cases, $\rho^* - {\rho^*}_0$ first increases until $t'/T = 10$, then it starts decreasing in a non-monotonic way (Fig. 3.4b). The non-monotonic decay of $\rho^* - {\rho^*}_0$ is observed starting immediately after the end of the initial phase in the plunging case. Depending on the breaking dynamics, the change of the mixed layer volume and averaged density are affected by the entrainment associated with instantaneous mutual contributions of fresh and salty water. The physical processes affecting the mixed layer evolution can be described by considering the temporal evolution of the bulk entrainment parameter. In particular, one can distinguish between the global bulk entrainment parameter of the mixed layer (black lines in Fig. 3.4) and the bulk entrainment parameter evaluated by considering the $\langle \rho^* \rangle = 0.02$ and 0.98 isopycnal surfaces. The former characterizes the entrainment of the fresh water into the salty water (green lines in Figs. 3.4), while the latter characterizes the entrainment of the salty water into the fresh water (red dashed lines in Figs. 3.4). As the collapsing breaker approaches the inclined surface in Case 2, it modifies its shape without developing any visible instability (Fig. 3.2a). Its trailing edge steepens, while its leading edge tends to assume the same slope as the incline. As this happens, the wave partially dissipates. The mixed layer increases its volume by entraining mostly fresh water. This is the main reason why its mean density decreases for small t'/T (e.g., until point A in Figs. 3.4b, 3.4c and 3.5a). As the ISW starts breaking, a bolus characterized by an anticlockwise motion forms and then dissipates fairly rapidly (Figs. 3.2b, 3.2c). This event induces a sudden change of the bulk entrainment parameter due to the increase of the brine water discharge into the mixed layer, which increases its density (see time interval between points A and B in Figs. 3.4b, 3.4c and 3.5a). The generation of a gravity current flowing up the inclined surface is consistent with the anticlockwise direction of the vortex generated by the interaction of the IBW with the inclined surface (see Figs. 3.2d and 3.2e and point C in Figs. 3.4b, 3.4c and 3.5a). The gravity current propagates upslope, interacting with the upper layer containing fresh water. As a result, the gravity current entrains lighter water (see time interval between points C and D in Figs. 3.4b, 3.4c and 3.5a), which explains the decrease of the mixed layer averaged density. The disappearance of a well-defined gravity current marks the end of the breaking event. At larger times, the incident wave is partially reflected and the mixed layer density becomes approximately constant (see time interval after point D in Fig. 3.4c).

For the plunging breaker case, the interaction of the ISW with the slop-

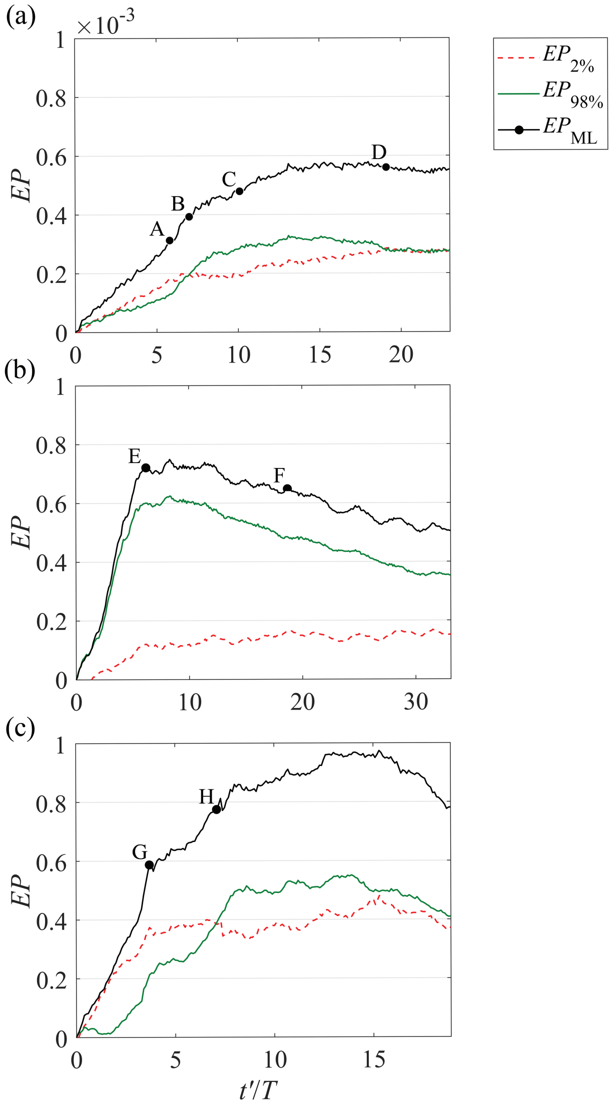

Figure 3.5: Temporal variation of bulk entrainment parameter (EP) for the collapsing case (a), the plunging case (b) and the surging case (c). The dashed lines show the EP obtained by using the 2% isopycnal surface (entrainment of fresh water); the green solid lines show the EP obtained by using the 98% isopycnal surface (entrainment of salty water). The black solid lines show the EP obtained by using both the 2% and 98% isopycnal surfaces (entrainment of the fresh water and salty water into the mixed layer).

ing boundary (Figs. 3.3a-3.3c) results in the steepening of the rear edge of the wave and its subsequent overturning in the onshore direction [*La Forgia et al.*, 2017]. This results in the formation of a clockwise rotating patch of heavier fluid due to the Rayleigh-Taylor instability which causes entrainment of lower-layer, salty water [*Aghsaee et al.*, 2010]. During the initial stages, an increase of the mixed layer volume and density is observed. It is due to entrainment of salty water into the mixed layer (see time interval before point E in Figs. 3.4b, 3.4c and 3.5b). The rotating patch of fluid slowly dissipates as it entrains less and less brine water. At the same time, as for the collapsing case, a gravity current forms and flows upslope (Fig. 3.3c), entraining lighter water into the mixed layer (Figs. 3.3d-e). Consequently, a decrease of the mixed layer mean density is observed due to a fresh water entrainment (see time interval after point E in Figs. 3.4b, 3.4c and 3.5b).
For the surging breaker case, the ISW dynamics is comparable to that observed in the collapsing case. As the wave interacts with the sloping boundary, it changes its shape and partially dissipates as it entrains fresh water ($t'/T < 2$ in Figs. 3.4b, 3.4c and 3.5c). When the wave trough reaches its lowest position over the sloped surface, boundary layer separation occurs, inducing the formation of a bolus (Fig. 3.3g) characterized by an anticlockwise motion. It quickly dissipates causing mixing. Eventually the bolus evolves into a gravity current like flow that advects fresh water upslope (Figs. 3.3h-i). This induces a quick increase of the mixed layer density which entrains rapidly salty water (see time interval before point G in Figs. 3.4b, 3.4c and 3.5c). In a first phase, the gravity current flow moves upwards over the sloped boundary, intruding into the mixed layer, whose mean density increases (see time interval between points G and H in Figs. 3.4b, 3.4c and 3.5c). As it propagates over the sloped boundary and approaches the free surface, the gravity current decelerates and interacts with the upper layer containing fresh water (Fig. 3.3l). As this happens, a decrease of the mixed layer mean density due to entrainment of fresh water is observed (see time interval after point H in Figs. 3.4b, 3.4c and 3.5c), which is similar to what was observed in the collapsing case. Later on, the entrainment of salty water remains roughly unchanged, while the entrainment of fresh water increases with time. Probably, this is due to the horizontal rearrangement of the mixed layer towards a more stable hydrostatic condition.

3.4 Potential energy and irreversible mixing

Mixing within a breaking ISW is herein quantified by the energy budget method of *Winters et al.* [1995] which has been widely used in literature [e.g. *Fragoso et al.*, 2013; *Patterson et al.*, 2006; *Ottolenghi et al.*, 2016a, b]. This method does not consider the change in the volume of the mixed layer; thus it is not required to define any iso-density interface. Considering the two-dimensional (spanwise-averaged) density field $\rho(x, y)$ for a closed system, where x and y are the streamwise and vertical coordinates, respectively, mixing of the density field corresponds to a change in the probability density function (pdf) of density induced by mass diffusion. This change results in a reduction of the density variance. Turbulence enhances the blending of fluid parcels by steepening scalar gradients and increasing iso-scalar surfaces, the regions along which diffusion develops [*Winters and D'Asaro*, 1996]. In the energy budget method, diabatic and adiabatic processes are distinguished. An adiabatic process can change the potential energy of the fluid by switching the kinetic energy into potential energy without inducing any diffusive mixing (i.e. no heat or mass transfer occurs). The diabatic processes properly quantify the energetics of mixing. They are responsible for the change of the total potential energy of the fluid due to irreversible molecular diffusion. In order to distinguish between the contribution of diabatic and adiabatic processes, the concepts of background and available potential energy have to be introduced [*Winters et al.*, 1995]. The volume-integrated kinetic and gravitational potential energy of the flow is defined as:

$$E_k\left(t\right) = \frac{\rho_0}{2} \int\limits_V \left(u^2 + v^2\right) \mathrm{d}V \tag{3.7}$$

$$E_p\left(t\right) = g \int\limits_V \left\langle \rho\left(x, y, t\right)\right\rangle \, y \, \mathrm{d}V \tag{3.8}$$

where ρ_0 is a constant reference density, u and v are the streamwise and vertical velocity respectively, $< \rho(x, y, t) >$ is the local instantaneous spanwise-averaged density field, and V is the entire volume of the domain. The volume-integrated background potential energy is defined as:

$$E_b\left(t\right) = g \int\limits_V \left\langle \tilde{\rho}\left(x, y, t\right)\right\rangle \, y \, \mathrm{d}V \tag{3.9}$$

where $\langle \tilde{\rho}(x, y, t)\rangle$ represents the spanwise-averaged density field in the configuration of minimum of the potential energy obtained by sorting the fluid parcels by an adiabatic volume-conserving rearrangement. The background

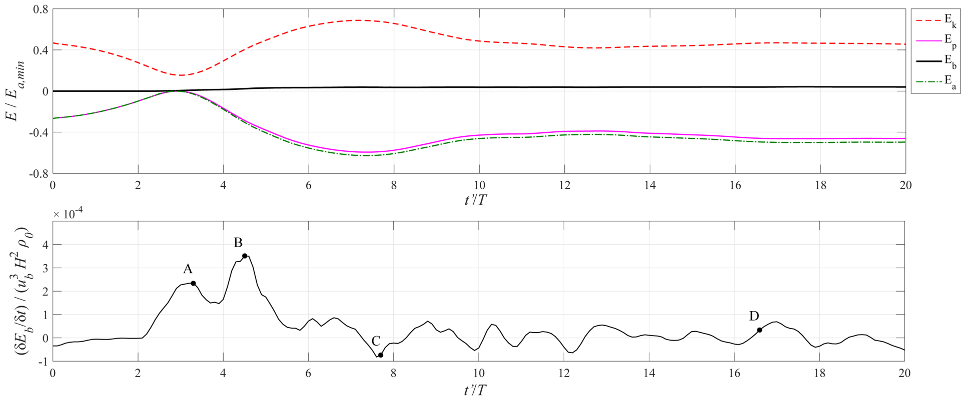

Figure 3.6: Volume-integrated energy results for the collapsing case (a). Kinetic energy (E_k), total potential energy (E_p), background potential energy (E_b), and available potential energy (E_a), all normalized by $|E_{a,min}|$. (b) Background potential energy evolution for the collapsing case.

potential energy is uniquely defined by the pdf of density and thus is independent of the instantaneous spatial distribution of density in the flow domain. The difference between the total energy and the background potential energy defines the volume-integrated available potential energy:

$$E_a\left(t\right) = E_p(t) - E_b(t) \tag{3.10}$$

The available potential energy quantifies the amount of potential energy released in the adiabatic transition from $\langle\rho\left(x,y,t\right)\rangle$ to $\langle\tilde{\rho}\left(x,y,t\right)\rangle$ without altering the pdf of density. It is the amount of potential energy stored in the fluid when it is not in gravitational equilibrium [*Lorenz*, 1955]. Changes in the background potential energy are thus associated to the energy consumed in mixing the fluid and can be used to characterize this process.

The energy budget was evaluated for all cases. Qualitatively, the temporal variations of the kinetic energy, total background potential energy and available potential energy terms were similar in these cases. For brevity, only results for the collapsing case are presented in Fig. 3.6a. When plotted, the energy variables E have the initial value E_0 removed. The dimensional variables are then normalized by the absolute value of the minimum available potential energy $|E_{a,min}|$. The energy that is no longer available due to irreversible mixing can be evaluated by calculating the change in background potential energy between consecutive states of the system. Figure 3.6b shows the time evolution of the nondimensional background potential energy for the collapsing case. It is normalized by ${u_b}^3H^2\rho_0$, where u_b is the buoyancy velocity.

As the wave starts to feel the presence of the sloping boundary, its celerity decreases. As a result, the volume-integrated kinetic energy inside the domain starts decaying. As this happens, the ISW is modifying its shape and the lighter fluid parcels tend to move downwards (Fig. 3.2a). For this reason, both the total and the available potential energies increase, while remaining equal to each other. The background potential energy is thus equal to zero. The kinetic energy starts to increase during the breaking event. The motion induced by the boundary layer separation (Fig. 3.2b) uplifts the lighter water parcel and induces mixing. The time evolution of the background potential energy shows the presence of a first peak during the time interval the bolus forms and of a second, more pronounced, peak during the time period when the whirling motion causes mixing (points A and B, respectively, in Fig. 3.6b). As the anticlockwise vortex loses its coherence, the rate of change of E_b decreases. This lasts until the formation of the gravity current (point C in Fig. 3.6b). The fluid motion inside the domain is now characterized by the presence of a gravity current flowing upslope and a reflected wave moving offshore. For these reasons, the kinetic energy and the potential energy assume their maximum and minimum values, respectively. When the gravity current flows upslope it induces mixing, which in turn results in slight variations of the background potential energy. In particular, when the gravity current reaches its highest position over the sloping boundary (Fig. 3.2e), a more pronounced variation of E_b is observed (point C in Fig. 3.6b).

The rate of change of the background potential energy is not a direct measure of the amount of mixing. Rather the mixing efficiency is used to quantify mixing, by evaluating the relation between the change in pdf and the system energetics. In a stratified flow, the mixing efficiency quantifies the fraction of energy consumed by irreversible diabatic mixing related to the amount of energy available to support this process (i.e. the mechanical energy). As widely used in previous experimental and computational studies [e.g. *Ivey and Imberger*, 1991; *Peltier and Caulfield*, 2003; *Dalziel et al.*, 2008; *Prastowo et al.*, 2009], the instantaneous mixing efficiency is defined as:

$$\eta = \frac{\Delta E_b}{|\Delta E_T|} \tag{3.11}$$

where Δ is the change between two consecutive states of the system, and E_T is the instantaneous total mechanical energy of the fluid:

$$E_T\,(t) = E_a(t) + E_k(t) \tag{3.12}$$

Fig. 3.7 shows the temporal variation of the mixing efficiency in the three

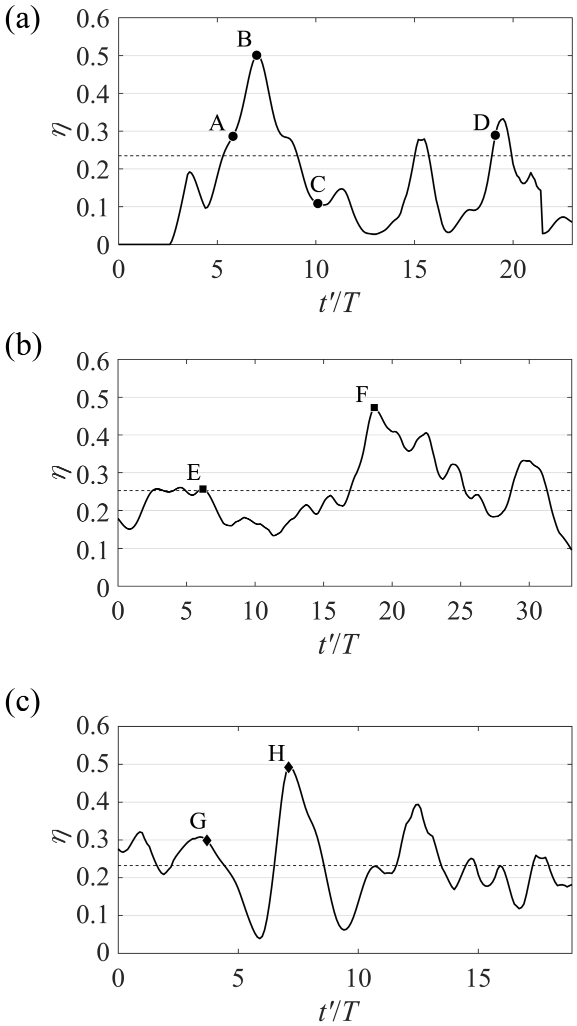

Figure 3.7: Instantaneous mixing efficiency η and bulk mixing efficiency η_m (dashed lines). (a) collapsing case; (b) plunging case; (b) surging case.

cases and its mean value during the corresponding breaker event. For the collapsing case, as the wave approaches the incline, it decelerates and consequently partially dissipates. The first peak of the mixing efficiency is observed for $t'/T < 5$ (Fig. 3.7a) as the volume-integrated kinetic energy starts to decrease (Fig. 3.6a). Then, as the the wave interacts with the sloping boundary, the changes in wave geometric and kinematic features cause an approximately linear increase of the mixing efficiency with time. Its maximum value is recorded during the dissipation of the anticlockwise vortex induced by the boundary layer separation (point B in Fig. 3.7a). During the upslope propagation of the gravity current, the value of η increases in an irregularly way. Three peaks of increasing magnitude are observed during the time interval between point C and point D (Fig. 3.7a). During this phase, the mixing peaks when the gravity current reaches the upper layer close to the free surface (point D in Fig. 3.6a). Because of the interaction between the gravity current and the surrounding lighter fluid, mixing is strong, which explains the peak in the mixing efficiency at point D.

In the plunging case (Fig. 3.7b), the clockwise vortex induced by the overturning of the rear edge of the wave causes the entrainment of a large amount of salty water for $2 < t'/T < 8$ (point E in Fig. 3.5b). The mixing efficiency then decreases before starting to increase again for $t'/T > 12$ and it peaks around $t'/T = 18$ (point F in Fig. 3.7b). During this phase, the formation of the gravity current is observed. As the gravity current flows upslope, it entrains lighter fluid (Fig. 3.5b), which causes mixing. For the same reason explained in the collapsing case, when the gravity current reaches the upper layer close to the free surface, the mixing and mixing efficiency peak again ($t'/T = 30$ in Fig. 3.7b).

The instantaneous mixing efficiency for the surging case contains four peaks (Fig. 3.7c). The first one occurs for $t'/T = 2$, as the wave interacts with the sloping boundary, which induces strong dissipation. As the wave trough reaches its lowest position over the incline, small instabilities develop due to boundary layer separation. A peak of the mixing efficiency occurs at this time (point G in Fig. 3.7c). The breaking event continues with the formation of a gravity current flowing upslope that induces strong local mixing. The peak of the mixing efficiency is reached when the gravity current reaches its highest position over the sloped boundary (point H in Fig. 3.7c). Around $t'/T = 13$, a third peak of the mixing efficiency is observed. This peak is probably due to the horizontal rearrangement of the mixed layer towards a stable hydrostatic condition.

3.5 Bed shear stress and sediment entrainment potential of an ISW interacting with a sloped surface

One of the advantages of 3-D eddy-resolving simulations it that they allow estimating the bed friction velocity distributions on the sloped boundary once the ISW starts interacting with this surface. This is important, given that the bed friction velocity is the main variable that affects the flux of sediment entrained from the sloped boundary in the case of a loose bed. Next, the nondimensional distributions of the bed friction velocity, u_τ/u_b, at relevant times after the ISW starts interacting with the sloped boundary are discussed for the plunging, collapsing and surging cases in Figs. 3.8, 3.9 and 3.10, respectively. To facilitate understanding the effect of the interaction between the ISW and the sloped boundary on the bed friction velocity distributions, the nondimensional spanwise-averaged density field and the 3-D interface ($\rho^* = 0.5$) are also included in Figs. 3.8, 3.9 and 3.10.

Fig. 3.8 shows that as the ISW reaches the sloped boundary, a large amplification of the bed shear stress occurs in the plunging case because of the thin layer of salty water flow pushed down the incline by the approaching wave. For example, a region of high bed friction velocity amplification is observed for $0.4 < x'/H < 1.2$ at $t'/T = 4.5$ in Fig. 3.8a. Interestingly, the bed shear stress distribution within this region is close to uniform in the spanwise direction indicating the thin layer of heavier fluid close to the sloped boundary contains negligible turbulence. This is confirmed by the distribution of the nondimensional density at the same time instant that shows basically no mixing at the interface between the two layers until $x'/H = 1.2$ where the strongly-coherent Kelvin-Helmholtz (KH) billows forming at the back of the ISW start interacting with the inclined boundary. Consistent with this, the 3-D interface, also visualized in Fig. 3.8a at $t'/T = 4.5$, shows only weak disturbances developing for $x/H < 1$ ($x'/H < 2$). Large-scale disturbances in both the streamwise and spanwise directions develop behind the crest of the wave due to the shedding of KH vortices and their subsequent 3-D stretching. Analysis of the spanwise averaged distributions of bed friction velocity in Fig. 3.8e confirm that the largest levels of u_τ/u_b are observed around $t'/T = 4.5$ beneath the thin layer of accelerating heavier fluid trapped between the ISW and the sloped boundary and also in the region where the large interfacial KH billows penetrate until close to the sloped boundary.

Once the rear edge of the ISW overturns, lots of turbulence is generated along the sloped boundary. This is the main reason why the distributions of u_τ/u_b become very irregular in the spanwise direction for $t'/T > 5$, especially in the region containing mixed fluid that is situated in the immediate vicinity of the boundary (see Figs. 3.8b, 3.8c and 3.8d). For example, at $t'/T = 8$, the interface displays a region of high-amplitude 2-D disturbances between the location where the bottom of the layer of light unmixed fluid is situated over the sloped boundary ($x'/H < 0.6$) and the bottom part of the region containing mixed fluid over the same boundary ($x'/H > 1.6$). This confirms that the breaking of the ISW, as it hits the sloped boundary, generates highly 3-D eddies and lots of mixing. The peak bed friction velocities at $t'/T = 8$ are observed around $x'/H = 1$ and 1.2 where the flow accelerates after the momentum changes direction from being oriented parallel to the streamwise direction to being oriented down of the sloped boundary. A smaller, but clear amplification of u_τ/u_b occurs inside the layer of lighter fluid because some of the incoming fluid in the ISW is pushed against the incline toward the top corner of the channel. The presence of energetic 3-D eddies inside the mixed layer away from the region where this layer is in direct contact with the sloped boundary explains the relatively strong disturbances of u_τ/u_b in the spanwise direction for $2 < x'/H < 2.7$ at $t'/T = 8$ in Fig. 3.8b. The largest bed friction velocity values are observed near the top and bottom boundaries of the layer of mixed fluid as it comes into contact with the sloped boundary (see also Fig. 3.8e). This is also observed at subsequent times (e.g., $t'/T = 12$ and $t'/T = 14$ in Figs. 3.8c and 3.8d) after the gravity current containing saltier water forms and the reflected wave starts moving away from the sloped boundary. As the gravity current advances against the bed slope, the peak values of u_τ/u_b and the degree of non-uniformity of the bed friction velocity distribution in the spanwise direction decreases. This is also due to the gradual loss of coherence of the larger eddies generated inside the mixed layer during the time the incoming wave hits the sloped boundary. The decay of the larger-scale turbulence is confirmed by the decay of the 3-D disturbances on the surface of the $\rho^* = 0.5$ isopycnal for $t'/T > 8$.

Similar to the plunging case, the largest amplification of the bed shear stress in the collapsing case occurs a short time after the ISW starts interacting with the sloped boundary and starts displacing the heavier fluid downwards in the vicinity of the sloped boundary (see distributions of bed friction velocity at $t'/T = 4.0$ in Figs. 3.9a and 3.9e). At these early times of the interaction of the ISW with the sloped boundary there is negligible large-scale turbulence generated in the flow, which explains why the distributions of u_τ/u_b are close to uniform in the spanwise direction. The flow in the immediate vicinity of the sloped surface remains laminar and the distributions of u_τ/u_b are close to uniform in the spanwise direction. It is only after the bolus forms ($t'/T > 5$) that the distributions of u_τ/u_b become nonuniform in the spanwise direction. As the gravity current associated to the formation of the bolus moves upwards and the wave reflection at the sloped boundary is complete, large-scale 3-D turbulent eddies start developing inside the mixed layer (e.g., see also interface deformations for $t'/T > 10$ in Fig. 3.9) and the bed friction velocity distributions become highly nonuniform beneath and some distance behind the front of the gravity current. At these times, the largest values of u_τ/u_b are observed around the location of the front of the gravity current. Interestingly, the u_τ/u_b in the region where the thin layer of mixed fluid comes into contact with the sloped boundary remain high even after the end of the breaking event (e.g., at $t'/T = 26.5$ in Fig. 3.9d). As for the plunging case, the turbulence inside the mixed layer and the degree of nonuniformity of u_τ/u_b in the spanwise direction decays after the gravity current dissipates and the mixed layer becomes close to horizontal neat the sloped boundary.

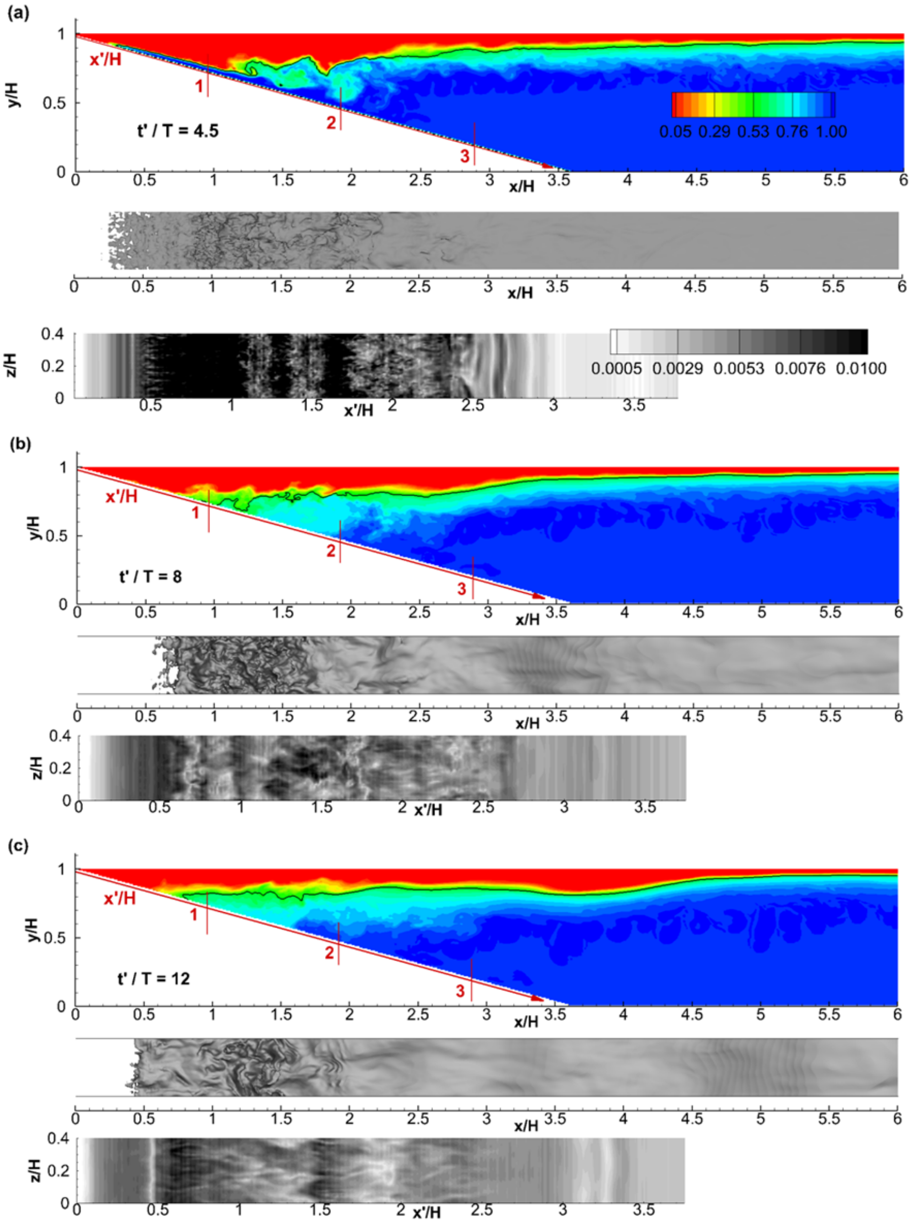

Figure 3.8: (a,b,c). For caption see facing page.

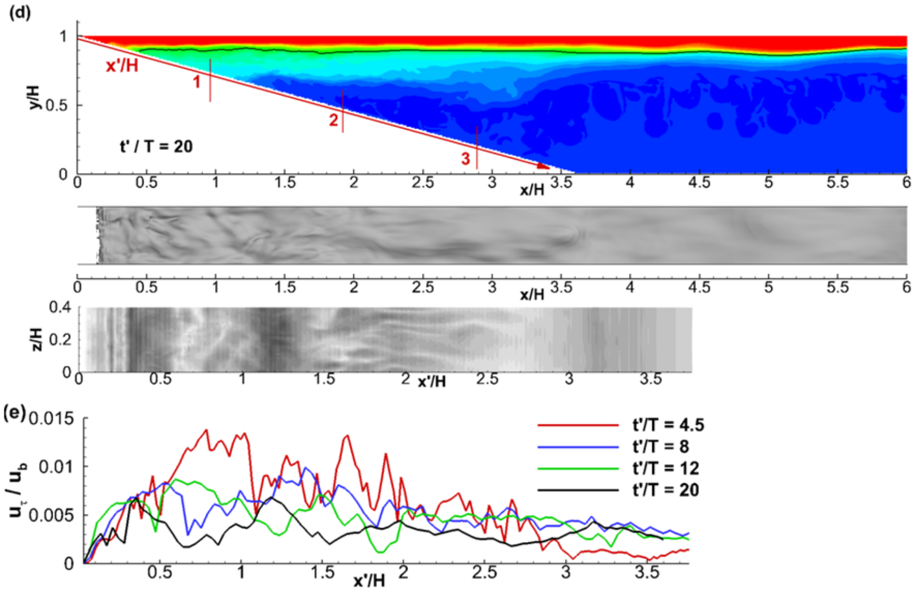

Figure 3.8: Nondimensional density field (top), 3-D interface represented by the $\rho^* = 0.5$ isopycnal surface (middle), and normalized bed shear velocity contours, u_τ/u_b, over the sloping boundary (bottom) for the plunging case. a) $t'/T = 4.5$; b) $t'/T = 8.0$; c) $t'/T = 12.0$; d) $t'/T = 20.0$. Also shown in frame e are the spanwise-averaged bed friction velocity contours over the sloping boundary.

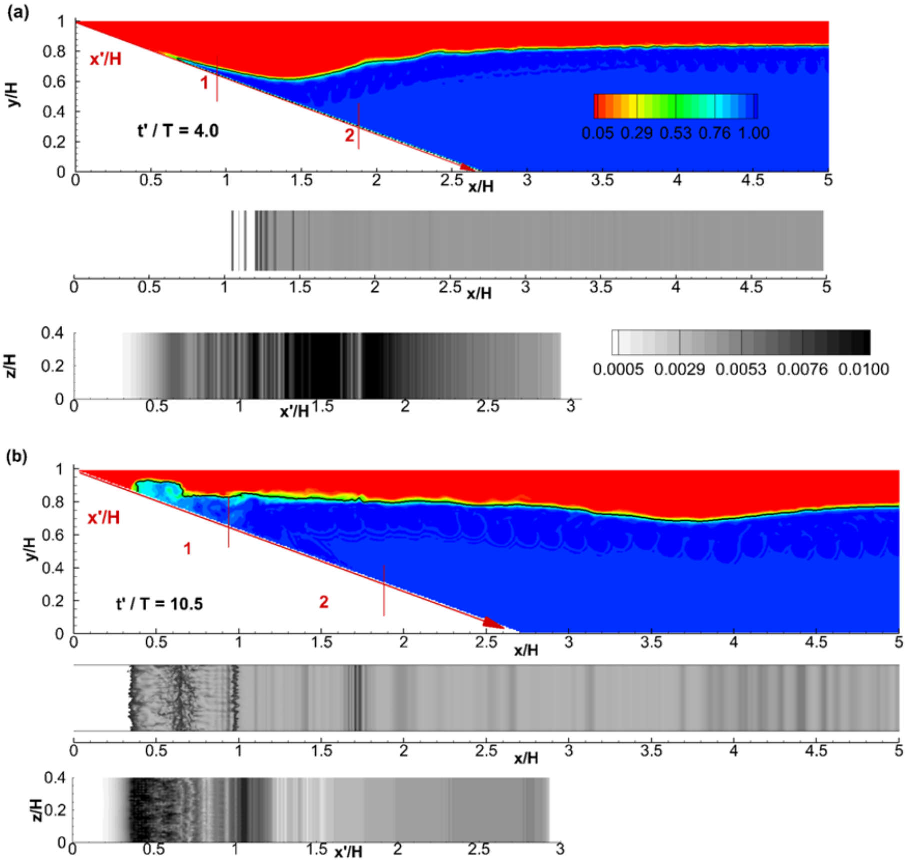

Figure 3.9: (a,b). For caption see facing page.

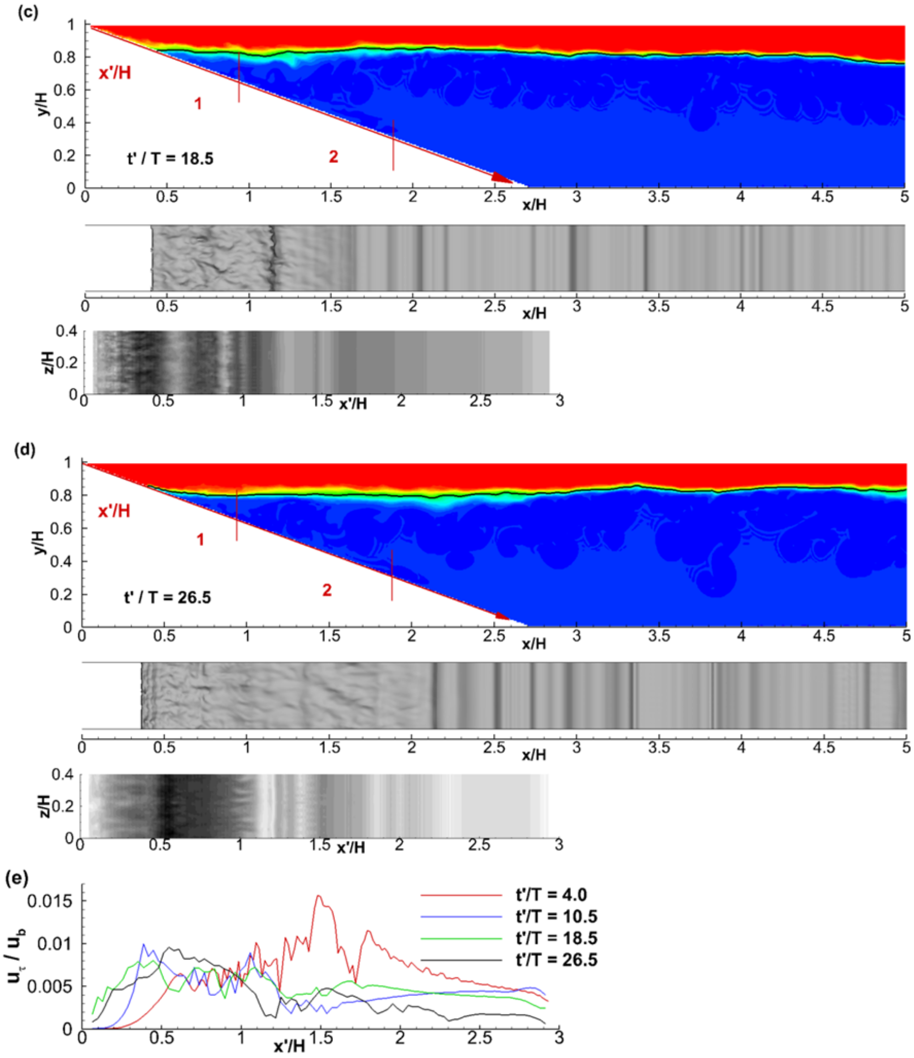

Figure 3.9: Nondimensional density field (top), 3-D interface represented by the $\rho^* = 0.5$ isopycnal surface (middle), and normalized bed shear velocity contours, u_τ/u_b, over the sloping boundary (bottom) for the collapsing case. a) $t'/T = 4.0$; b) $t'/T = 10.5$; c) $t'/T = 18.5$; d) $t'/T = 26.5$. Also shown in frame e are the spanwise-averaged bed friction velocity contours over the sloping boundary.

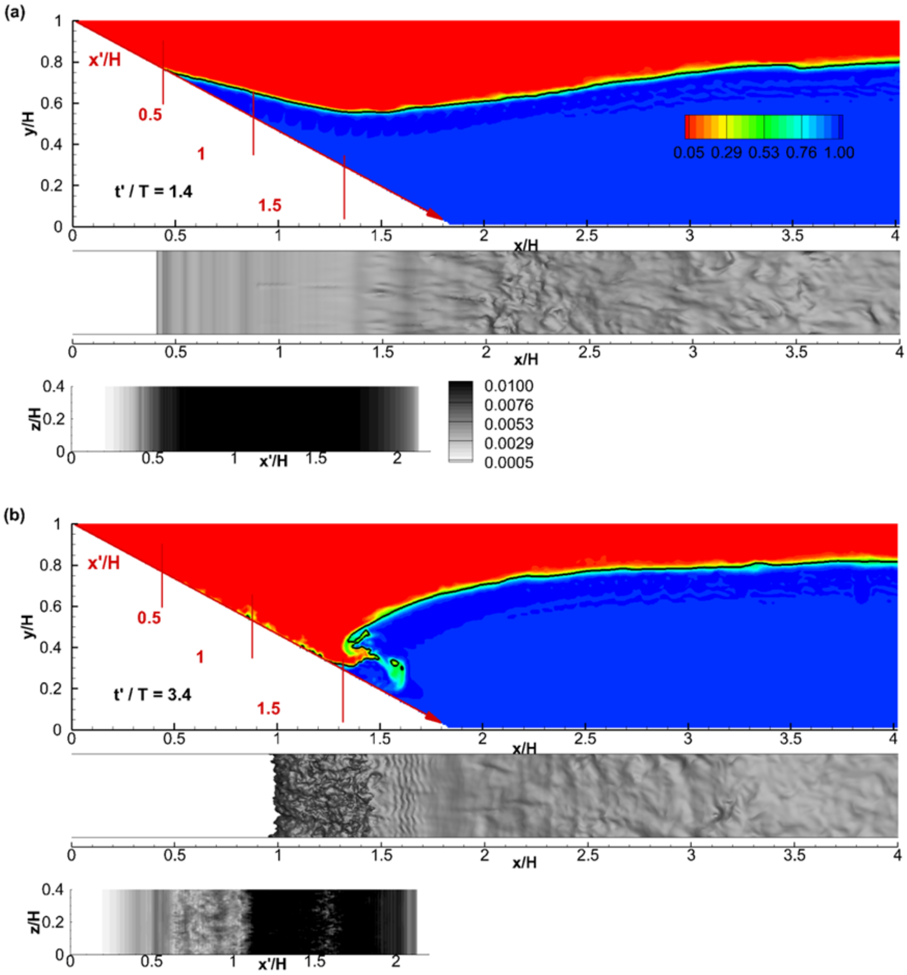

Figure 3.10: (a,b). For caption see facing page.

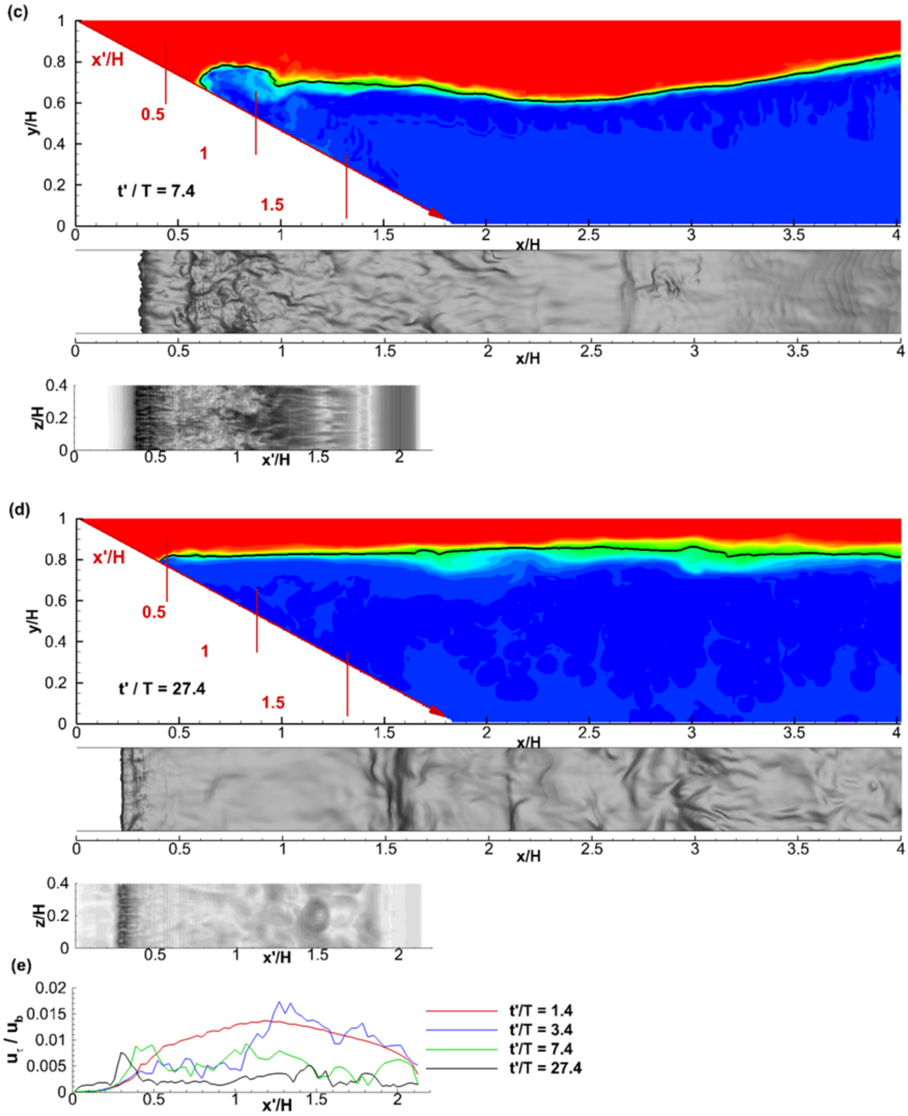

Figure 3.10: Nondimensional density field (top), 3-D interface represented by the $\rho^* = 0.5$ isopycnal surface (middle), and normalized bed shear velocity contours, u_τ/u_b, over the sloping boundary (bottom) for the surging case. a) $t'/T = 1.4$; b) $t'/T = 3.4$; c) $t'/T = 7.4$; d) $t'/T = 27.4$. Also shown in frame e are the spanwise-averaged bed friction velocity contours over the sloping boundary.

Similar to the collapsing case, the large values of u_τ/u_b in the surging case occur as the front of the ISW approaches the sloped boundary ($t'/T = 1.4$, Figs. 3.10a and 3.10e) and the bolus forms (Figs. 3.10b and 3.10e). As for the previous cases, the distributions of u_τ/u_b are close to uniform in the spanwise direction before the formation of the bolus despite the fact that large-scale instabilities develop on the rear side of the approaching wave (e.g., see $\rho^* = 0.5$ interface at $t'/T = 1.4$ in Fig. 3.10a). As opposed to the other cases, where the region of high u_τ/u_b over the sloped boundary approximately corresponded to the extent of the mixed layer over the same boundary, in the collapsing case the region of high u_τ/u_b penetrates into the regions containing unmixed fluid above and below the thin mixing layer. Before the bolus forms the region of high u_τ/u_b extends only beneath the mixed layer (e.g., for $x'/H < 1.5$ in Fig. 3.10a) where the flow accelerates as the crest of the approaching wave moves toward the sloped boundary. However, the formation of the bolus induces the formation of 3-D eddies, some of them being advected into the layer containing light unmixed fluid close to the surface of the sloped boundary (Fig. 3.10b). This explains the large fluctuations of u_τ/u_b in the spanwise direction starting around $x'/H = 0.5$ at $t'/T = 3.4$. Moreover, at $t'/T = 3.4$ the region containing the peak values of u_τ/u_b starts at $x'/H = 1.1$, way above the mixed layer which is situated at $x'/H = 1.5$ and extends until $x'/H = 2.1$, way inside the layer containing heavier fluid. As for the other cases, once the upward moving gravity current forms, the largest values of u_τ/u_b are recorded beneath the front of the current until close to the time when the current dissipates (Figs. 3.10c, 3.10d). As the current dissipates and the mixing layer becomes close to horizontal away from the sloped boundary, the flow starts relaminarizing (e.g., see $\rho^* = 0.5$ interface at $t'/T = 27.4$ in Fig. 3.10d) and the distributions of u_τ/u_b over the sloped boundary become more uniform in the spanwise direction (see Figs. 3.10c and 3.10d). As for the collapsing case, some entrainment can occur around the region where the mixed layer comes into contact with the sloped boundary a long time after the wave has reflected (e.g., see distribution of u_τ/u_b near $x'/H = 0.3$ at $t'/T = 27.4$ in Fig. 3.10d).

One interesting question is how the differences in the bed friction velocity distributions during the different stages of the evolution of the ISW affects its overall capacity to entrain sediment from the sloped boundary. Various semi-empirical models are available to estimate the instantaneous flux of sediment entrained from the bed by a turbulent overflow. Most of these models assume that the sediment flux is proportional to $u_\tau{}^\varphi$ or to $(u_\tau{}^2 - u_{\tau c}{}^2)^{\varphi/2}$, where the former is commonly used for live-bed scour conditions (e.g., $\varphi = 3$ in the *Meyer-Peter and Muller* [1948] formula) and the latter is generally

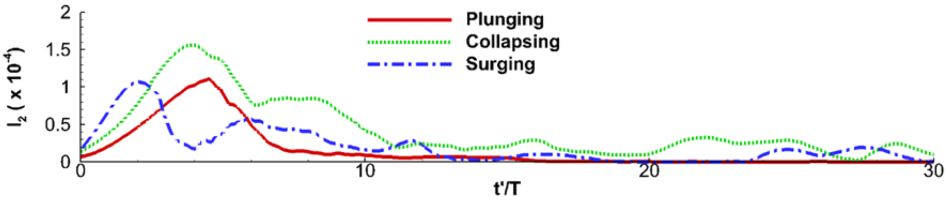

Figure 3.11: Temporal variation of the entrainment function I_2 for the plunging, collapsing and surging cases. Critical shear velocity is taken as $u_{\tau c0} = 0.005 u_b$ for all cases.

used for clear-water scour conditions (e.g., *Van Rijn* [1984] formula). For example, *Van Rijn* [1984] formula (Eq. 3.13) assumes that the local pick up rate P is proportional to $({u_\tau}^2 - {u_{\tau c}}^2)^{\varphi/2}$ with $\varphi = 3$ in regions where $u_\tau > u_{\tau c}$:

$$P = 0.00033(\frac{{u_\tau}^2 - {u_{\tau c}}^2}{{u_{\tau c}}^2})^{1.5} \frac{(\rho_p/\rho - 1)^{0.6} g^{0.6} d^{0.8}}{\nu^2} \tag{3.13}$$

where P is expressed in units of volumetric flux per unit area and time, ρ is the density of water and ρ_p is the density of the sediment particles of diameter d. In the following simplified analysis one will assume that the flux of sediment entrained from the bed at a certain location is not limited by the presence of a high concentration of entrained particles over that location. This is a standard assumption in previous studies that simulated the transport and deposition of entrained particles carried by gravity and turbidity currents [e.g. *Necker et al.*, 2005]. For a given sediment grain size, the local flux of sediment entrained from the bed calculated using these empirical models is a function of u_τ and $u_{\tau c}$ for clear water scour conditions (I_2 type formulas as the one proposed by *Van Rijn* [1984]). In nondimensional form, the generic expression for the local flux of entrained sediment is:

$$I_2 = \frac{1}{H^2 {u_b}^3} \int\limits_{A', u_\tau > u_{\tau c}} \left({u_\tau}^2 - {u_{\tau c}}^2\right)^{3/2} \mathrm{d}A' \tag{3.14}$$

where A' indicates the area of the inclined channel bottom.

Results in Fig. 3.11 show that the capacity of the ISW to entrain sediment over the sloped boundary is the largest in the collapsing case. Not only that the peak value of I_2 is the largest in the collapsing case, but also the nondimensional time interval over which I_2 assumes relatively large values ($\sim 12T$) is the largest in this case. For all three cases, the sediment entrainment capacity of the current peaks as the maximum downstream acceleration over the inclined surface occurs, immediately before the generation of the instability. Though the peak values of I_2 are comparable in the plunging and surging cases, the peak of I_2 occurs much faster in the surging case and decays fairly rapidly compared to the plunging case.

3.6 Discussion

Using high-resolution numerical simulations, we reproduced three laboratory experiments on internal solitary waves in order to investigate the effects of their interaction with a sloping boundary. The numerical approach allowed us to analyze and quantify three breaking events by linking the different instabilities and dynamics of each breaker wave with the consequent effects within the fluid and over the inclined surface. For the plunging breaker case, an instability develops as the wave feels the presence of the sloping boundary in the form of a clockwise vortex induced by the overturning of the trailing edge of the wave. The instability occurs in the internal part of the flow beneath the wave, relatively far from the bottom with respect to the other cases. Immediately after the edge overturning, a large amount of salty water runs over the wave, inducing a large amount of salty water entrainment into the mixed layer. However, the instantaneous mixing efficiency increases up to about 0.25, maintaining approximately unchanged its value until the turbulent structure dissipates. During these times ($t'/T = 3 \div 8$), the thin layer of salty water is pushed down the incline by the approaching wave, which induces a large amplification of the bed shear stress. As the mixed region starts to interact with the sloped boundary, the distributions of u_τ/u_b become very irregular in the spanwise direction. During this stage, the mixing efficiency increases again, reaching its maximum value as the mixed region reaches the undisturbed pycnocline position. For the collapsing breaker case, before the wave through reaches the sloping surface, it forces the heavier fluid to accelerate downwards in the vicinity of the sloped boundary. At this stage, the normalized bed friction velocity is close to uniform in the spanwise direction and assume its maximum value. Over the incline, the position at which the maximum velocity occurs is expected to move upstream, until the consequent deceleration in the adverse pressure gradient region becomes strong enough to induce the boundary layer separation. From this time, the distributions of u_τ/u_b become non uniform in the spanwise direction. The instability causes the generation of a fresh water bolus characterized by an anticlockwise motion that quickly dissipates, inducing entrainment of salty water into the mixed layer. The vortex dissipation occurs rapidly, thus entrainment and mixing occur in quick succession: the maximum mixing efficiency is observed after the bolus generated by boundary layer separation forms. After the bolus dissipation, the breaker event evolves with the generation of a gravity current forced by the unstable density distribution over the sloping boundary. The gravity current flows upslope inducing entrainment of fresh water into the mixed layer. During this phase, although the entrainment linearly increases, the mixing efficiency evolution shows several peaks of increasing values. This could be probably due to formation of successive KH billows at the interface. As the gravity current flows up to the incline, the maximum bed shear stress values are observed in close proximity of its front, and large-scale 3-D turbulent eddies develop inside the mixed layer. For a surging case, the entire breaking event is very similar to the one observed for the collapsing ISW. The main difference can be found in the energetics of the boundary layer separation instability. Because of a larger Iribarren number is needed, a surging breaker occurs when the sloping boundary is inclined enough compared to the wave slope. Under these circumstances, as the wave approaches the slope, the quick upstream acceleration and deceleration of the heavier fluid close to the inclined surface assume lower values. The consequent boundary layer separation could cause the formation of a smaller bolus. Because case 3 ISW (the surging case) is bigger (i.e. faster) than the one of case 1 (the collapsing case), one could expect stronger instabilities to develop for case 3. Nevertheless, both the qualitative comparison between the bolus size (Fig. 3.2b and Fig. 3.3g) and the quantitave comparison of their effects in terms of mixing efficiency (point B in Fig. 3.7a and point G in Fig. 3.7c), prove that for the surging breaker this instability is relatively less energetic. For these reasons, the gravity current that starts to flow up the sloping boundary is relatively bigger and more energetic for the surging breaker (Fig. 10c) compared to the one observed in the collapsing case (Fig. 3.9b). The normalized bottom shear stress velocities during the propagation of the two currents assume approximately the same values (~ 0.01) even if the boundary is more inclined in the surging case. For the three cases analyzed, although the maximum entrainment values are very different, the bulk mixing efficiency evaluated during the breaking events is similar. The maximum amount of entrainment is observed for the surging breaker case. However, the mixing efficiency does not show any considerable increase and remains comparable to the values predicted in the other two cases. Thus, the surging breaker case is characterized by a lower mixing compared to the other cases. We also investigated the capacity of the ISW to entrain sediments over the sloped boundary. For both the collapsing and the surging case, the largest sediments entrainment capacity is observed as the boundary layer separation develops, immediately before the bolus formation. However, the collapsing case showed the largest values of the entrainment function I_2, confirming that the anticlockwise vortex is more energetic in this case compared to the surging breaker case. Secondary peaks were also observed to occur as the gravity current forms and starts to accelerate. The plunging case showed a capacity to entrain sediments during the breaking event comparable to the surging case in terms of peak values. However, the plunging mechanism is characterized by instabilities that develop mostly in the interior part of the fluid and not in close proximity to the sloped surface. This is the reason why the nondimensional time interval over which I_2 assumes relatively large values is the lowest with respect to the other cases.

Chapter 4

Bedforms generated by solitary waves

Solitary waves play a crucial role in nearshore zones, such that many authors investigated their features in the past [e.g. *Munk and Traylor*, 1947; *Synolakis*, 1987; *Puig et al.*, 2004; *Garrett and Kunze*, 2007]. The main attention was focused on the wave breaking over a sloping boundary, and the consequent mixing and resuspension of bed material [*Kao et al.*, 1985]. The role of solitary waves on sand-wave field formation is a topic of great interest nowadays. *Droghei et al.* [2016] analyzed the bedforms observed off the Messina Strait in order to link their presence to the tidal-induced ISWs action.

The generation of coherent vortices are shed from the separation bubble in the adverse pressure gradient region, is the main resuspension mechanism beneath ISWs [*Aghsaee and Boegman*, 2015]. In order to simulate the same physical process for successive identical waves, taking advantage of the similar unsteady features, surface solitary waves (SSWs) are considered.

This Chapter presents experiments on surface solitary waves interacting with a sandy flat bottom. A series of 15 different cases is considered and for each of them 400 SSWs having the same features are generated. For all cases, after the wave passage, a reverse flow is observed in close approximation with the bottom. However, only for 7 of them bedforms generation occurs. The sand-wave field, composed by asymmetric equal to each other dunes, migrates in the same direction of the waves, increasing in length. The objective of the present study is to investigate the boundary layer instability mechanism beneath SSWs over flat sandy bottom. In particular, I seek to formulate a criterion for predicting the occurrence of unstable flow to re-suspend bed material. For this reason, the experimental apparatus is

properly set up in order to measure the time evolution of both downstream and vertical velocity, and the total pressure, in close proximity to the sandy bottom. For particular values of wave amplitude, wavelength and water depth the sand-wave field forms. Both the horizontal pressure gradient and the downstream velocity acting at the upper edge of the bottom boundary layer affect the triggering process.
Finally, I qualitative evaluate the different effects on the same flat sandy bottom induced by a steady current and by successive identical waves.

This Chapter is organized as follows: Section 4.1 describes the sand-wave field observed off the Messina Strait, Section 4.2 introduces the adopted experimental procedure and facilities; Section 4.3 describes the obtained results: the SSWs and bedforms features, and the bedforms triggering process. Section 4.4 presents the steady flow experiment.

4.1 Bedforms off the Messina Strait

In marine channel, tidal environment and continental shelf/slope, the shear stress caused by the presence of unidirectional strong currents induce the formation of asymmetric sand wave field. However, sand wave field are observed also in marine environments where no such currents exist. Both south and north approaches of the Messina Strait (Mediterranean Sea) are characterized by the presence of sand-wave fields, formed between ~ 200 m and ~ 300 m depth, running along a topographic mound offshore of Capo Rasocolmo. The ~ 7 km wide and ~ 150 m high mound extends for about 10 km along a SW-NE direction. *Selli et al.* [1978] and *Martine and Jean-Pierre* [1988] first report bedforms presence in this region, cover an area of about 3 km^2. The recovered seafloor sampling is composed mostly by sand with a mean grain size of about 0.5 mm [*Santoro et al.*, 2002]. Bedform dimensions tend to increase northward having wavelengths of 60-120 m, amplitudes of 1.5-5 m, and lateral extent of 100-300 m. The presence of those bedforms marks the strong tidal processes affecting this region [*Defant*, 1940]. *Selli et al.* [1978] and *Martine and Jean-Pierre* [1988] suggested that tidal-induced bottom currents could induce bedforms formation. *Santoro et al.* [2002] attributed this bottom current to a combination of tidal, upwelling, and thermohaline effects, and suggested that the migration velocity of the sand waves decreases with increasing depths due to differences in the hydrodynamic forcing. *Droghei et al.* [2016] considered for the first time the role of tidal-induced ISWs in sand-wave field formation. They proposed that ISWs induced by tides can produce a unidirectional boundary current able to induce bedforms generation. They tested this idea by examining the sand-wave field off the Messina Strait, where ISWs are refracted by topography. Numerical simulations and field observations proved that the deflected pattern of the sand-wave field could be due to the refraction of such waves. In this context, the motivation of the study is to experimentally investigate the role of successive ISWs in the bedforms triggering process, in order to define if and what kind of solitary waves can produce sand-wave fields. For this reason, I analyzed the interaction between waves in shallow water conditions with a flat sandy bottom. The generation of a large number of ISWs, without alternating the initial two-layer stratification, represented a difficult and time-consuming challenge. As explained in more detail below, by taking advantage of solitary waves properties, in terms of induced velocity and pressure fields, I opted for generating not internal but surface solitary waves, and analyzing their interaction with a flat sandy bottom.

4.2 Experimental setting and facilities

We performed a series of laboratory experiments at the Saint Anthony Falls Laboratory in Minneapolis, in a 12 m long, 0.15 m wide and 0.5 m deep flume.

Fig. 4.1 shows the initial experimental setting used to generate surface solitary waves, following the standard lock-release method [*Russell*, 1844]. The flume is filled with fresh water ($\rho = 1000$ kg/m^3), producing a uniform layer with a thickness h_0. A vertical movable gate is placed at a distance x_0 from the left lateral wall of the tank, in order to produce a hydraulic discontinuity between the lock region (on the left) and the ambient fluid region (on the right). The 5 mm thick gate is composed by two metal plates separated by a protruding gasket seals, adhering to the bottom and the tank side walls. By adding further fresh water inside the lock region, a displacement η_0 forms between the free surfaces on either side of the gate. Essentially just a quick removal of the gate induces the formation of a single surface solitary wave, propagating towards the ambient fluid region. Once each wave reaches the end of the tank, it would be reflected by the vertical lateral wall. To avoid any possible interaction of the reflected waves with the sandy bottom of the domain of interest, the SSWs reflection is suppressed by loose nets, as wave absorbers, placed at the end of the tank (W.A. in Fig. 4.1).

Along the whole tank, the bottom has a thickness $h_s = 0.02$ m. In the lock region, and up to 2.0 m from the left lateral wall of the tank, the bottom is composed by an iron plate (2.0 m × 0.15 m × 0.02 m). By means of this rigid bed, the hydraulic seal of the gate is ensured, avoiding also that the waves generation mechanism could induce erosion, affecting the successive waves features, for the changing bottom conditions. The ambient fluid region presents natural sand arranged at the bottom (0.45 $\div$ 0.55 mm), producing a 2 cm thick flat inconsistent layer. Fig. 4.2 shows the grain distribution test data I measured by sieve analysis, following the Standard Test Methods for Particle-Size Analysis (ASTM D - 422 63). The following D-values are obtained: $D_{10} = 0.5031$ mm, $D_{50} = 0.6474$ mm, $D_{90} = 0.8173$ mm. The sand specific gravity is SG= 2.67.

We used a high-resolution acoustic Doppler velocimeter (Nortek Vectrino Plus) to measure, with a frequency of 80 Hz and an accuracy of 1 mm/s, 3D water velocity at a fixed distance over the bottom (u along the x axis, v along the y axis and w along z axis). The acoustic sensor has one transmit and four receive transducers. The 7 mm high sampling volume, located 5 cm away from the sensor, is a cylinder with a diameter of 6 mm. The emitter sends out a short acoustic pulse that travels through the focus point for the

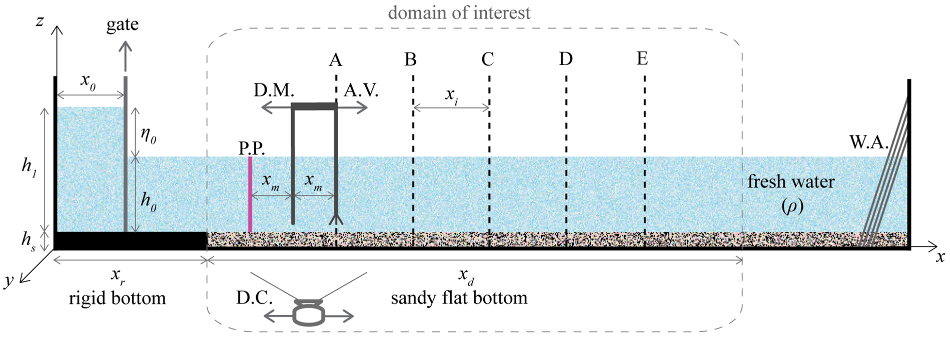

Figure 4.1: Initial experimental set-up for the surface solitary wave generation. The 12 m long, 0.15 m wide and 0.5 m high tank is filled with fresh water ($\rho = 1000$ kg/m^3) to the height h_0. A displacement η_0 is produced between the free surfaces divided by the gate, placed at a distance x_0 from the lateral wall of the flume. The h_s thick bottom is composed by a rigid layer nearby the lock region ($x_r = 2.0$ m), and by natural sand elsewhere. Five millimetres from the bottom, at the midpoint of five equally-spaced cross sections (A-E, $x_i = 1.0$ m), the 3D velocity is measured by using a 3D high-resolution acoustic velocimeter (A.V.), mounted on a movable carrier. Integral therewith, a digital manometer (D.M.) measures the total pressure 5 mm from the bottom at a fixed distance ($x_m = 0.56$ m) from the velocimeter. A digital camera (D.C.), placed 2.0 m from the tank, is used to record each generated wave. Potassium Permanganate (P.P.) is used as tracer to evaluate by image analysis the velocity along a vertical 1 m spaced from the velocity probe. Outside from the domain of interest ($x_d = 9.0$ m), at the end of the tank a wave absorber (W.A.) is placed to avoid waves reflection.

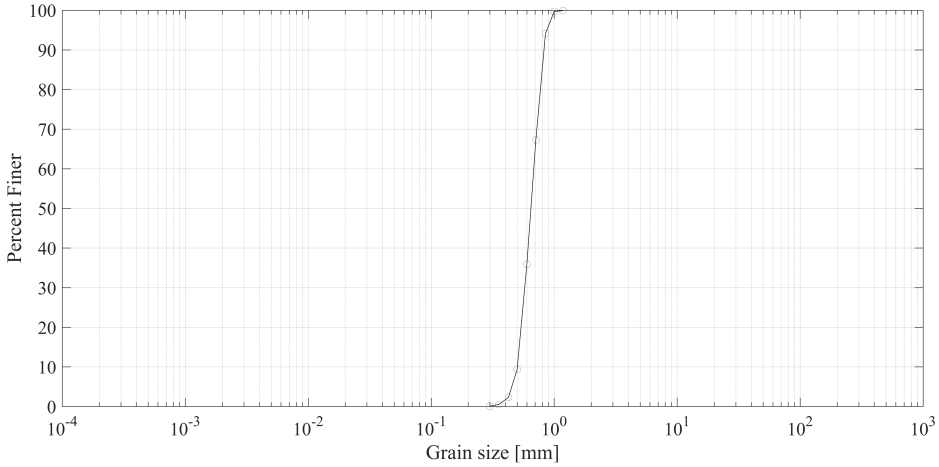

Figure 4.2: Particle size distribution obtained by sieve analysis (ASTM D-422) for the natural sand composing the flat inconsistent bed of the wave tank.

receiver beams, and the echo is firstly recorded in each of the acoustic receiver elements, and then processed to find the Doppler shift. An electronic pressure sensor measures the total pressure, with an accuracy of 1 mm and a frequency of 200 Hz, 5 mm from the bottom. Before each experiment, the total pressure is measured at a fixed depth with the fluid at rest, in order to obtain, as differential, the total pressure during the fluid motion. Both the pressure probe and the velocimeter probe are placed over a movable carrier able to horizontally slide by means of tracks (Fig. 4.1). The fixed distance between the pressure and velocity probes is $x_m = 0.5$ m. Both the 3-D velocity and the total pressure are evaluated at 5 mm from the bottom, at the midpoint of five cross sections (A-E in Fig. 4.1) spaced 1 m from each other, by aligning the velocity probe with each of them.

The wave passage from each measurement section is recorded by a CCD (Charged Coupled Device) camera with a frequency of 60 Hz and a spatial resolution of 1080×1920 pixels. It is located at a fixed distance (2.0 m) from the lateral wall of the tank, so that each pixel has a resolution of about 15 mm (Fig. 4.1). By image analysis, it is possible to evaluate the SSWs main features: the wave amplitude A_w, the wavelength L_w, and celerity c_w (i.e. the first derivative of the crest position). The error committed for lengths measurements is about 1 pixel, thus the celerity values are affected by an error of 0.05 cm/s.

Some potassium permanganate grains (KM_nO_4) are spilled over the free surface, at the midpoint of the tank cross section, 1 m spaced from the velocimeter probe (P.P. in Fig. 4.1). The grains, vertically decanting, release a pink line approximately 0.5 cm wide along the x direction. The motion of the dyed strip is analyzed by image analysis, in order to evaluate the vertical profile of the horizontal velocity component induced be the wave. The not negligible vertical velocity values, mostly at shallow depths, affected the accuracy of this method. Nevertheless, close to the bottom, where the vertical velocities are lower, the image analysis of the dyed strip motion allowed to obtain a measure of the stroke horizontal action induced by the wave passage. The water parcels motion induced by the wave, at 5 mm from the bottom is defined *'stroke length'* (L_{ws}).

A series of 15 experiments are performed(Tab. 4.1). The initial setting parameters are the lock length (x_0), the water depth (h_0), and the free surface displacement (η_0). By varying their values, it is possible to obtain different waves in terms of amplitude (A_w), wavelength (L_w) celerity (c_w), and stroke length (L_{ws}). It was important to make sure that the interaction of each wave with the bottom induced sand particles motion in the same direction of the wave propagation at least (shallow water condition). For each case, 400 successive SSWs with the same features are generated, and their effect on the initially flat sandy bottom are investigated. For 8 cases, the original flat bottom remained unchanged, while, for 7 cases, asymmetric sandy dunes form. Tab. 4.1 shows the values of their amplitude (A_s), and length (L_s). The dunes amplitude is evaluated as the maximum displacement of each dune from the original flat bottom level; while the dunes length is the distance between the crests of two successive dunes.

At a later stage, for each case, in the measurement sections and at 5 mm from the bottom (Fig. 4.1), I evaluated the time evolution of the 3-D velocity, the total pressure, and the surface displacement. For each section, I evaluated all these quantities for three waves with the same features, in order to obtain their averaged representative values.

Case	Initial setting parameters			SSWs Features				Bedforms features	
	x_0 [cm]	η_0 [cm]	h_0 [cm]	A_w [cm]	L_w [cm]	c_w [cm/s]	L_{ws} [cm]	A_s [cm]	L_s [cm]
1	27.0	10.0	10.0	4.8	71.8	106.43	17.2	1.4	9
2	39.0	12.0	12.0	7.6	90.8	117.50	20.7	1.6	10.2
3	39.0	10.0	12.0	6.0	81.8	109.16	18.5	-	-
4	39.0	9.0	11.0	5.7	78.0	110.57	17.0	-	-
5	39.0	13.0	13.0	7.5	98.0	123.80	22.7	1.8	10.5
6	39.0	13.0	14.0	7.5	110.0	127.01	23.0	-	-
7	33.0	13.0	14.0	7.0	100.4	124.10	21.4	2.2	12.5
8	33.0	12.0	12.0	6.3	92.2	113.53	21.2	-	-
9	33.0	10.0	10.0	5.2	69.6	105.12	16.6	-	-
10	33.0	12.0	13.0	6.4	93.0	117.59	19.7	1.8	12
11	25.0	14.0	12.0	6.0	86.7	114.95	20.5	1.8	10.9
12	25.0	10.0	9.5	5.0	70.0	102.97	16.8	1.6	11.1
13	25.0	9.0	9.5	4.1	70.0	99.09	14.8	-	-
14	25.0	13.0	12.0	4.6	96.9	109.84	16.2	-	-
15	27.0	8.0	10.0	4.1	76.2	102.63	14.1	-	-

Table 4.1: The SSWs cases considered in this study in terms of the initial setting parameters (i.e. lock length x_0, free surface displacements η_0, water depth in the ambient fluid region h_0) and the SSWs features (i.e. the wave amplitude A_w, the wavelength L_w, the celerity c_w, the stroke-length L_{ws}). The cases for which the interaction between the initial flat sandy bottom and 400 consecutive waves for each case, induced bedforms generation, present the sandy dunes features (i.e. dunes amplitude A_s and length L_s).

4.3 Results

As a result of the interaction between 400 SSWs and the initially flat sandy bottom, cases for which a sand wave field formed presented some common features. Although the number of successive SSWs that induce the generation of recognizable asymmetric dunes varies from case to case, the firsts bed irregularities are observed to occur after the action of 5-10 SSWs. Moreover, the location of these irregularities along the tank is approximately the same: nearby the measurement section B (Fig. 4.1). For this reason, wave properties are evaluated in such location.

4.3.1 Wave features

SSWs are generated with a range of amplitude $4.1 \div 7.6$ cm and a range of wavelength $69.6 \div 110$ cm. The water volume trapped in the lock region above the water depth h_0, is always larger than the volume of the generated SSWs. Fig. 4.3a shows the relation between those quantities, normalized by the spanwise dimension of the domain (i.e. the tank width). Meanly 30% of the initial volume is lost due to the turbulence induced by the generation mechanism, irrespective of the trapped volume. The phase velocity c_w appears to be linearly related with the wave surface S_w, normalized by the water depth h_0: the relation shows that bigger waves move faster (Fig. 4.3b).
However, the generation of sand wave fields is not directly related with the SSWs size: both larger and smaller waves can produce sandy bedforms (Fig. 4.3b), e.g. case 6 (i.e. the largest generated wave) did not show any dune forming, as well as for case 1 (i.e. one of the smallest waves) bedforms are observed. The possibility for a SSW to produce sandy dunes seems to be not dependent on how large is the velocity transferred at the bottom during the wave passage: the induced shear stress intensity does not affect the bedforms generation mechanism.

Bedforms triggering process must be anyhow affected by geometric and kinematic features of SSWs and the total water depth, over which they propagate. For this reason, I investigated the relation between the maximum surface displacement ($A_w + h_0$) and the wavelength (L_w), both normalized by the undisturbed water depth h_0 (Fig. 4.4). From the analysis of Fig. 4.4, it is possible to notice that for solitary waves that generated bedforms, those quantities show a linear relationship. This prove that for a given water depth, only waves with specific values of amplitude and wavelength induce

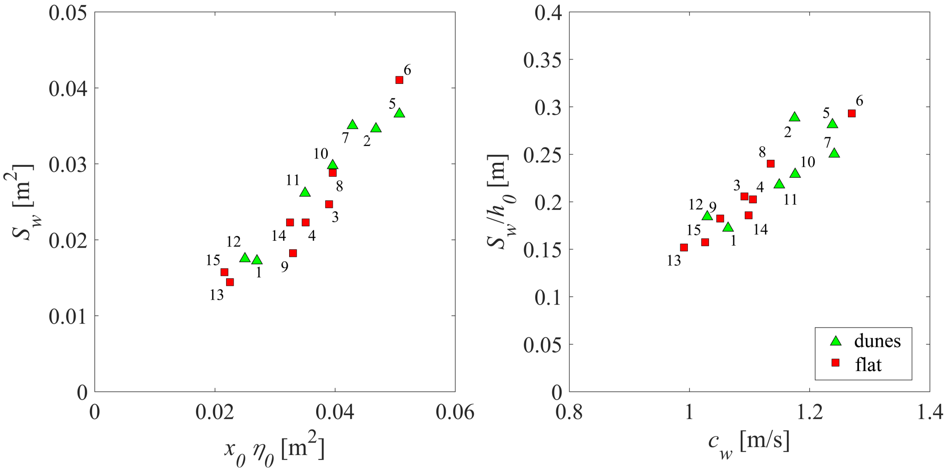

Figure 4.3: Wave features evaluated in Section B. (a) Relation between initial setting parameters (i.e. lock length x_0 and free surfaces displacements η_0) and SSWs surface (S_w). (b) Relation between SSWs celerity (c_w) and SSWs surface. These plots have been obtained following the interaction between 400 SSWs, having the same features, with the initially flat sandy bottom. Green triangles refer to cases for which bedforms formed, red squares refer to cases for which the initial flat bottom remained undisturbed.

the generation of sandy bedforms (Fig. 4.4). Wavelength involves horizontal gradients of velocity and dynamic pressure: for larger waves lower horizontal velocity and dynamic pressure gradients are expected. Otherwise, the wave amplitude affects the hydrostatic pressure and the wave surface/celerity: for waves with larger amplitudes the velocity field presents larger absolute values. All this suggests that, for a better understanding of the triggering process, waves velocity and pressure fields should be investigated, focusing mostly on their time and spatial variations.

4.3.2 Interaction between SSWs and the sandy bottom

By using potassium permanganate as tracer, resulting as a vertical line, it was possible to observe the wave action on the fluid during its propagation (Fig. 4.5a). For all the performed experiments, the velocity field induced by each SSW unevenly shifted forward, as proved from the rigid movement of the dyed vertical line. Fig. 4.5 shows this occurrence for case 5 SSW. Approximately in the upper half of the undisturbed water level, the more the dyed water particles are close to the free surface, the larger is their hor-

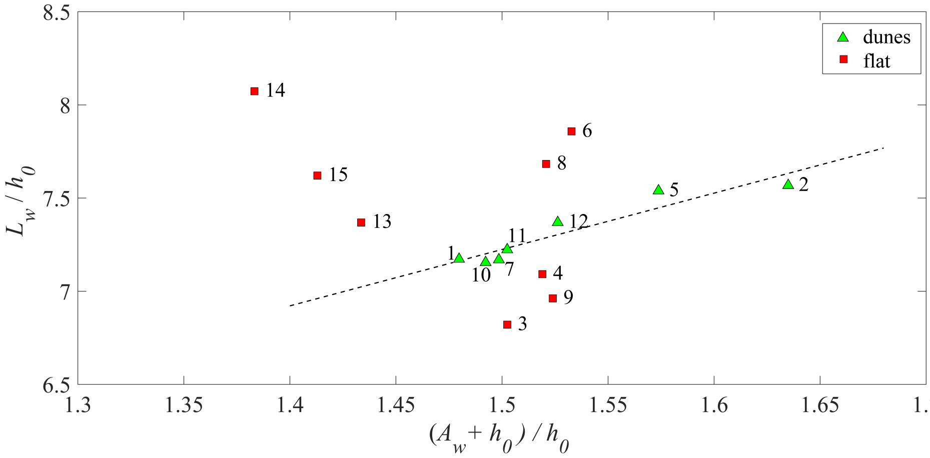

Figure 4.4: Wave features evaluated in Section B. Relation between the maximum surface displacement ($A_w + h_0$) and the SSWs wavelength (L_w), both normalized by using the undisturbed water depth (h_0). This plot has been obtained following the interaction between 400 SSWs, having the same features, with the initially flat sandy bottom. Green triangles refer to cases for which bedforms are observed, red squares refer to cases for which the initial flat bottom remained undisturbed.

izontal displacement (Fig. 4.5d). Moreover, in this region, the stretching of the vertical dyed strip gives proof of not negligible vertical velocity (Figs. 4.5b, c). In the lower half of the vertical profile, the stroke action of the wave evenly shifts forward the water parcels. Here, the dyed strip thickness remains roughly unvaried because of less vertical velocity values. In close proximity to the bottom, after the wave passage, the fluid results displaced along the x-axis (Fig. 4.5a). By image analysis, the stroke length L_{sw} is estimated. Fig. 4.5f shows that the stroke lengths are linearly related with the waves surface, normalized by the undisturbed water level. Also in this case we observed that, for a given h_0, bigger waves transfer larger horizontal velocities at the bottom, not necessarily generating bedforms.

The shear stress induced by the SSWs at the bottom causes sand particles motion in the same direction of the wave. For a given h_0, being the horizontal velocities transferred at the bottom proportional to the wave celerity (i.e. wave volume), the observed stroke motion of the sandy particles is larger for larger waves. Moreover, the stroke velocity transferred at the bottom acts on particles of different size, inducing different effects in terms of transport. The adopted natural sand is composed by particles of different size and color: a larger diameter characterizes the black particles.

The shear stress induced by the wave passage horizontally stratifies the bot-

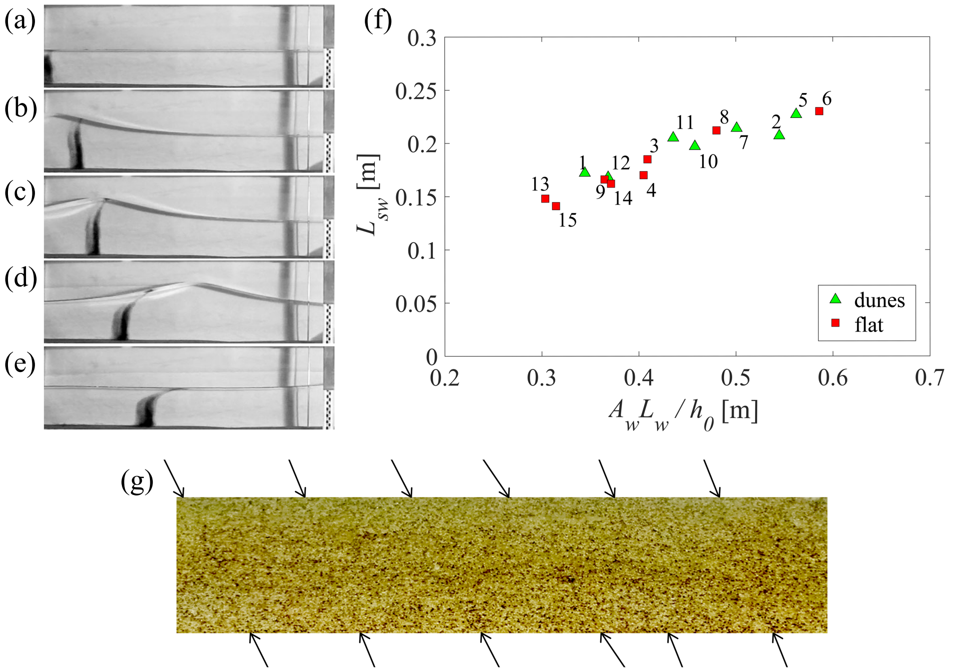

Figure 4.5: Stroke length induced by SSWs. (a-e) Snapshots in time of case 5 in Section B. The wave propagates rightwards and potassium permanganate is used as tracer: undisturbed condition (a), leading edge passage (b), maximum surface displacement over the tracer (c), trailing edge passage (d), tracer at rest after the wave passage (e). Perspective view of the sandy bottom after the passage of 10 SSWs for case 5 (g). The arrows identify the position of the strips. They form perpendicularly with respect to the direction of waves propagation. Relation between the wave features (i.e. wave amplitude A_w, wavelength L_w and undisturbed water depth h_0) and the induced stroke length (L_{ws}), evaluated at 5 mm from the bottom. This plot has been obtained following the interaction between 400 SSWs, having the same features, with the initially flat sandy bottom. Markers are defined as in Fig. 4.3

tom surface, and this effect can be directly observed. In particular, '*strips*' composed by the black particles form, perpendicularly arranged with respect to the direction of wave propagation. Fig. 4.5g shows this occurrence for case 5 SSWs. As the wave propagates, its impulsive action seems to be not uniformly distributed along the domain, rather it appears to act for consecutive '*sand packets*', as if the wave bounced during motion. A possible explanation could be the fact that during particle motion, each sand packet acts as a shield on the sand particles located below it.

For the same case, some dye is arranged at the bottom in order to directly observe the wave action in that region, nearby section B. Fig. 4.6 shows consecutive perspective snapshots, captured during (Fig. 4.6a, b) and after (Fig. 4.6c, d) the wave passage. As expected, the first action of the wave is the motion of the water parcel in the same direction of the wave. After the wave passage a reverse flow occurs, giving rise to anticlockwise vortexes, much smaller than the SSW, that quickly dissipate [*Bogucki and Redekopp*, 1999]. This event occurs overall the domain and for each performed experiments. If the reverse flow velocities are larger than the sand critical shear stress velocity, sand particle upstream motion occurs. In all cases for which a sand wave field formed, this occurrence was observed nearby section B, located at about 4.5 m from the left hand-side lateral wall of the tank. As a SSW generates, it starts to propagate interacting with the mobile bed. This engage causes the wave steepening: the wave tends to increase its amplitude and to decrease its wavelength, while the celerity remains roughly unvaried. This process involves larger horizontal gradients of velocity and dynamic pressure. Once critical values of amplitude and wavelength are reached, the wave broadens, assuming larger wavelength and lower amplitudes. The entire process repeatedly occurs, and it would slowly induce the wave dissipation. Because of the limited domain length, during our experiments, no waves dissipate. During the experiments, the steepening and broadening processes occur, however, the change of the geometric features of the waves during motion are comparable with the error committed in length measurements. When bedforms are observed one supposes that the steepening process occurs nearby section B, where sand particle upstream motion is observed. In the following sections, the broadening process leads the wave to assume different geometric and kinematic features such that the bedforms triggering process cannot occur anymore.

Whenever a sand wave field forms, it's possible to visually distinguish three parts in which the bedforms domain can be divided as follows: a first generation region, the asymmetric dunes zone, and the new generation area (Fig. 4.7c). The first generation region presents the first erosion section: here, the

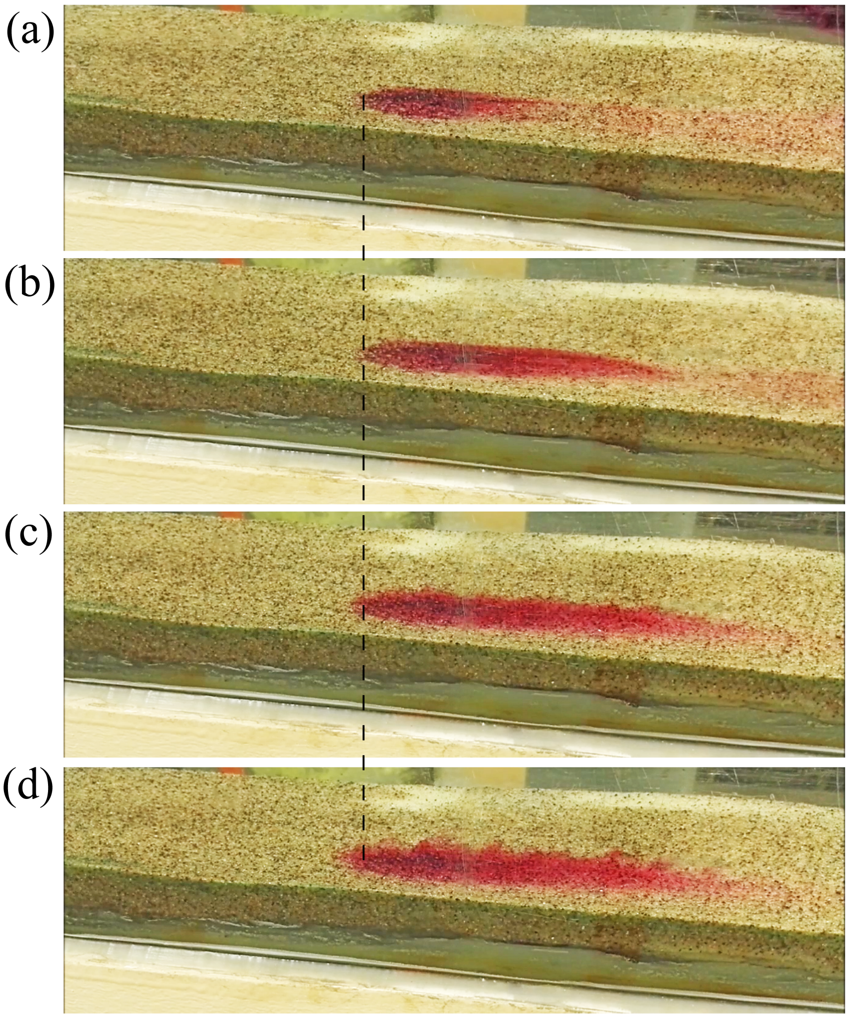

Figure 4.6: Consecutive perspective snapshots captured during the passage of the case 5 SSW over the flat sandy bottom. The dyed region is composed by potassium permanganate. The reverse flow motion is made visible with the help of the dashed line. The undisturbed condition (a); the dyed water parcels move in the same direction of the wave (b), after the wave passage the reverse flow develops (c), resulting in clockwise vortexes that quickly dissipate (d).

interaction between the first successive waves (meanly 5-10 among all cases) and the sandy bottom causes the formation of a localized irregularity of the bottom. The triggering process evolves by means of the action of successive waves interacting with the eroded region: each wave deepens it and the displaced sand particles accumulate upstream, forming a first deposition area. Once the first erosion deposition zone forms, the sand wave field formation started: the following waves continue to generate consecutive alternate erosion and deposition zones. Because of the influence of the lateral wall of the tank, the first generation region presents erosion zones with a facing upstream concavity. This effect decreases as new dunes form as schematized in Fig. 4.7 for case 2. The asymmetric dunes zone is composed by asymmetric dunes having the same geometric features; here the erosion and deposition region develop perpendicularly to the direction of wave propagation. The new generation zone represents the upstream region of the sand wave field. Also in this region the lateral wall of the tank affects the process, forming erosion regions with a facing downstream concavity. As consequence of the successive waves action, the entire sand wave field migrates downstream [*Marin et al.*, 2005].

However, the three zones move with different increasing downstream velocities. For case 2, each wave moves forward the first generation zone and the asymmetric dune region of about 0.08 cm, while the new generation zone moves of about 0.31 cm. The velocity at which new dunes are generated is larger than the migration rate of the entire domain, such that the sand wave field increases its length during migration.

4.3.3 Bedforms triggering process

Bedforms triggering process occurs whenever the shear stress reverse flow velocities, due to boundary layer separation, assume larger values than the sand critical shear stress velocity, inducing a local back motion of sand particles and thus the generation of the first erosion region. The triggering process is explained by the boundary layer theory. From the boundary layer approximation, for a sufficiently high Reynolds number, the flow is divided into an outer region of inviscid flow, and a portion of the domain close to the bottom (the boundary layer), where viscous effects are not negligible. Being u and v the streamwise and vertical velocities respectively inside the boundary layer (with $u >> v$), and μ the kinematic viscosity of the fluid, by using scale analysis, the continuity and Navier-Stokes equations for a two-dimensional steady incompressible flow, reduce to [*Förste*, 1980]:

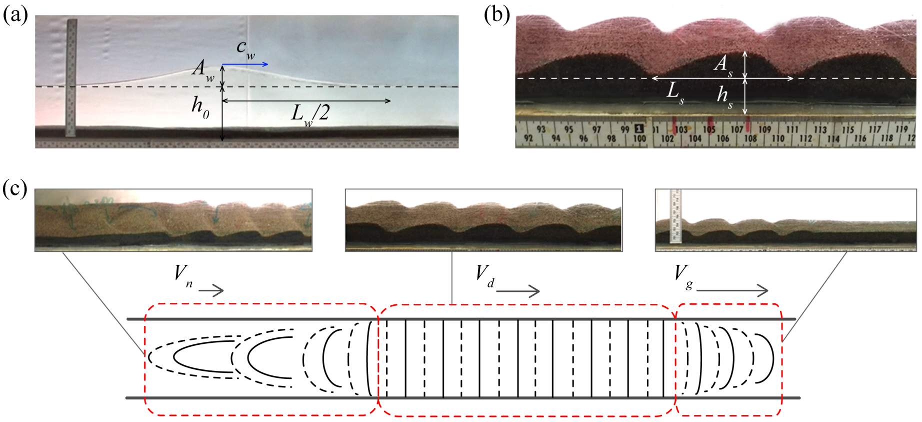

Figure 4.7: Case 2 SSW propagating over the flat sandy bottom (a). Both the geometric/kinematic features of the wave (i.e. wave amplitude A_w, wavelength L_w and celerity c_w) and the undisturbed water depth (h_0) are indicated. Asymmetric dunes generated by the interaction of 400 case 2 SSWs and the sandy bottom(b). Both the geometric features of the dunes (i.e. dune amplitude A_s and wavelength L_s) and the undisturbed sandy layer thickness (h_s) are indicated. Spatial distribution of the final bedforms domain (c), and snapshots of three region that can be identified. In order from left: the first generation zone (migration speed: V_n), the dunes zone (migration speed: V_d), the new generation zone (migration speed: V_g).

$$u\frac{\partial u}{\partial x} + v\frac{\partial u}{\partial y} = -\frac{1}{\rho}\frac{\partial p}{\partial x} + \mu\frac{\partial^2 u}{\partial y^2} \tag{4.1}$$

$$\frac{1}{\rho}\frac{\partial p}{\partial x} \simeq \mu\frac{\partial^2 u}{\partial y^2} \tag{4.2}$$

Flow separation occurs when the boundary layer travels far enough against an adverse pressure gradient region, such that the horizontal velocity inside the boundary layer is almost null. The point where the shear stress is zero is the separation point between the the forward and backward flow. Starting from the separation point, the boundary layer suddenly thickens being forced off by the reversed flow at the bottom: the flow detaches from the bottom and takes the form of eddies and vortices [*Wilkox*, 2010]. Scketch of Fig. 4.8a shows the reverse flow induced by the presence of an adverse pressure gradient imposed on the boundary layer by the outer potential flow. From Eq. 4.1, by neglecting the advective terms Eq. 4.2 is obtained. This shows that the adverse pressure gradient induces the velocity u to decrease along y. If the adverse pressure gradient is strong enough, the second derivative in Eq. 4.1 forces the u velocities to assume negative values, thus inducing reverse flow.

We investigated the reverse flow that induces boundary layer separation, as produced by SSWs, in order to define the bedforms generation conditions. Our analysis can be can generalized also to the case of ISWs, because of the same physical processes involved. Under the hydrostatic hypothesis, indeed, both ISWs and SSWs present an adverse pressure gradient region below the trailing edge (Figs. 4.8b, c). In those regions, the direction of the pressure gradient is opposite to the direction of the flow above the boundary layer. The horizontal velocity acting at the upper edge of the boundary layer is evaluated (u_p). For an ISW, below the maximum displacement of the pycnocline, down to the bottom, the velocity field is exactly specular to the one induced by a SSW [*Lamb*, 1997]. The water parcel motion, thus, will occur in the same direction of wave propagation for a SSW, and in the opposite direction for an ISW [*Hsu et al.*, 2012]. Moreover, the velocity field induced by an ISW of depression shows that the horizontal wave-induced velocity is maximum beneath the wave trough, and it assumes a zero value behind the wave. Hence, a decelerating adverse pressure gradient region underneath the rear half of the wave always occurs [*Aghsaee et al.*, 2012].

As herein shown and described, for the generated SSWs, the hydrostatic assumption is not correct, because of the peculiar velocity field induced by a solitary wave: both vertical and horizontal velocities affect the total pressure

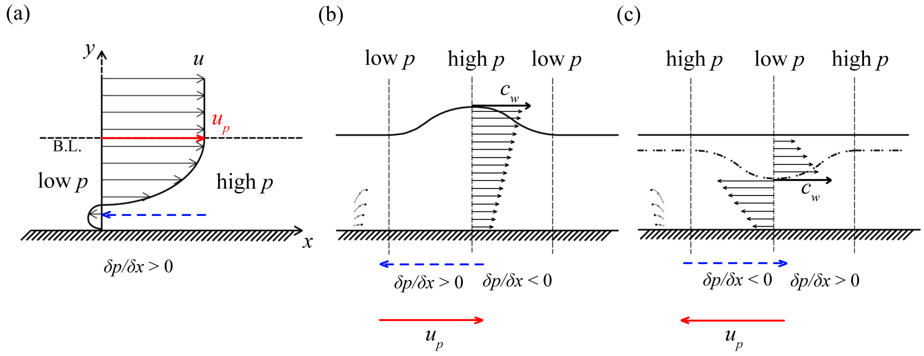

Figure 4.8: Scheme of the boundary layer horizontal velocity profile in presence of a horizontal adverse pressure gradient (a). A reverse flow occurs close to the bottom. Location of the adverse pressure gradient region for a SSW (b) and for an ISW (c) under the hypothesis of hydrostatic conditions; the solid lines refer to the free surfaces, while the dash dot line schematizes the pycnocline position. The induced water parcels path is schematized by successive increasingly dark dots. In both cases, an adverse pressure gradient region is expected below the trailing edge of the wave. The solid arrows refer to the horizontal velocities u induced by each wave, along the vertical profile passing through the maximum surface/pycnocline displacement. The dashed arrows refer to the action of the adverse pressure gradient on the horizontal velocity profile, into the boundary layer.

field. Nevertheless, the total pressure and free surface level time evolution show the same trend for a SSW, such that an adverse pressure gradient region forms.

In section B (Fig. 4.1) the bedforms triggering process has been observed: in this region, for each case and at 5 mm from the bottom, the space/time evolution of the streamwise and vertical velocities and the total pressure are measured. The free surface evolution was obtained by image analysis. Fig 4.9 shows the obtained results both for a case in which the initially flat bottom remained undisturbed (i.e. case 6, Fig. 4.9a), and for a case in which bedforms are observed (i.e. case 10, Fig. 4.9b). The distance of 5 mm from the sandy bottom is low enough to approximate the measured velocity/pressure to the values they assume at the upper edge of the boundary layer. The digital manometer and the 3-D acoustic velocimeter are placed in different sections along the tank (Fig. 4.1). The temporal evolution of the measured quantities is thus aligned by considering as time zero the instant at which the horizontal velocities start to assume positive values. In both cases, the horizontal velocities start to increase when the undisturbed free surface level begins to increase, because of the incoming wave.

However, the rate of increase of the free surface level is larger compared with the rate of increase of the total pressure. This is due to the presence of increasing upward vertical velocities that induce a negative dynamic pressure. For this reason, once the maximum surface displacement occurs, the total pressure is lower compared with the hydrostatic pressure. The maximum vertical velocity at the bottom occurs when the free surface displacement reaches the maximum value. During the decrease of the free surface level the total pressure continues to increase, initially with the same rate, and after faster(for $t > 0.4$ s). This change is due to the combined action of decreasing vertical velocities and increasing horizontal velocities, which causes the total pressure raise (Fig. 4.9a, b). The maximum total pressure results affected mostly on the horizontal velocities, because of abating of both the vertical velocity and surface displacement. Approximately for $t > 0.6$ s, the total pressure time evolution is exclusively affected by its dynamic component, being the free surface displacement equal to zero. Now, the increasing vertical downward velocity is contrasted by the decreasing horizontal velocities. The latter prevails, inducing a decrease of the total pressure.

After the wave passage, thus, the velocity field affected the total pressure field only: the horizontal adverse pressure gradient acts on the velocity field from which it has been generated. The wave geometric features, and the undisturbed water depth are expected to affect the horizontal gradients of the variables involved in the process (i.e. total pressure and horizontal ve-

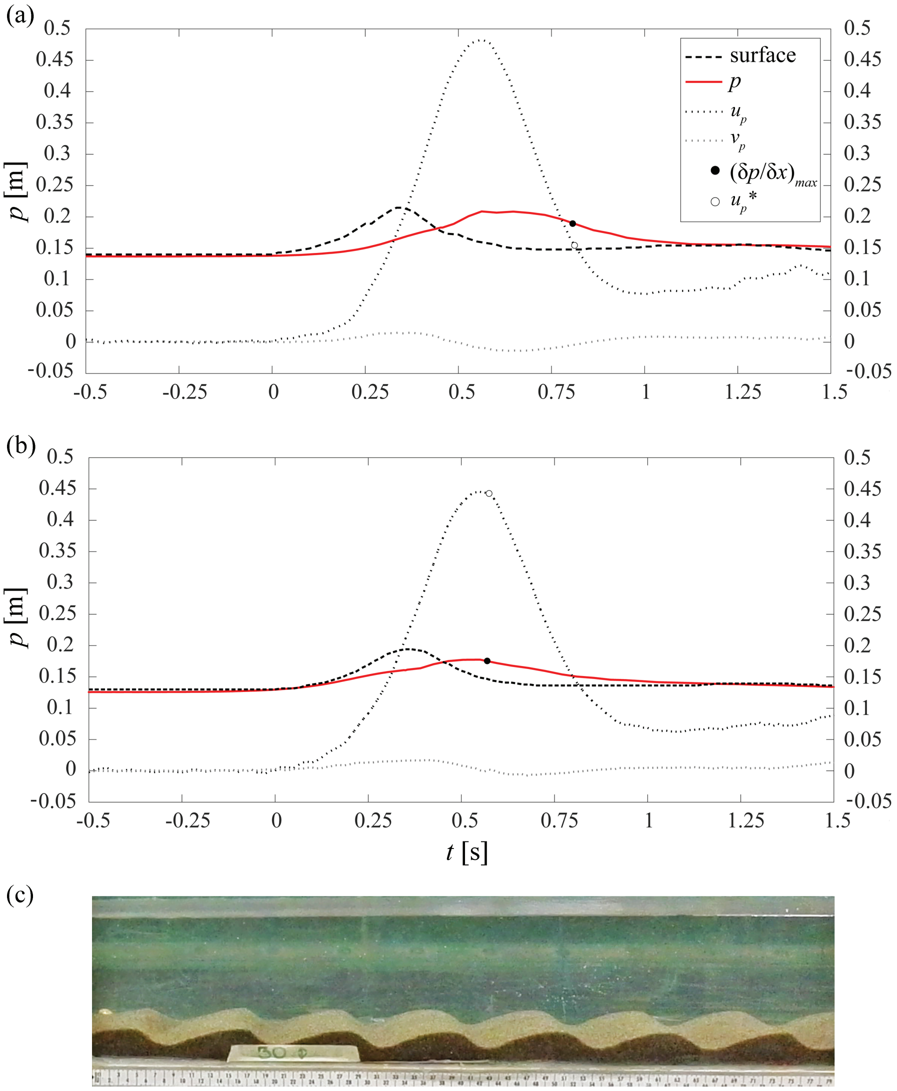

Figure 4.9: Free surface level, total pressure (p) and 2D velocity (u, v) time evolution (a) for a wave not able to generate bedforms - case 6 - and (b) for a wave able to induce bedforms (c) - case 10. Pressure and velocity values have been measured 5 mm from the bottom. Solid dots refer to the time at which the maximum value of the horizontal pressure gradient occurs, empty dots refer to the corresponding horizontal velocity.

locity). The wave surface and the water level affect the velocity values at the bottom: larger velocities are expected for bigger waves and lower water depth. For a given water level, larger waves have lower horizontal velocity gradients, so they need to propagate with larger amplitudes in order to induce velocity/pressure gradients strong enough to cause the development of a reverse flow. Conversely, waves with small amplitudes need lower wavelengths to trigger the bedforms generation, such that short and steep waves facilitate the process. Thus, the reverse flow takes place much more easily as much as the hydrodynamic process assumes an unsteady behavior.

For the performed experiments, I evaluated the maximum horizontal adverse pressure gradient $(\partial p/\partial x)_{max}$ and the horizontal velocity (u_p^*) simultaneously acting at the upper edge of the boundary layer (Tab. 4.2). Waves able to generate bedforms show a different behavior with respect to the others; by comparing Fig. 4.9 and Fig. 4.9b, it's possible to notice a different time delay (t_D) between the occurrences of the maximum horizontal velocity and the maximum adverse pressure gradient. I investigate the relation between this time and the normalized effective pressure, defined as:

$$t_P = \frac{\Delta P_{max}}{\rho u_{max}} \qquad [s] \tag{4.3}$$

where u_{max} is the maximum horizontal velocity at 5 mm from the bottom and ΔP_{max} is the effective total pressure induced by the velocity. In Eq. 4.3, ΔP_{max} is obtained as the difference between the maximum and the minimum total pressure; the latter is the hydrostatic pressure acting at 5 mm from the bottom before the wave passage.

Fig. 4.10 shows the relation between the normalized effective pressure and the time delay t_D. If the normalized effective pressure assumes low values, the bedforms triggering process takes place only if the maximum horizontal pressure gradient occurs immediately after the occurrence of the maximum velocity at the bottom. For these reasons, the more the wave is small (i.e. slow), the more it must be steep in order to induce stronger reverse flow.

I investigated the relation between the maximum horizontal adverse pressure gradient $(\partial p/\partial x)_{max}$ and the horizontal velocity (u_p^*) simultaneously acting at the upper edge of the boundary layer (Fig. 4.11). For low u_p^*, not even for largest maximum horizontal adverse pressure gradients sand particle back-motion occurs. The domain of existence of bedforms is defined for larger values of both variables. This could be surprising, if one does not consider the effect of the horizontal velocity on the adverse pressure gradient. Following Eq. 4.1, indeed, for larger horizontal velocities acting at the upper edge of the boundary layer, stronger reverse flow occurs.

Case	$u_{p\ max}$ [m/s]	p_{max} [m]	u_p^* [m/s]	$\left(\frac{\partial p}{\partial x}\right)_{max}$	t_D [s]	t_P [s]
1	0.424	0.138	0.339	0.136	0.088	8.84E-05
2	0.463	0.186	0.320	0.171	0.125	1.42E-04
3	0.436	0.155	0.176	0.181	0.213	8.02E-05
4	0.419	0.129	0.278	0.137	0.113	1.06E-04
5	0.481	0.199	0.310	0.243	0.130	1.44E-04
6	0.483	0.209	0.154	0.205	0.258	1.42E-04
7	0.458	0.208	0.376	0.260	0.100	1.49E-04
8	0.438	0.164	0.278	0.153	0.138	1.01E-04
9	0.475	0.137	0.292	0.105	0.113	7.79E-05
10	0.445	0.168	0.433	0.121	0.040	8.52E-05
11	0.563	0.172	0.414	0.184	0.050	9.23E-05
12	0.399	0.131	0.296	0.141	0.088	8.89E-05
13	0.350	0.121	0.199	0.107	0.150	7.45E-05
14	0.355	0.166	0.129	0.144	0.260	1.30E-04
15	0.343	0.125	0.252	0.073	0.113	7.32E-05

Table 4.2: Effects on pressure and velocity induced by SSWs passage. Maximum horizontal velocity measured at 5 mm from the bottom ($u_{p\ max}$); maximum total pressure (p_{max}); maximum horizontal adverse pressure gradient ($(\partial p/\partial x)_{max}$); velocity at 5 mm from the bottom when the maximum horizontal pressure gradient is acting (u_p^*); time delay between the maximum velocity and the maximum horizontal pressure gradient (t_D); normalized effective pressure (t_P).

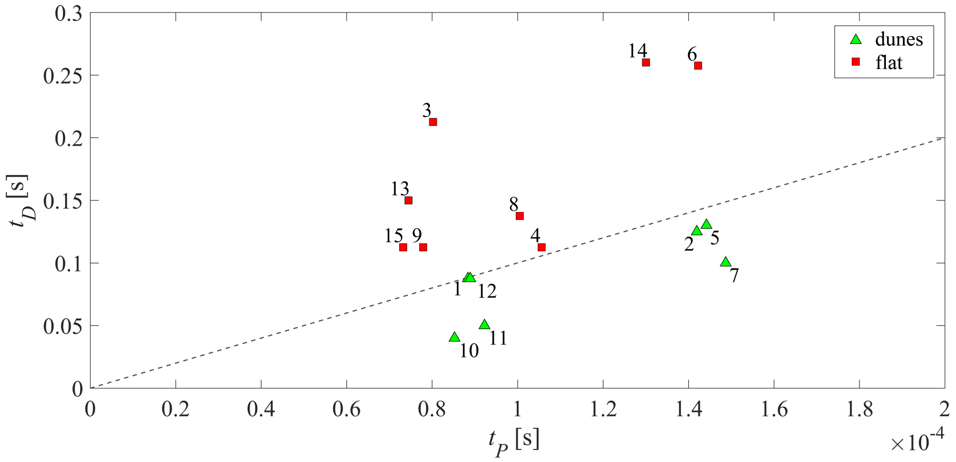

Figure 4.10: Bedforms generation condition: t_P is the time delay between the occurrence of the maximum horizontal velocity and the maximum horizontal pressure gradient; t_P is the time obtained as the ratio between the effective total pressure p_e, and the water density ρ times the maximum horizontal velocity u_{max}.

Being the wave geometric features linked to their effects at the sandy bottom, the wave amplitude, the wavelength and the total water depth are related to the main variables involving the triggering process. Fig. 4.12 shows the relation between wave features and effects at the bottom: the x-axis presents the product of the maximum horizontal adverse pressure gradient and the horizontal velocity u_p^*, normalized by the maximum velocity the horizontal velocity u_{max}; the y-axis presents the ratio between the maximum surface displacement $(A_w + h_0)$ and the SSWs wavelength (L_w). The bedforms domain is clearly identified: only if $(A_w + h_0)/L_w$ assumes values approximately equal to 0.21 the bedforms generation mechanism can take place. However, at the same time, both the horizontal pressure gradient and the horizontal velocity acting on the upper edge of the boundary layer should be strong enough.

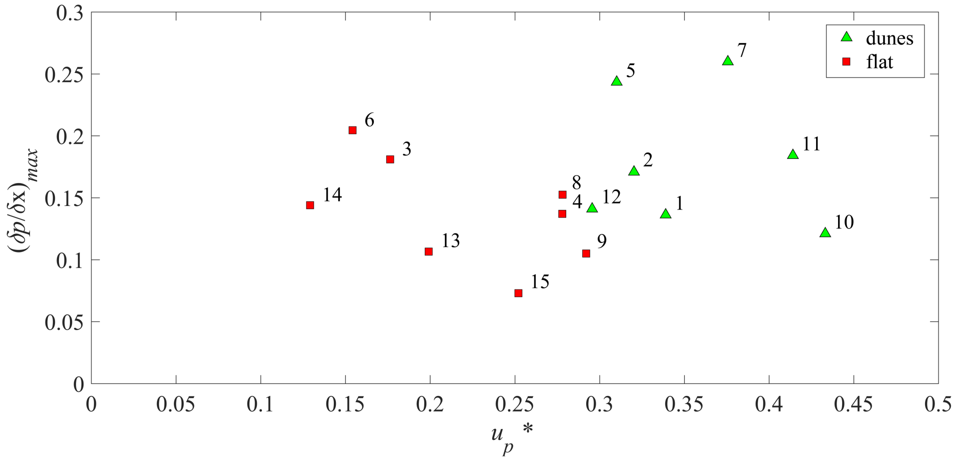

Figure 4.11: Relation between the maximum horizontal pressure gradient and the horizontal velocity up measured at the time of its occurrence (a). Relation between up and the first term of the streamwise momentum equation, evaluated at the upper edge of the boundary layer (b).

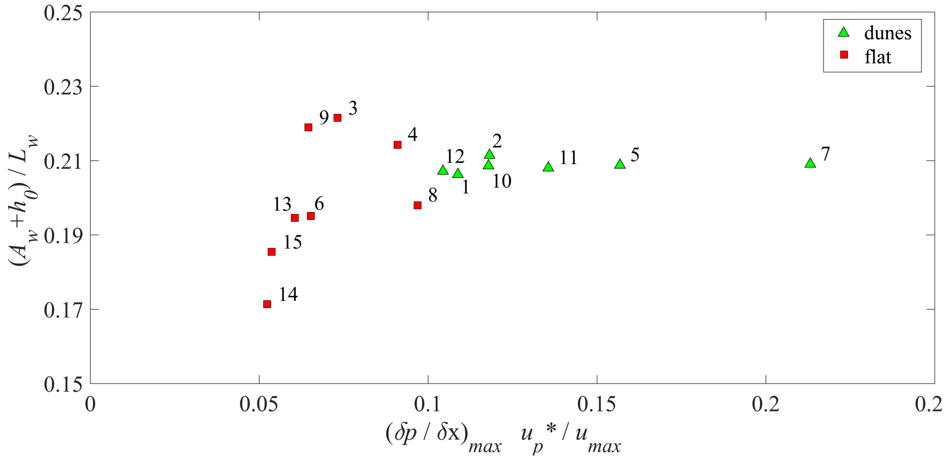

Figure 4.12: Bedforms generation condition. Relation between the wave features (i.e. wave amplitude A_w, wavelength L_w and undisturbed water depth h_0) and the terms affecting the bedforms triggering process, evaluated 5 mm from the bottom (i.e. the maximum horizontal pressure gradient $(\partial p/\partial x)_{max}$, and the horizontal velocity u_p measured at the time it occurs, and the maximum horizontal velocity u_{max}.

4.4 Steady flow experiments

Asymmetric sand waves are typically observed in coastal marine environments exposed to strong currents, where they are formed by current shear resulting from a dominant unidirectional flow. Solitary waves and steady currents induced different action over a sandy bottom. By using the same sand adopted for the SSW experiments, the effects of the interaction of an initially flat sandy bottom and a uniform constant flow are investigated .
The experiment is performed in a 3 m long, 0.15 m wide and 0.5 m deep tank at the Saint Anthony Falls Laboratory (Fig. 4.13). A 0.05 m thick layer of sand composes the bottom. A hydraulic pump placed on the left hand-side of the tank generates a uniform discharge. By properly regulate the upstream and downstream gates level it was possible to obtain a uniform flow characterized by an approximately constant water surface level. A rigid bottom 0.05 m thick is placed next to the inlet, in order to avoid that at this location any irregularity of the bottom took place. The first 0.3 m of the sandy bed present several stones in order to lessen the passage from a rigid to a mobile bed. The high-resolution acoustic 3-D velocimeter is located over the rigid bottom to measure at 5 mm from it the velocity field induced by the flow. The bed was initially covered by a rigid lid until the measured horizontal velocity assumed wanted values. After, it was displaced downstream and I started to record the change in bottom profile induced by the uniform flow. The experiment was recorded by the CCD camera used for the SSWs cases. The flow, travelling along the tank, reaches the outlet which leads to an underlying tank, from which the hydraulic pump draws off the water.

A uniform velocity at 5 mm from the bottom is imposed equal to the maximum velocity measured at the same depth for case 6 SSW. Fig. 4.14 shows consecutive snapshots of the experiment which last 600 s. Each case 6 SSW acted for 1 second, so it is possible to assume that each second of the steady experiment corresponds to the action of an equivalent wave. Fig. 4.14 shows the bedforms induced by the steady flow after 360 s. The comparison with Fig. 4.9c clearly stresses the different effects at the bottom induced by the two flows. The sandy bed profile starts to modify its profile as soon as the flow interacts with it and the triggering process appears widespread along the entire domain. Bedforms induced by steady flow are better defined as ripples: they are composed by consecutive steps that change their length during motion becoming longer and longer over time. Between two consecutive ripples, no erosion zones form, but stagnation regions, in which clockwise vortexes induced a wildly sand particle motion.

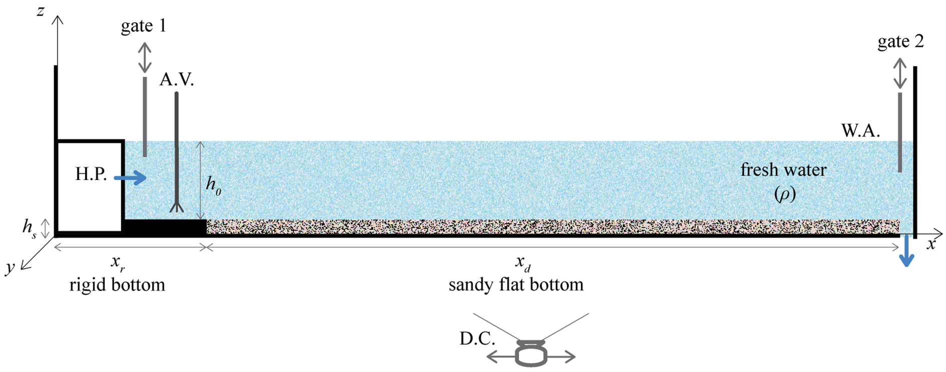

Figure 4.13: Initial experimental set-up for the steady case experiment. The 3 m long, 0.15 m wide and 0.5 m deep tank is filled with fresh water ($\rho = 1$ g/cm^3) up to the height h_0. A hydraulic pump (H.P.) generates a uniform steady flow. Integral with the tank, a high resolution acoustic velocimeter (A.V.) measures 3-D velocity at 5 mm from a h_s thick rigid bottom. Natural sand composed the 2.5 m long, 0.05 m thick mobile bed. Two gates are placed at the tank ends in order to regulate the flow. A digital camera (D.C.), placed 2.0 m from the tank, is used to record the bottom profile time evolution.

The bedforms mechanism is localized in the case of a SSW. Otherwise, it appears widespread along the entire domain for a steady current. The induced bedforms are very different as well: in one case asymmetric dunes having the same geometric features form, in the other case unstable ripples generate. The bedforms triggering process for a steady current depends exclusively on the shear stress velocity induced at the bottom. A SSW inducing a bottom shear stress larger than the critical value, can also not produce any bedform. For a given free surface level, only for particular values of wavelength and amplitude, the necessary conditions for a strong enough reverse flow can occur, the more efficiently the more the hydrodynamic process assumes an unsteady behavior.

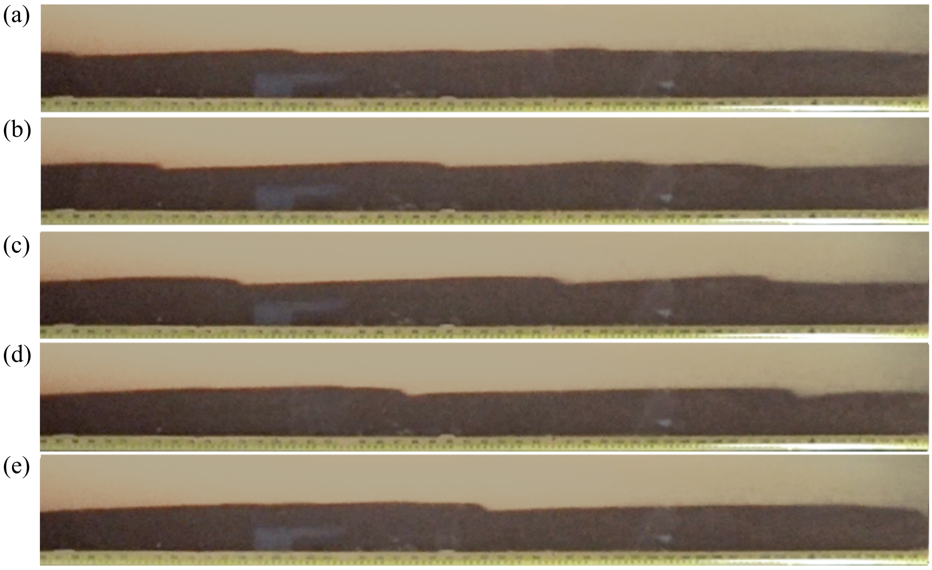

Figure 4.14: Sandy bottom profile evolution caused by a uniform constant flow. Images have been captured at a fixed time from the initial flat bottom condition: (a) 120 s, (b) 240 s, (c) 360 s, (d) 480 s, (e) 600 s. The horizontal velocity 5 mm from the bottom is imposed equal to the maximum horizontal velocity measured at the same depth for the case 6 SSW.

Chapter 5

Conclusions

Shallow water large amplitude surface waves are generally classified as solitary waves, in homage to the first reported single hump-shaped surface wave generated by a towed barge on the River Severn [*Russell*, 1844]. Internal solitary waves are manifest as large amplitude sinusoidal undulations of the pycnocline, the portion of the water column separating a surface layer from relatively more dense underlying fluid. The interaction between the wave and the bottom boundary have a significant effect on both mixing and the benthic dynamics. In the present thesis, the shoaling and the breaking of internal solitary waves in a shallow upper layer as they approach a constant bottom slope is examined through laboratory experiments and numerical simulations. Moreover, the role of the solitary waves in bedforms generation is experimentally investigated.

By following the theoretical/numerical approach it was possible to define the ISWs characteristic wavelength λ. Empirical relations between the experimental initial setting parameters and the generated ISWs kinematic and geometric main features are developed and used to obtain a well-defined wave in terms of amplitude, characteristic wavelength and celerity. The empirical relations show that the amplitude of the generated wave depends on the aspect ratio of the generating volume confined in the lock region before the gate removal. Moreover, the generating volume strongly influences both the value of the characteristic wavelength, and the wave speed.

The interaction between ISWs and a sloping boundary is analyzed. The shoaling processes and breaking events were experimentally and numerically investigated. A LES numerical model is validated by experimental data. The simulated instantaneous velocity and density field are obtained for three different breaking waves, in order to evaluate the effects of the breaking in terms of mixing efficiency and mixed layer volume-integrated bulk entrainment parameter. When a solitary wave of depression shoals over a sloping boundary, the different breaking mechanisms that could develop depend directly on the main processes involved during the shoaling. The steepening of the trailing edge of the wave and the downward motion of the dense fluid confined between the leading edge and the sloping boundary occur. These events develop differently depending on the wave geometric characteristics and on the topographic features. The dynamics of the shoaling waves are characterized by the Iribarren number (Ir) which measures the ratio of the topographic slope to the square root of the characteristic wave slope.

Plunging breakers are observed for $Ir < 1$. During the shoaling, the observed predominant event is the decrease of the trailing edge slope. At about half of the total shoaling time, the leeward steepening process undergoes a sharp increase, resulting in the overturning of the trailing edge. The instability develop within the body of the fluid, at the interface between the two fluids of different density, where the overturning causes the formation of a downstream migrating clockwise vortex. Consequently a large amount of salty water entrainment into the mixed layer occur. However, the trend of the instantaneous mixing efficiency shows that the turbulent mixing does not occur immediately, but only at following times. The marked delay in time between the entrainment and the consequent mixing, suggests that the global instability whirling motion is not energetic enough to immediately mix the two fluid entrained into the mixed layer. The decrease of the lower layer fluid confined between the wave and the sloping boundary characterizes the collapsing mechanism ($1 < Ir < 1.5$). Shortly before the end of the shoaling, this process becomes prominent, and causes instabilities at the bottom. Leaving its original location, the confined fluid accelerates and then strongly decelerates in the adverse pressure gradient region. Boundary layer separation occurs, generating a separation bubble characterized by an anticlockwise motion. The maximum mixing efficiency occurs when the bolus forms and entrains salty water. The anticlockwise vortex dissipates rapidly and then entrainment and mixing occur in quick succession. As collapsing-plunging breakers ($Ir = 1$) shoal over the sloping boundary, the decrease of the trapped dense volume steadily occurs while a strong rear edge overturning takes place only in the second half of the process. Both the events cause instabilities giving rise to a large amount of mixing.

For surging breakers ($Ir > 1.5$) only a small amount of mixing occurs during the propagation of the interface upslope as a gravity current. In this case, the largest amount of the confined dense water flows offshore trough a surface not large enough to induce the boundary layer separation. The max-

imum mixing efficiency occurs when the nose of the gravity current reaches its hightest position over the slope. The gravity current stops and the salty water immediately interacts and mixes with the surrounding lighter fluid. For the three simulated cases, although the maximum entrainment values are very different, the bulk mixing efficiency evaluated during the breaking events, assumes approximately similar values. The surging case shows the maximum amount of entrainment; nevertheless, the mixing efficiency does not show any considerable increase and remains comparable to the other breaking mechanisms. For this reason, it shows a lower mixing than expected, compared to the other cases.
We also investigated the capacity of the ISW to entrain sediments over the sloped boundary. For both the collapsing and the surging case, the largest sediments entrainment capacity is observed as the boundary layer separation develops, immediately before the bolus formation. However, the collapsing case showed the largest values of the entrainment function I_2, confirming that the anticlockwise vortex is more energetic in this case compared to the surging breaker case. Secondary peaks were also observed to occur as the gravity current forms and starts to accelerate. The plunging case showed a capacity to entrain sediments during the breaking event comparable to the surging case in terms of peak values. However, the plunging mechanism is characterized by instabilities that develop mostly in the interior part of the fluid and not in close proximity to the sloped surface. This is the reason why the nondimensional time interval over which I_2 assumes relatively large values is the lowest with respect to the other cases.

ISWs propagating toward the North of the Messina Strait are studied. These waves and topographic features suggest that plunging breakers occur in this region ($Ir = 0.24$). Seven runs are carried out in order to reproduce the real field case with idealized small-scale experiments. The effect of the breaking is evaluated in terms of increase of the pycnocline thickness induced by the consequent mixing. Both the wave reflection and the breaking locations result to affect the horizontal distribution of the increase of the pycnocline thickness induced by the breaking. The ratio between the dimensionless increase of the pycnocline thickness and the wave slope is evaluated. This parameter shows a trend strongly related with the Iribarren number: it increases as Ir increases; then it collapses when Ir tends to the collapsing domain. For $Ir < 0.35$ the performed experiments show an approximately linear relation between Ir and the dimensionless mixed depth: one may infer that breaking mechanisms that occur in the North of the Messina Strait should generate an increase of the pycnocline thickness of $0.5 \div 1\%$. However, only the plunging regime is investigated. For collapsing breakers one may expect a similar behavior concerning with the relation between the Iribarren number and the pycnocline thickness. When the shoaling develops simultaneous instabilities, as for collapsing-plunging breakers, a more complicated trend is expected. It depends on the relative contribution of the two main shoaling processes. An increase of the Reynolds number (as for real-field conditions) would reduce the effect of boundary layer separation on wave breaking [*Aghsaee et al.*, 2010], bring the system towards the plunging for the same internal Iribarren number.

Off the Messina Strait, widespread all over the sloping bottom subaqueous, asymmetric sand waves are present. The interaction of periodic ISWs with the bottom may not only re-suspend, but it also generates bedforms. Intrigued by this occurrence, a series of *ad hoc* experiments are performed. In particular, the effects of the interaction between successive surface solitary waves with an initially flat sandy bottom is investigated. The propagation of ISWs and SSWs over an inconsistent bottom induces the same instability in the bottom boundary layer. In both cases, immediately after the wave transition, the reverse flow caused by the deceleration occurring in the adverse pressure gradient region occurs. By varying wave features (i.e. wave amplitude A_w and wavelength L_w) and free surface levels (h_0), 15 cases are considered. Being in shallow water conditions, the stroke action characterizing each generated wave, always caused downstream sand particle motion. However, bedforms generation occurred only for 7 cases. The wave surface and celerity did not affect the bedforms triggering process: for a given water depth, bigger waves move faster, inducing larger shear stress velocity at the bottom, and, consequently, larger downstream horizontal shift of the sand particles. Nevertheless, the bigger generated wave did not induce any sandy bedform (case 6). In close proximity to the bottom, approximately $4.5m$ from the left end wall of the tank, and at the midpoint of the cross section, we measured the time and space evolution of both the 3-D velocity and the total pressure induced by the wave transition. By image analysis, we evaluated the time and space evolution of the surface displacement. Results shows that during the passage of the leading edge of the wave the total pressure induced close to the bottom is strongly affected by its dynamic component: the upward increasing vertical velocities induce negative dynamic pressure. After the wave crest passage, we noted the simultaneous occurrence of the maximum values of total pressure and horizontal velocity. The effect of the trailing edge over the sandy bottom are exclusively affected by the induced velocity field: the free surface reaches its undisturbed condition and hydrostatic pressure vanishes. An adverse pressure gradient region forms causing reverse flow and, consequently, boundary layer separation. If the reverse flow is strong enough, reaching the sand critical shear stress velocity, a back motion of the sand particles occurs. Waves able to produce bedforms showed a lower delay in time between the occurrence of the maximum horizontal velocity and the maximum adverse pressure gradient. The reverse flow, indeed, is affected on both the pressure gradient and on the horizontal velocity simultaneously acting at the upper edge of the boundary layer (u_p^*), as stated by the boundary layer streamwise momentum equation. For this reason, the relation between u_p^* and $\partial p/\partial x$ is investigated: only waves for which their product is larger enough induce the triggering process, and that their values depend on both wave features and the total water level. In particular, the wave surface and the free surface undisturbed depth affect the velocity induced at the bottom: larger velocities are expected for bigger waves and lower water depth. However, waves with large wavelengths are characterized by lower horizontal velocity gradients, so they can induce stronger reverse flow only if they propagate with larger amplitudes. Steeper waves induce larger velocity/pressure gradients, involving stronger reverse flow. Conversely, waves with small amplitudes need lower wavelengths to trigger the bedforms generation, such that short and steep waves facilitate the process. Thus, the reverse flow takes place much more easily as much as the hydrodynamic process assumes an unsteady behavior. A uniform steady current can be imagined as a wave with infinitesimal amplitude and infinite wavelength. If a steady flow induces bedforms generation, the expected triggering process is very different from the one observed in the case of SSWs. We performed a comparison between the effects over an initially flat sandy bottom of a SSW and a steady flow. We imposed that close to the bottom the horizontal velocity of the current was equal to the maximum horizontal velocity measured at the same depth in the case of a SSW. The bedforms mechanism appears localized in the case of a SSW and diffuses all over the domain for a current. The induced bedforms are very different: we observed asymmetric equal to each other dunes in one case and unstable ripples in the other. The bedforms triggering process for a steady current depends exclusively on the shear stress velocity induced at the bottom. A solitary wave that induces shear stress velocities larger than the critical value can also not induce any bedform. For a given free surface level, only for particular values of wavelength and amplitude, the necessary conditions for a strong enough reverse flow can occur, the more efficiently the more the hydrodynamic process assume an unsteady behavior. *Droghei et al.* [2016] argued that tidal induced ISWs can produce a unidirectional boundary current able to induce bedforms generation. It is possible for solitary waves to induce bedforms generation, and the triggering process depend on the unsteady nature of the induced boundary current.

Bibliography

Adduce, C., G. Sciortino, and S. Proietti, Gravity currents produced by lock exchanges: Experiments and simulations with a two-layer shallow-water model with entrainment, *J. Hydraul. Eng.-ASCE*, *138*(2), 111–121, 2012.

Aghsaee, P., and L. Boegman, Experimental investigation of sediment resuspension beneath internal solitary waves of depression, *Journal of Geophysical Research: Oceans*, *120*(5), 3301–3314, 2015.

Aghsaee, P., L. Boegman, and K. G. Lamb, Breaking of shoaling internal solitary waves, *Journal of Fluid Mechanics*, *659*, 289–317, 2010.

Aghsaee, P., L. Boegman, P. J. Diamessis, and K. G. Lamb, Boundary-layer-separation-driven vortex shedding beneath internal solitary waves of depression, *Journal of Fluid Mechanics*, *690*, 321–344, 2012.

Alpers, W., and E. Salusti, Scylla and charybdis observed from space, *Journal of Geophysical Research: Oceans*, *88*(C3), 1800–1808, 1983.

Alpers, W., P. Brandt, A. Rubino, and J. O. Backhaus, Recent contributions of remote sensing to the study of internal waves in the straits of gibraltar and messina, *Bulletin - Institut Oceanographique Monaco-Numero Special* -, pp. 21–40, 1996.

Alpers, W., P. Brandt, and A. Rubino, Internal waves generated in the straits of gibraltar and messina: Observations from space, *Barale, V. and Gade. M.(eds.), Remote Sensing of the European Seas. Dordrecht, the Netherlands: Springer*, pp. 319–330, 2008.

Armi, L., and D. M. Farmer, The flow of atlantic water through the strait of gibraltar. the flow of mediterranean water through the strait of gibraltar., *Progress in Oceanography*, *21*, 1988.

Artale, V., D. Levi, S. Marullo, and R. Santoleri, Analysis of nonlinear internal waves observed by landsat thematic mapper, *Journal of Geophysical Research: Oceans*, *95*(C9), 16,065–16,073, 1990.

Arthur, R. S., and O. B. Fringer, The dynamics of breaking internal solitary waves on slopes, *Journal of Fluid Mechanics*, *761*, 360–398, 2014.

Arthur, R. S., and O. B. Fringer, Transport by breaking internal gravity waves on slopes, *Journal of Fluid Mechanics*, *789*, 93–126, 2016.

Bakhoday-Paskyabi, M., Particle motions beneath irrotational water waves, *Ocean Dynamics*, *65*(8), 1063–1078, 2015.

Batchelor, G., H. Moffatt, M. Worster, and T. Osborn, Perspectives in fluid dynamics, 2000.

Boegman, L., and G. N. Ivey, Flow separation and resuspension beneath shoaling nonlinear internal waves, *Journal of Geophysical Research: Oceans*, *114*(C2), 2009.

Boegman, L., G. Ivey, and J. Imberger, The degeneration of internal waves in lakes with sloping topography, *Limnology and oceanography*, *50*(5), 1620–1637, 2005.

Bogucki, D., T. Dickey, and L. G. Redekopp, Sediment resuspension and mixing by resonantly generated internal solitary waves, *Journal of Physical Oceanography*, *27*(7), 1181–1196, 1997.

Bogucki, D. J., and L. G. Redekopp, A mechanism for sediment resuspension by internal solitary waves, *Geophysical Research Letters*, *26*(9), 1317–1320, 1999.

Bogucki, D. J., L. Redekopp, and J. Barth, Internal solitary waves in the coastal mixing and optics 1996 experiment: Multimodal structure and resuspension, *Journal of Geophysical Research: Oceans*, *110*(C2), 2005.

Borden, Z., T. Koblitz, and E. Meiburg, Turbulent mixing and wave radiation in non-boussinesq internal bores, *Physics of Fluids*, *24*(8), 082,106, 2012a.

Borden, Z., E. Meiburg, and G. Constantinescu, Internal bores: an improved model via a detailed analysis of the energy budget, *Journal of Fluid Mechanics*, *703*, 279–314, 2012b.

Bourgault, D., M. Blokhina, R. Mirshak, and D. Kelley, Evolution of a shoaling internal solitary wavetrain, *Geophysical Research Letters*, *34*(3), 2007.

Bourgault, D., M. Morsilli, C. Richards, U. Neumeier, and D. E. Kelley, Sediment resuspension and nepheloid layers induced by long internal solitary waves shoaling orthogonally on uniform slopes, *Continental Shelf Research*, *72*, 21–33, 2014.

Brandt, P., A. Rubino, D. Quadfasel, W. Alpers, J. Sellschopp, and H.-V. Fiekas, Evidence for the influence of atlantic–ionian stream fluctuations on the tidally induced internal dynamics in the strait of messina, *Journal of physical oceanography*, *29*(5), 1071–1080, 1999.

Bridges, T. J., Waves in oceanic and coastal waters, by leo h. holthuijsen, cambridge university press, 2007. isbn 978-0521860284., *Quarterly Journal of the Royal Meteorological Society*, *134*(636), 1947–1948, 2008.

Cacchione, D., L. F. Pratson, and A. Ogston, The shaping of continental slopes by internal tides, *Science*, *296*(5568), 724–727, 2002.

Carr, M., P. A. Davies, and P. Shivaram, Experimental evidence of internal solitary wave-induced global instability in shallow water benthic boundary layers, *Physics of Fluids*, *20*(6), 066,603, 2008.

Cenedese, C., and C. Adduce, Mixing in a density-driven current flowing down a slope in a rotating fluid., *J. Fluid Mech.*, *604*, 369–388, 2008.

Chen, C.-Y., J. R.-C. Hsu, C.-W. Chen, H.-H. Chen, C.-F. Kuo, and M.-H. Cheng, Generation of internal solitary wave by gravity collapse, *Journal of Marine Science and Technology*, *15*(1), 1–7, 2007.

Church, J. A., and N. J. White, A 20th century acceleration in global sea-level rise, *Geophysical research letters*, *33*(1), 2006.

Core Writing Team, R. P., and L. Meyer (Eds.), *IPCC 2014. Impacts, Adaptation and Vulnerability: Part A: Global and Sectoral Aspects: Working Group II Contribution to the IPCC Fifth Assessment Report*, Cambridge University Press, doi:10.1017/CBO9781107415379, 2014a.

Core Writing Team, R. P., and L. Meyer (Eds.), *IPCC 2014.Climate Change 2014: Synthesis Report. Contribution of Working Groups I, II and III to the Fifth Assessment Report of the Intergovernmental Panel on Climate Change*, Cambridge University Press, doi:10.1017/CBO9781107415416, 2014b.

Dalziel, S. B., M. D. Patterson, C. Caulfield, and I. A. Coomaraswamy, Mixing efficiency in high-aspect-ratio rayleigh–taylor experiments, *Physics of Fluids*, *20*(6), 065,106, 2008.

Davis, K. A., and S. G. Monismith, The modification of bottom boundary layer turbulence and mixing by internal waves shoaling on a barrier reef, *Journal of Physical Oceanography*, *41*(11), 2223–2241, 2011.

Dean, R. G., and R. A. Dalrymple, *Water wave mechanics for engineers and scientists*, vol. 2, world scientific publishing Co Inc, 1991.

DeCarlo, T. M., K. B. Karnauskas, K. A. Davis, and G. T. Wong, Climate modulates internal wave activity in the northern south china sea, *Geophysical Research Letters*, *42*(3), 831–838, 2015.

Defant, A. J. M., *Scylla und Charybdis und die Gezeitenströmungen in der Straße von Messina*, 1940.

Diamessis, P. J., and L. G. Redekopp, Numerical investigation of solitary internal wave-induced global instability in shallow water benthic boundary layers, *Journal of physical oceanography*, *36*(5), 784–812, 2006.

D'Ortenzio, F., D. Iudicone, C. de Boyer Montegut, P. Testor, D. Antoine, S. Marullo, R. Santoleri, and G. Madec, Seasonal variability of the mixed layer depth in the mediterranean sea as derived from in situ profiles, *Geophysical Research Letters*, *32*(12), 2005.

Droghei, R., F. Falcini, D. Casalbore, E. Martorelli, R. Mosetti, G. Sannino, R. Santoleri, and F. Chiocci, The role of internal solitary waves on deep-water sedimentary processes: the case of up-slope migrating sediment waves off the messina strait, *Scientific reports*, *6*, 36,376, 2016.

Förste, J., Schlichting, h., boundary-layer theory. transl. by j. kestin. mcgraw-hill series in mechanical engineering. new york-st. louis-san francisco-auckland-bogotà-düsseldorf-johannesburg-london-madrid-mexico-montreal-new delhi-panama-paris-são paulo-singapore-sydney-tokyo-toronto, mcgraw-hill book company 1979. xxii, 817 s., 429 abb., 3 tab.,£ 9.23. isbn 0-07-055334-3., *ZAMM-Journal of Applied Mathematics and Mechanics/Zeitschrift für Angewandte Mathematik und Mechanik*, *60*(4), 217–217, 1980.

Fragoso, A., M. Patterson, and J. J.S. Wettlaufer, Mixing in gravity currents, *J. Fluid Mech.*, *734*, Art–No, 2013.

Garrett, C., Internal tides and ocean mixing, *Science*, *301*(5641), 1858–1859, 2003.

Garrett, C., and E. Kunze, Internal tide generation in the deep ocean, *Annu. Rev. Fluid Mech.*, *39*, 57–87, 2007.

Gayen, B., and S. Sarkar, Turbulence during the generation of internal tide on a critical slope, *Physical review letters*, *104*(21), 218,502, 2010.

Gayen, B., and S. Sarkar, Boundary mixing by density overturns in an internal tidal beam, *Geophysical Research Letters*, *38*(14), 2011.

Grue, J., A. Jensen, P.-O. Rusås, and J. K. Sveen, Properties of large-amplitude internal waves, *Journal of Fluid Mechanics*, *380*, 257–278, 1999.

Grue, J., A. Jensen, P.-O. Rusås, and J. K. Sveen, Breaking and broadening of internal solitary waves, *Journal of Fluid Mechanics*, *413*, 181–217, 2000.

Helfrich, K. R., Internal solitary wave breaking and run-up on a uniform slope, *Journal of Fluid Mechanics*, *243*, 133–154, 1992.

Helfrich, K. R., and W. Melville, On long nonlinear internal waves over slope-shelf topography, *Journal of Fluid Mechanics*, *167*, 285–308, 1986.

Hsu, H.-C., Y.-Y. Chen, and H.-H. Hwung, Experimental study of the particle paths in solitary water waves, *Phil. Trans. R. Soc. A*, *370*(1964), 1629–1637, 2012.

Ivey, G., and J. Imberger, On the nature of turbulence in a stratified fluid. part i: The energetics of mixing, *Journal of Physical Oceanography*, *21*(5), 650–658, 1991.

Kao, T. W., F.-S. Pan, and D. Renouard, Internal solitons on the pycnocline: generation, propagation, and shoaling and breaking over a slope, *Journal of Fluid Mechanics*, *159*, 19–53, 1985.

Klymak, J. M., and J. N. Moum, Internal solitary waves of elevation advancing on a shoaling shelf, *Geophysical Research Letters*, *30*(20), 2003.

Korteweg, D. J., and G. De Vries, Xli. on the change of form of long waves advancing in a rectangular canal, and on a new type of long stationary waves, *The London, Edinburgh, and Dublin Philosophical Magazine and Journal of Science*, *39*(240), 422–443, 1985.

Kraucunas, I., *Surface temperature reconstructions for the last 2,000 years*, 1–155 pp., National Academies Press, 2006.

La Forgia, G., C. Adduce, and F. Falcini, Laboratory investigation on internal solitary waves interacting with a uniform slope, *Advances in Water Resources*, *ISSN 0309-1708*, 2017.

Lai, Z., C. Chen, R. C. Beardsley, B. Rothschild, and R. Tian, Impact of high-frequency nonlinear internal waves on plankton dynamics in massachusetts bay, *Journal of Marine Research*, *68*(2), 259–281, 2010.

Lamb, K. G., Particle transport by nonbreaking, solitary internal waves, *Journal of Geophysical Research: Oceans*, *102*(C8), 18,641–18,660, 1997.

Lamb, K. G., A numerical investigation of solitary internal waves with trapped cores formed via shoaling, *Journal of Fluid Mechanics*, *451*, 109–144, 2002.

Levitus, S., J. I. Antonov, T. P. Boyer, R. A. Locarnini, H. E. Garcia, and A. V. Mishonov, Global ocean heat content 1955–2008 in light of recently revealed instrumentation problems, *Geophysical Research Letters*, *36*(7), 2009.

Li, Y., and F. Raichlen, Non-breaking and breaking solitary wave run-up, *Journal of Fluid Mechanics*, *456*, 295–318, 2002.

Lombardi, V., C. Adduce, G. Sciortino, and M. L. Rocca, Gravity currents flowing upslope:laboratory experiments and shallow water simulations, *Phys. Fluids*, *27*(1), 016,602, 2015.

Lorenz, E. N., Available potential energy and the maintenance of the general circulation, *Tellus*, *7*(2), 157–167, 1955.

Marin, F., N. Abcha, J. Brossard, and A. B. Ezersky, Laboratory study of sand bed forms induced by solitary waves in shallow water, *Journal of Geophysical Research: Earth Surface*, *110*(F4), 2005.

Martine, C., and C. Jean-Pierre, Le detroit de messine (italie). evolution tectono-sédimentaire récente (pliocène et quaternaire) et environnement actuel. documents et travaux de l'institut géologique albert de lappar-ent., *Bulletin de l'Association française pour l'étude du quaternaire*, *25*(4), 216–217, 1988.

Marullo, S., and R. Santoleri, Fronts and internal currents at the northern mouth of the strait of messina, *Il Nuovo Cimento C*, *9*(3), 701–713, 1986.

Maxworthy, T., A note on the internal solitary waves produced by tidal flow over a three-dimensional ridge, *Journal of Geophysical Research: Oceans*, *84*(C1), 338–346, 1979.

McPhee-Shaw, E., Boundary–interior exchange: reviewing the idea that internal-wave mixing enhances lateral dispersal near continental margins, *Deep Sea Research Part II: Topical Studies in Oceanography*, *53*(1), 42–59, 2006.

Meyer-Peter, E., and R. Muller, Formulas for bed-load transport. international association for hydraulic structure, in *Second meeting, Stockholm*, 1948.

Michallet, H., and G. Ivey, Experiments on mixing due to internal solitary waves breaking on uniform slopes, *Journal of Geophysical Research: Oceans*, *104*(C6), 13,467–13,477, 1999.

Munk, W. H., and M. A. Traylor, Refraction of ocean waves: a process linking underwater topography to beach erosion, *The Journal of Geology*, *55*(1), 1–26, 1947.

Musumeci, R. E., A. Viviano, and E. Foti, Influence of regular surface waves on the propagation of gravity currents: Experimental and numerical modeling, *Journal of Hydraulic Engineering*, *143*(8), 04017,022, 2017.

Nakayama, K., and J. Imberger, Residual circulation due to internal waves shoaling on a slope, *Limnology and Oceanography*, *55*(3), 1009–1023, 2010.

Nakayama, K., T. Shintani, K. Kokubo, T. Kakinuma, Y. Maruya, K. Komai, and T. Okada, Residual currents over a uniform slope due to breaking of internal waves in a two-layer system, *Journal of Geophysical Research: Oceans*, *117*(C10), 2012.

Nash, J. D., and J. N. Moum, River plumes as a source of large-amplitude internal waves in the coastal ocean, *Nature*, *437*(7057), 400, 2005.

Nash, J. D., E. Kunze, J. M. Toole, and R. W. Schmitt, Internal tide reflection and turbulent mixing on the continental slope, *Journal of Physical Oceanography*, *34*(5), 1117–1134, 2004.

Necker, F., C. Härtel, L. Kleiser, and E. Meiburg, Mixing and dissipation in particle-driven gravity currents, *Journal of Fluid Mechanics*, *545*, 339–372, 2005.

Nicolò, L., and E. Salusti, Field and satellite observations of large amplitude internal tidal wave trains south of the strait of messina, mediterranean sea, in *Annales geophysicae*, vol. 9, pp. 534–539, Copernicus, 1991.

Niwa, Y., and T. Hibiya, Numerical study of the spatial distribution of the m2 internal tide in the pacific ocean, *Journal of Geophysical Research: Oceans*, *106*(C10), 22,441–22,449, 2001.

Nogueira, H., C. Adduce, E. Alves, and M. Franca, Analysis of lock-exchange gravity currents over smooth and rough beds, *J. Hydraul. Res.*, *51*(4), 417–431, 2013a.

Nogueira, H., C. Adduce, E. Alves, and M. Franca, Image analysis technique applied to lock-exchange gravity currents, *Meas. Sci. Technol.*, *24*(4), 047,001, 2013b.

Nogueira, H., C. Adduce, E. Alves, and M. Franca, Dynamics of the head of gravity currents, *Environ. Fluid Mech.*, *14*, 519–540, 2014.

Olsthoorn, J., and M. Stastna, Numerical investigation of internal wave-induced sediment motion: Resuspension versus entrainment, *Geophysical Research Letters*, *41*(8), 2876–2882, 2014.

Ooi, S. K., G. Constantinescu, and L. Weber, A numerical study of intrusive compositional gravity currents, *Physics of Fluids*, *19*(7), 076,602, 2007.

Osborne, A., and T. Burch, Internal solitons in the andaman sea, *Science*, *208*(4443), 451–460, 1980.

Osborne, A., T. Burch, R. Scarlet, et al., The influence of internal waves on deep-water drilling, *Journal of Petroleum Technology*, *30*(10), 1–497, 1978.

Ottolenghi, L., C. Adduce, R. Inghilesi, F. Roman, and V. Armenio, Large eddy simulation of gravity currents moving on up-sloping boundaries, in *River Flow 2014: International conference on Fluvial Hydraulics, Lausanne, Switzerland, 3-5 September 2014*, pp. 189–196, 2014.

Ottolenghi, L., C. Adduce, R. Inghilesi, V. Armenio, and F. Roman, Entrainment and mixing in unsteady gravity currents, *J. Hydraul. Res.*, *54*(5), 541–557, 2016a.

Ottolenghi, L., C. Adduce, R. Inghilesi, F. Roman, and V. Armenio, Mixing in lock-release gravity currents propagating up a slope, *Phys. Fluids*, *28*(5), 056,604, 2016b.

Ottolenghi, L., C. Adduce, F. Roman, and V. Armenio, Analysis of the flow in gravity currents propagating up a slope, *Ocean Modelling*, *115*, 1–13, 2017a.

Ottolenghi, L., C. Cenedese, and C. Adduce, Entrainment in a dense current flowing down a rough sloping bottom in a rotating fluid, *Journal of Physical Oceanography*, *47*(3), 485–498, 2017b.

Ottolenghi, L., P. Prestininzi, A. Montessori, C. Adduce, and M. La Rocca, Lattice boltzmann simulations of gravity currents, *European Journal of Mechanics-B/Fluids*, 2017c.

Ozeren, Y., and M. Altinakar, Turbidity currents generated by bank failure under wave erosion, in *River Flow 2016. ISBN 978-1-138-02913-2*, pp. 882–889, 2016.

Patterson, M., C. Caulfield, J. McElwaine, and S. Dalziel, Time-dependent mixing in stratified kelvin-helmholtz billows: Experimental observations, *Geophys. Res. Lett.*, *33*(15), 2006.

Pedlowsky, J., and J. Miles, Waves in the ocean and atmosphere: Introduction to wave dynamics, *Applied Mechanics Reviews*, *57*, B20, 2004.

Peltier, W., and C. Caulfield, Mixing efficiency in stratified shear flows, *Annual review of fluid mechanics*, *35*(1), 135–167, 2003.

Peterson, T., and M. Baringer, State of the climate in 2008, *Bull. Am. Meteorol. Soc.*, *90*, S1–S196, 2009.

Pierce, C. D., and P. Moin, *Progress-variable approach for large-eddy simulation of turbulent combustion*, stanford university California, USA, 2001.

Prastowo, T., R. Griffiths, G. Hughes, and A. M. Hogg, Effects of topography on the cumulative mixing efficiency in exchange flows, *Journal of Geophysical Research: Oceans*, *114*(C8), 2009.

Puig, P., A. Palanques, J. Guillén, and M. El Khatab, Role of internal waves in the generation of nepheloid layers on the northwestern alboran slope: implications for continental margin shaping, *Journal of Geophysical Research: Oceans*, *109*(C9), 2004.

Quaresma, L. S., J. Vitorino, A. Oliveira, and J. da Silva, Evidence of sediment resuspension by nonlinear internal waves on the western portuguese mid-shelf, *Marine geology*, *246*(2), 123–143, 2007.

Robinson, T., I. Eames, and R. Simons, Dense gravity currents moving beneath progressive free-surface water waves, *Journal of Fluid Mechanics*, *725*, 588–610, 2013.

Russell, J. S., Report on waves, in *14th meeting of the British Association for the Advancement of Science*, vol. 311, p. 1844, 1844.

Santoro, V. C., E. Amore, L. Cavallaro, G. Cozzo, and E. Foti, Sand waves in the messina strait, italy, *J. Coastal Res*, *36*, 640–653, 2002.

Sapia, A., and E. Salusti, Observation of nonlinear internal solitary wave trains at the northern and southern mouths of the strait of messina, *Deep Sea Research Part A. Oceanographic Research Papers*, *34*(7), 1081–1092, 1987.

Scotti, A., and J. Pineda, Observation of very large and steep internal waves of elevation near the massachusetts coast, *Geophysical Research Letters*, *31*(22), 2004.

Selli, R., P. Colantoni, A. Fabbri, S. Rossi, A. Borsetti, and P. Gallignani, Marine geological investigation on the messina strait and its approaches, *Giornale di Geologia*, *42*(2), 1–70, 1978.

Simmons, H. L., and M. H. Alford, Simulating the long-range swell of internal waves generated by ocean storms, *Oceanography*, *25*(2), 30–41, 2012.

Skåre, P. E., and P.-å. Krogstad, A turbulent equilibrium boundary layer near separation, *Journal of Fluid Mechanics*, *272*, 319–348, 1994.

Soulsby, R., R. Atkins, and A. Salkield, Observations of the turbulent structure of a suspension of sand in a tidal current, *Continental Shelf Research*, *14*(4), 429–435, 1994.

Stashchuk, N., and V. Vlasenko, Generation of internal waves by a supercritical stratified plume, *Journal of Geophysical Research: Oceans*, *114*(C1), 2009.

Stastna, M., and K. G. Lamb, Vortex shedding and sediment resuspension associated with the interaction of an internal solitary wave and the bottom boundary layer, *Geophysical research letters*, *29*(11), 2002.

Stastna, M., and K. G. Lamb, Sediment resuspension mechanisms associated with internal waves in coastal waters, *Journal of Geophysical Research: Oceans*, *113*(C10), 2008.

Steenhauer, K., T. Tokyay, and G. Constantinescu, Dynamics and structure of planar gravity currents propagating down an inclined surface, *Physics of Fluids*, *29*(3), 036,604, 2017.

Stocker, T., et al. (Eds.), *IPCC 2013. Climate Change 2013: The Physical Science Basis. Contribution of Working Group I to the Fifth Assessment Report of the Intergovernmental Panel on Climate Change*, Cambridge University Press, Cambridge, United Kingdom and New York, NY, USA, doi:10.1017/CBO9781107415324, 2013.

Sutherland, B., and K. Ivey, Shoaling internal solitary waves, *J. Geophys. Res. Ocean*, *118*, 4111–4124, 2013.

Synolakis, C. E., The runup of solitary waves, *Journal of Fluid Mechanics*, *185*, 523–545, 1987.

Theiler, Q., and M. J. Franca, Contained density currents with high volume of release, *Sedimentology*, *63*(6), 1820–1842, 2016.

Tokyay, T., and G. Constantinescu, The effects of a submerged non-erodible triangular obstacle on bottom propagating gravity currents, *Physics of Fluids*, *27*(5), 056,601, 2015.

Tokyay, T., G. Constantinescu, and E. Meiburg, Lock-exchange gravity currents with a high volume of release propagating over a periodic array of obstacles, *J. Fluid Mech.*, *672*, 570–605, 2011.

Tokyay, T., G. Constantinescu, and E. Meiburg, Tail structure and bed friction velocity distribution of gravity currents propagating over an array of obstacles, *J. Fluid Mech.*, *694*, 252–291, 2012.

Tokyay, T., G. Constantinescu, and E. Meiburg, Lock-exchange gravity currents with a low volume of release propagating over an array of obstacles, *Journal of Geophysical Research: Oceans*, *119*(5), 2752–2768, 2014.

Van Rijn, L. C., Sediment pick-up functions, *Journal of Hydraulic engineering*, *110*(10), 1494–1502, 1984.

Venayagamoorthy, S., and O. Fringer, Numerical simulations of the interaction of internal waves with a shelf break, *Physics of Fluids*, *18*(7), 076,603, 2006.

Venayagamoorthy, S. K., and O. B. Fringer, On the formation and propagation of nonlinear internal boluses across a shelf break, *Journal of Fluid Mechanics*, *577*, 137–159, 2007.

Vercelli, E., *Il regime delle correnti e delle maree nello Stretto di Messina*, Venezia, 1925.

Vlasenko, V., and K. Hutter, Numerical experiments on the breaking of solitary internal wavesover a slope–shelf topography, *Journal of Physical Oceanography*, *32*(6), 1779–1793, 2002.

Vlasenko, V., and N. Stashchuk, Three-dimensional shoaling of large-amplitude internal waves, *Journal of Geophysical Research: Oceans*, *112*(C11), 2007.

Walter, R. K., C. B. Woodson, R. S. Arthur, O. B. Fringer, and S. G. Monismith, Nearshore internal bores and turbulent mixing in southern monterey bay, *Journal of Geophysical Research: Oceans*, *117*(C7), 2012.

Wilkox, D., *Basic Fluid Mechanics, Third Edition.*, DCW Industries, 2010.

Winters, K., and E. D'Asaro, Diascalar flux and the rate of fluid mixing, *J. Fluid Mech.*, *317*, 179–193, 1996.

Winters, K., P. Lombard, J. Riley, and E. D'Asaro, Available potential energy and mixing in density-stratified fluids, *J. Fluid Mech.*, *289*, 115–128, 1995.

Zhou, J.-x., X.-z. Zhang, and P. H. Rogers, Resonant interaction of sound wave with internal solitons in the coastal zone, *The Journal of the Acoustical Society of America*, *90*(4), 2042–2054, 1991.

Acknowledgements

This work presents the research activity carried out, as PhD student of the XXX doctoral cycle at the University of Roma Tre (Rome, Italy). Prof. Claudia Adduce (University of Roma Tre) and Dr. Federico Falcini (Institute of Atmospheric Sciences and Climate, Rome Italy) supervised my research activity. It was funded by 'Ritmare Flagship Project', one of the 'National Research Programmes' for the period 2012-2016, supported by the Italian Ministry of University and Research, and coordinated by the National Research Council (CNR).

I want to thank all the institutions and the people who collaborated with me in this study:

- **Roma Tre University (Rome, Italy).**
  I would firstly like to thank my Ph.D. Advisor, Prof. Claudia Adduce for her leading role and her constant support during these years.
- **ISAC-CNR (Institute of Atmospheric Sciences and Climate, Rome, Italy).**
  A special thank to my Co-Advisor Dr. Federico Falcini, for his expertise and useful suggestions, fundamental for the development of the present study.
- **SAFL (Saint Anthony Falls Laboratory, Minneapolis, MN, USA).**
  I would like to really thank Prof. Chris Paola, for giving me the opportunity to work with him and his brilliant staff at SAFL, for six months. It was a wonderful experience that made me even better conscious of how exciting and challenging the research world is .

I want to thank Prof. George Constantinescu (The University of Iowa, IA, USA) and Dr. Talia Ekin Tokyay Sinha (Middle East Technical University, Ankara, Turkey) for the collaborative research we developed.

A special mention goes for Dr. Luisa Ottolenghi (University of Roma Tre) for the constant support and presence. Finally, my warm thanks to all the people of the research group of the Engineering Department with whom I daily shared this experience.